DAMPING ESTIMATION, RESPONSE PREDICTION AND FATIGUE CALCULATION OF AN OPERATIONAL SINGLE PILE PLATFORM

by

MICHAEL FERRIS COOK

B.S. Texas A&M University
(1978)

SUBMITTED IN PARTIAL FULFILLMENT OF THE
REQUIREMENTS FOR THE DEGREE OF
OCEAN ENGINEER

at the

MASSACHUSETTS INSTITUTE OF TECHNOLOGY

and the

WOODS HOLE OCEANOGRAPHIC INSTITUTION

AND FOR THE DEGREE OF

MASTER OF SCIENCE

in OCEAN ENGINEERING

at the

MASSACHUSETTS INSTITUTE OF TECHNOLOGY

January, 1982

Signature of Author . . . . . Joint Program in Ocean Engineering, Massachusetts Institute of Technology/Woods Hole Oceanographic Institution, and Department of Ocean Engineering, Massachusetts Institute of Technology, January, 1982.

Certified by . . . . . J.K. Vandiver, Thesis Supervisor, MIT

Certified by . . . . . H.O. Berteaux, Thesis Supervisor, WHOI

Accepted by . . . . . Earl E. Hayes, Chairman, Joint Committee on Ocean Engineering, Massachusetts Institute of Technology/Woods Hole Oceanographic Institution

DAMPING ESTIMATION, RESPONSE PREDICTION AND FATIGUE CALCULATION OF AN OPERATIONAL SINGLE PILE PLATFORM

by

MICHAEL FERRIS COOK

Submitted to the Department of Ocean Engineering in January, 1982 in partial fulfillment of the requirements for the Degree of Ocean Engineer at the Massachusetts Institute of Technology and the Woods Hole Oceanographic Institution and for the degree of Master of Science in Ocean Engineering at the Massachusetts Institute of Technology

ABSTRACT

A comparison between predicted and measured damping controlled dynamic response of an operational single pile platform (AMOCO's South Marsh Island Block 33B platform) is presented. In the predictive analysis, a finite element model of the structure and a theoretical assessment of damping phenomena are combined with a response prediction method which utilizes the principle of reciprocity of ocean waves. The result is a versatile expression for the estimation of the dynamic response fatigue life of a platform in a directionally spread sea. In addition, the data analysis performed on wind, wave and response time histories, recorded in March, 1980, is carefully described. A method is presented which uses biaxial accelerometer data to infer platform modal orientations and to estimate wave spreading. Finally, modal natural frequencies and damping ratios are estimated using the Maximum Entropy Method (MEM) of spectral analysis. Good agreement between predicted and estimated response characteristics is attained.

Thesis Supervisor: Dr. J. Kim Vandiver
Title: Associate Professor of Ocean Engineering
Massachusetts Institute of Technology

Thesis Supervisor: Mr. Henri O. Berteaux
Title: Research Specialist
Woods Hole Oceanographic Institution

ACKNOWLEDGEMENTS

This research was sponsored by the Branch of Marine Oil and Gas Operations of the United States Geological Survey, Department of the Interior, and the Joint Program in Oceanographic Engineering between the Massachusetts Institute of Technology and Woods Hole Oceanographic Institution. In addition, thanks must be given to AMOCO Oil Company for permitting us to collect and analyze wind, wave and response data from their South Marsh Island Block 33 single pile platform.

As a Joint Program student, I am particularly grateful to Henri O. Berteaux for his guidance and encouragement during my two summers at Woods Hole and thereafter.

I will always be indebted to J. Kim Vandiver. His enthusiasm, drive, guidance, and friendship have made my career as a graduate student very fulfilling.

Special thanks is due Mike Briggs for his analysis of portions of the AMOCO caisson data and the inclusion of some of his results here. In addition, the help of C.Y. Liou during the last few weeks has been appreciated. I am also grateful to Anna Markowitz for typing this thesis.

I want to thank my parents for everything they have done to aid my development into adulthood.

Finally, it is impossible to adequately convey my true feelings to my financée, Rosanne. Her unending support, encouragement, friendship and love has made my life infinitely richer. To her I am truly indebted.

TABLE OF CONTENTS

LIST OF FIGURES

LIST OF TABLES

CHAPTER 1

INTRODUCTION

Within the last five years, a record number of offshore platforms have been installed which have fundamental flexural natural frequencies within the band of excitation provided by ocean waves. For these structures, modal periods are longer than 2.5 seconds and resonant dynamic response is possible even in moderate sea states. The level of response associated with resonant excitation of a structural mode depends on the modal damping present within the vibrating system. For offshore platforms, the modal damping ratio is small (less than 5%) and significant damping controlled dynamic responses are expected. The governing design criteria for these flexible structures is often the prevention of failure due to low stress/high cycle fatigue. In this thesis, the variables which contribute in a fatigue analysis of an operational single pile platform are addressed.

The structure which is the focus of this research is a single well gas production platform, operated by AMOCO Oil Company, located in South Marsh Island (SMI) Block 33 in the Gulf of Mexico. Although the caisson stands in only 89 feet of water, the fundamental flexural modal periods exceed three seconds and significant dynamic response occurs, even in moderate sea states. The motivation for focusing attention on a single pile platform is that it is a relatively simple structure exhibiting all the response characteristics of

larger structures. With its inherent symmetry and the absence of adjacent members to obscure wave loading effects, it is an ideal structure to validate response prediction models.

In Chapter 2, a description of the AMOCO single pile platform is presented.

In Chapter 3, the formulation and performance of a dynamic finite element model of the structure is discussed. The structure is idealized as an assemblage of two-dimensional beam elements. Soil properties are incorporated in the model using linear soil springs. Uncertainties associated with the resulting idealization are addressed and the performance of the model is compared with field response data.

The subject of damping estimation is the topic of Chapter 4. In this chapter, the four dominant sources of damping applicable to offshore structures, namely steel hysteretic damping, radiation (wave making) damping, viscous hydrodynamic damping and soils damping, are described. In addition, theoretical techniques to estimate each source of modal damping are presented and compared with total damping estimates obtained from field data.

In Chapter 5, the mean square damping controlled dynamic response of the AMOCO caisson, when subjected to a directionally spread random sea, is estimated using the reciprocity method [Vandiver, 1979]. This method utilizes the principle of reciprocity for ocean waves. Wave spreading is included in this technique and four different spreading functions are described. The chapter concludes with a discussion of vor-

tex shedding.

In Chapter 6, the dynamic response fatigue life of the AMOCO caisson is estimated using a fatigue accumulation model which assumes the stress history is a narrow band Gaussian random process [Crandall and Mark, 1963]. A versatile expression for the mean rate of fatigue accumulation is produced when this model is combined with the reciprocity method of response prediction.

Chapter 7 contains a description of field tests performed on the AMOCO caisson in March, 1980, by Professor Vandiver and the author. Wind, wave and acceleration response time histories were obtained.

In Chapter 8, the analysis of this data is presented. Both single-channel and two-channel spectral analysis techniques were used to quantify the behavior of the platform under random wave loading. The use of biaxial accelerometer data to isolate the modal directions and estimate the spreading in the seas is shown. Natural frequencies and modal damping ratios are estimated for the fundamental flexural modes using MEM spectral analysis.

In the last chapter, conclusions and recommendations for future research are presented.

CHAPTER 2

PLATFORM DESCRIPTION

The single pile platform (caisson) investigated throughout this thesis is a single-well gas production platform operated by AMOCO Oil Company. The caisson stands in 89 feet of water in South Marsh Island Block 33 in the Gulf of Mexico. The pile rises 40 feet above the water and is driven to a depth of 100 feet below the mudline. On top of the pile are three decks. The lowest (wellhead) deck is 20 feet on a side and supports the top of the well (commonly referred to as the Christmas (Xmas) tree). The middle (production) deck is 57 feet above sea level and is also 20 feet square. A small crane, a pig trap and a large heater vessel are the major equipment on this deck. The top deck, 76 feet above the water, is 24 feet on a side and is used as a heliport. All of the structural components of the platform are fabricated from steel. A three-dimensional drawing and an elevation view of the caisson are shown in Figures 2.1 and 2.2.

One of the most interesting aspects of a single pile platform is the caisson. It consists of the outer pile which is 4 feet in diameter from its upper cutoff point to a level 20 feet below sea level, where the diameter increases linearly to 7 feet at a point 50 feet below sea level. The outer pile remains 7 feet in diameter to its terminal depth 100 feet below the mudline. The outer wall thickness is one inch, except for a 60 foot long, 1.375 inch thick, section

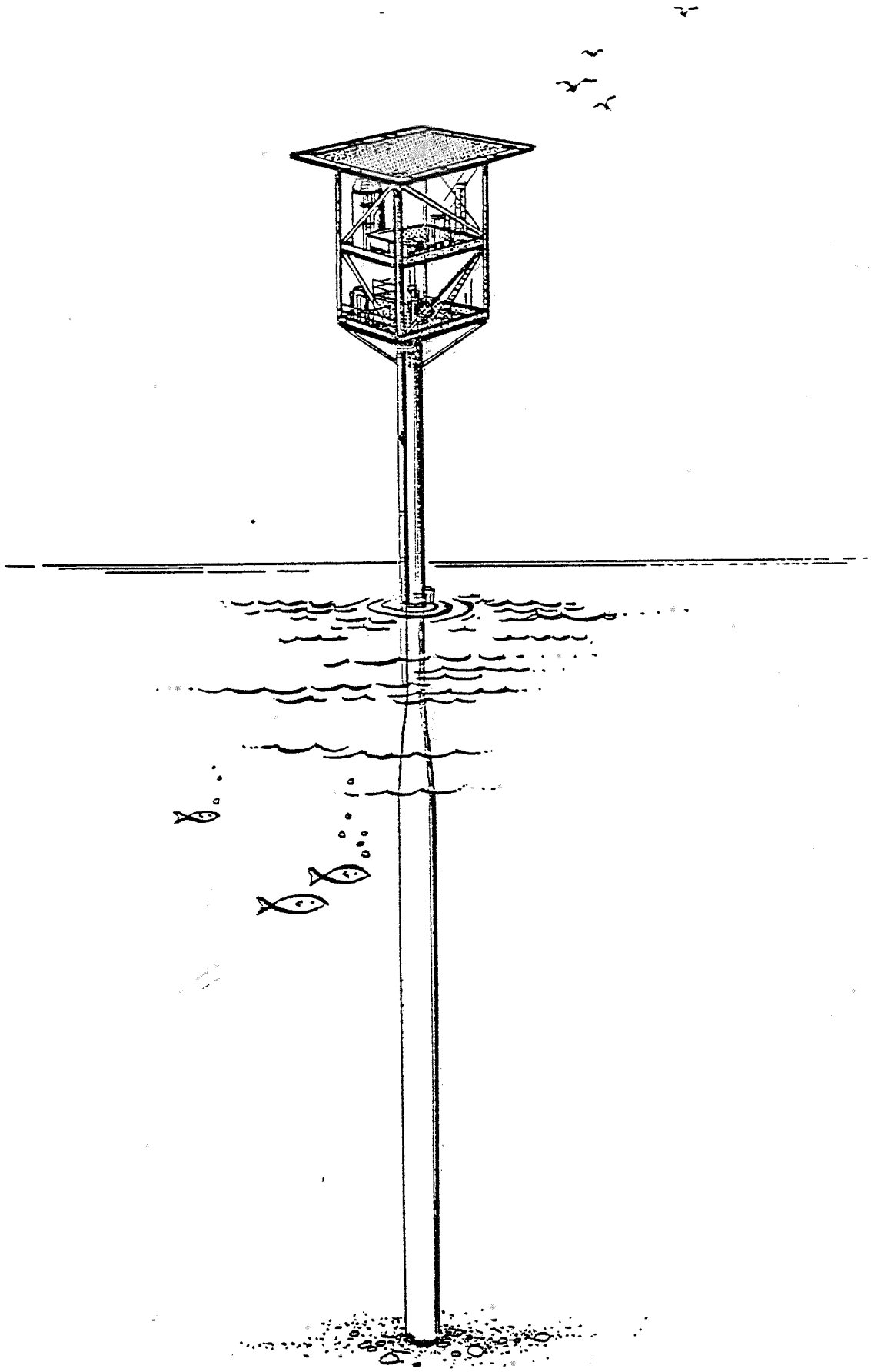

FIG. 2.1: THREE-DIMENSIONAL DRAWING OF THE AMOCO CAISSON

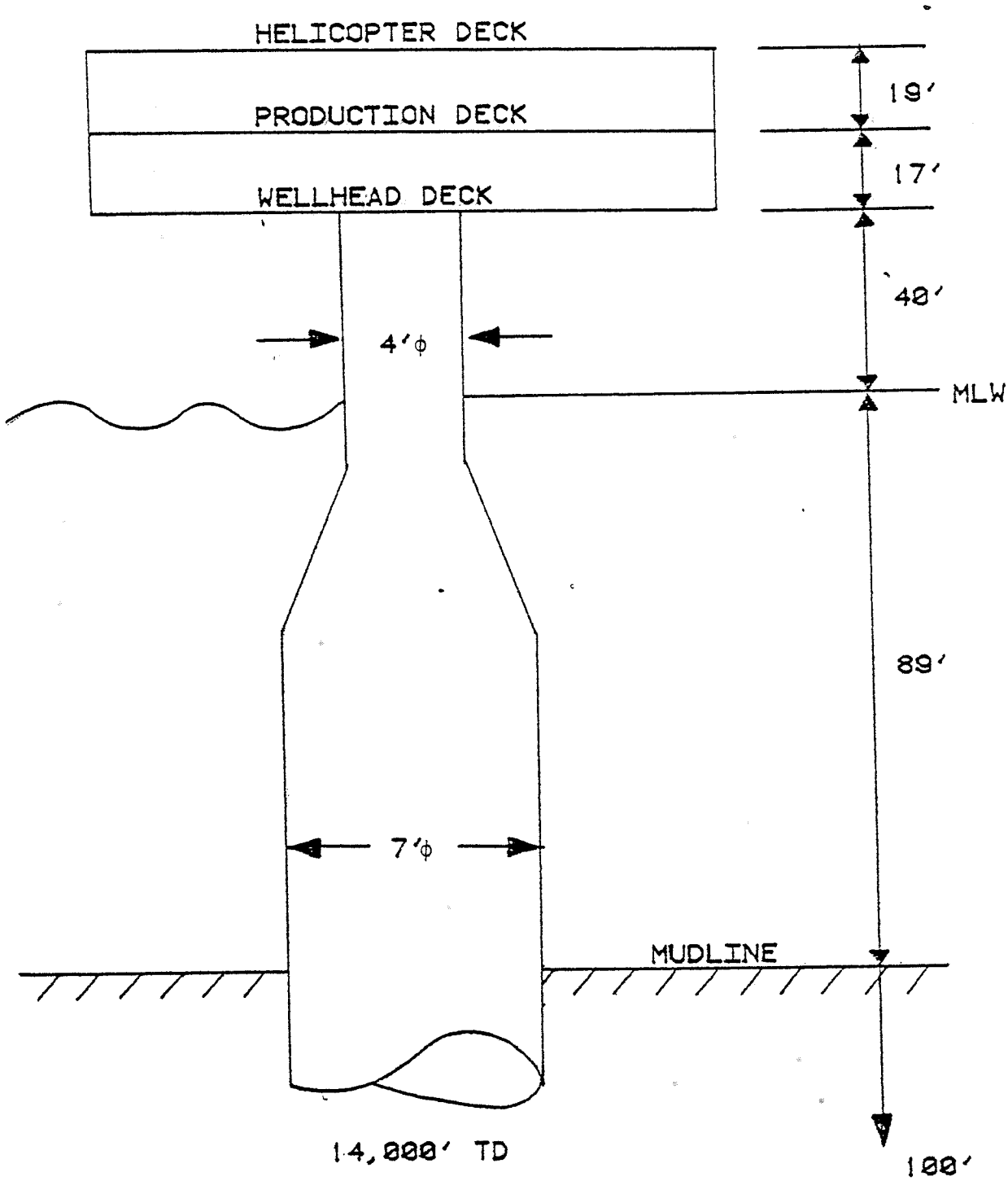

FIG 2.2: ELEVATION VIEW OF AMOCO CAISSON

which starts 10 feet above the mudline. The outer pile was installed in conventional offshore fashion in 20 to 30 foot long sections which were welded together during the pile-driving operation. Inside the outer pile are six smaller diameter concentric pipes which are associated with the well. The diameters of these pipes range from 30 inches to 2 7/8 inches. The 30 inch pipe, commonly referred to as the drive pile, was pile-driven to a depth 221 feet below the mudline. Together with the outer pile, these two members support all the other internal pipes, which are in tension, and the deck superstructure. The space between the pile and the 30 inch drive pipe is filled with 4000 psi compressive strength grout down to the mudline. The grout is used to increase both the weight and the stiffness of the caisson.

Predicting the response of a multi-legged structure is usually complicated by the lack of symmetry and the difficulty in quantifying the interaction effects of adjacent members. A single pile platform, however, minimizes these difficulties. The AMOCO caisson (Lollipop) is reasonably axisymmetric with the only major asymmetry a result of the placement of equipment on the decks. The absence of interaction effects is not strictly satisfied either. At the free surface, a boat landing is attached to the pile. The landing is constructed of both horizontal and vertical tubular members which have significant surface area in the wave impact zone (Figures 2.3 and 2.4). The presence of the landing increases the wave loading. Also, along the entire length of

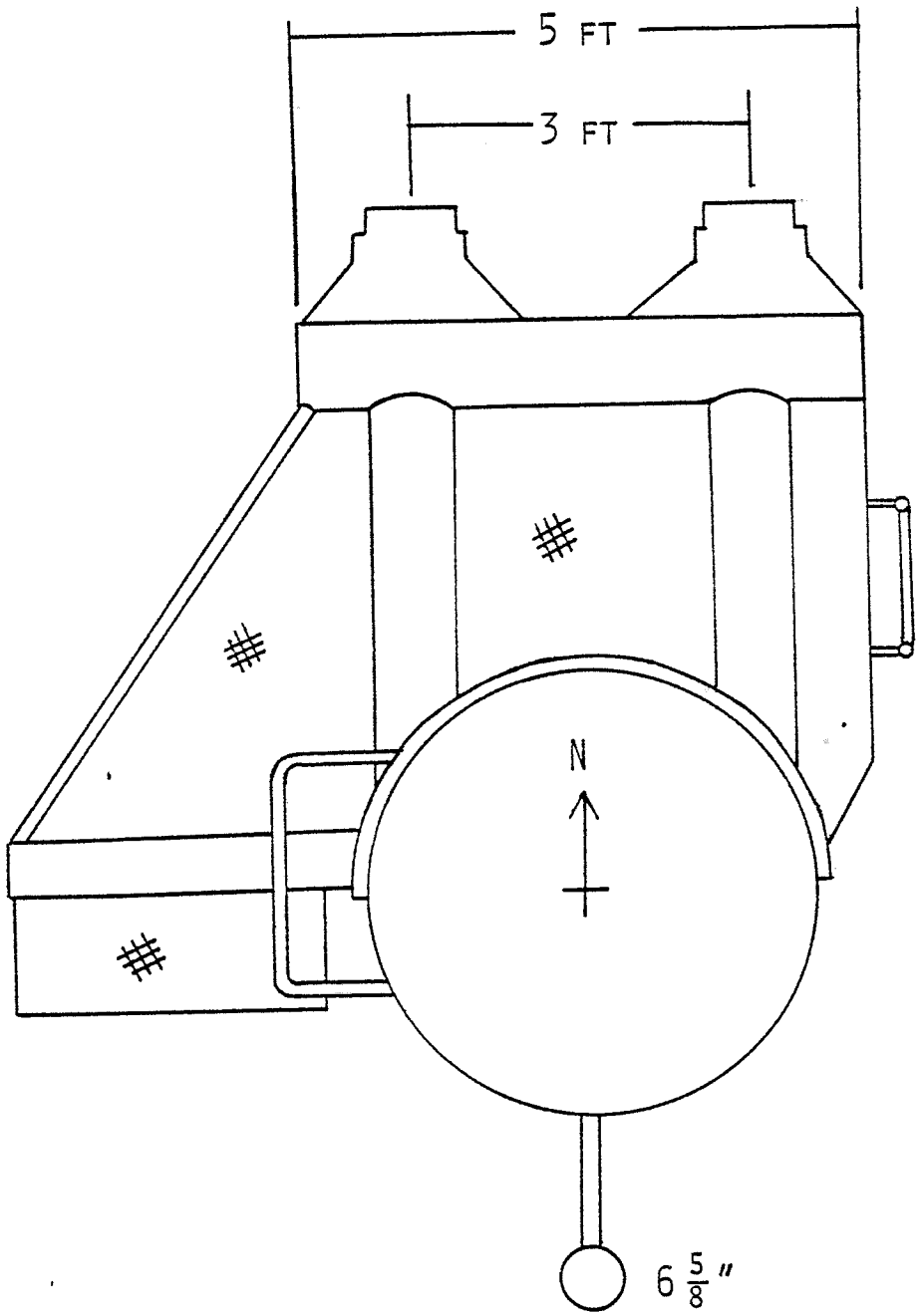

FIG. 2.3: PLAN VIEW OF THE BOAT LANDING

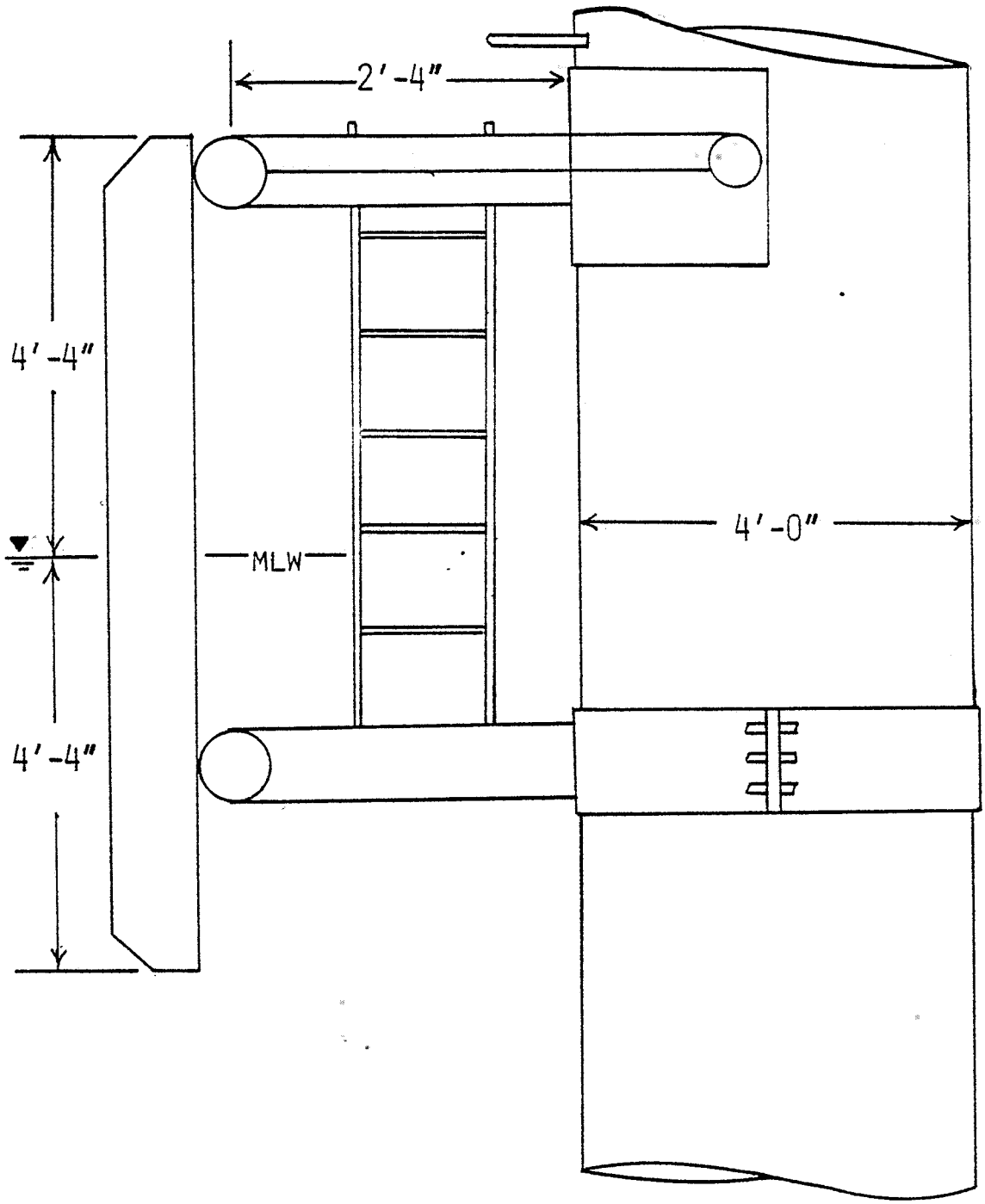

FIG. 2.4: ELEVATION VIEW OF BOAT LANDING AND CAISSON

the pile down to the mudline is a 6-5/8 inch diameter pipe which transports the produced gas to a neighboring platform. The pipe is held fixed by clamps which extend 20 inches from the outer wall of the pile. The pipe complicates the flow pattern around the pile and its effect will vary depending on the principal direction of the seas due to shielding of the large diameter pile. In total, however, the effect of the asymmetries and the additional outer members are not felt to be significant in the response prediction.

Another major reason for studying a caisson is its compliance. The AMOCO platform as described above has a natural period of over 3 seconds and a damping ratio of less than 1.5% in only 89 feet of water. For structures in the ocean with natural periods longer than 2 seconds, dynamic response may be substantial. For the Lollipop, essentially all of the response, except during the most severe wave conditions, is dynamic response of the first fundamental bending modes. Understanding, as well as predicting, the dynamic response of this relatively simple structure will yield valuable insights into the behavior of more complex deep water structures such as tension leg platforms and guyed towers.

As a first approximation, a single pile platform can be modelled as a fixed-free cantilever beam with a lumped mass at the free end. Analytical solutions of a fixed-free beam are well documented [Biggs, 1964], and yield some valuable insights. First, for a perfectly symmetric beam, the lowest two natural frequencies (eigenvalues) will be identical and

the corresponding mode shapes (eigenvectors) will be orthogonal to one another, but will not have a unique orientation. Phrased another way, one mode may be arbitrarily designated to vibrate in the x-z plane. The other fundamental bending mode would then be defined to vibrate in the y-z plane at the same natural frequency. Any other orthogonal pair of modes could also be defined. If the two natural frequencies are different then the orientation of the natural modes is uniquely defined.

Prior to any analysis, some of the response characteristics of the AMOCO caisson can be anticipated. Although not perfectly symmetric or fixed to the seafloor, significant response is probable only in the fundamental bending modes. The lowest natural frequencies should be almost identical, and significant response during low sea states is expected. The underlying soil at the site will also play a major role, as a soil foundation is not as stiff as a rigid foundation. The natural frequency calculated using a fixed-free beam model of the Lollipop, assuming constant mass and stiffness properties, will be an upper bound on the true value. Similarly, the stresses in the pile will be smaller than those calculated using this simple model. In the next chapter, a more sophisticated finite element idealization of the AMOCO caisson is discussed.

CHAPTER 3

STRUCTURAL IDEALIZATION

One of the first steps taken in the design of an offshore structure is to construct a realistic mathematical model of the structure. Throughout the design phase, this model is continually improved until the response characteristics of the model are satisfactory to the design team. In this thesis, a primary goal of the structural model was to see how well a relatively simple finite element model could replicate the observed dynamics of the AMOCO caisson. To achieve this goal, the sensitivity of the model to variations in mass, stiffness, and soil properties was studied to more accurately understand the dynamic behavior of the model. Finally, the model was subjected to sinusoidal excitation in order to obtain the relationship between platform motion and the maximum dynamic stress in the pile for use in a fatigue life calculation.

3.1 Description of the Model

In the course of this research, two finite element discretizations have been used to model the AMOCO caisson. The initial idealization, using 19 nodes, was a relatively crude model in two respects. The transition section of the pile, where the diameter increases from 4 to 7 feet, was not accurately modelled and the outer pile was assumed to have a uniform 1 inch thickness along its length. When it was dis-

covered that the pile was 1.375 inches thick at the mudline, a more accurate 21 node discretization was developed. Details of the initial model can be found in the 1980 report by Cook et. al.. The intricacies of the improved 21-node model will be discussed here.

The general purpose finite element analysis program ADINA (Automatic Dynamic Incremental Nonlinear Analysis) developed by Bathe [1975] was used. Although ADINA can be used for very complex nonlinear static and dynamic problems, it handles simple linear analysis just as capably. The discretization used to model the dynamic properties of the Lollipop incorporated 21 nodes, 16 beam elements, and 4 truss elements in a two-dimensional analysis with translational and rotational degrees of freedom (DOF) allowed. A schematic of the 21-node model is shown in Figure 3.1.

3.1.1 Pile Modelling

The pile was modelled using 2-node, 4 DOF beam elements, as described in the ADINA manual. The beam elements incorporated only translational and rotational DOF and were used to model the pile to a level 61 feet below the mudline. Beam element properties required for each beam group were mass density, moment of inertia, Young's modulus, Poisson's ratio, and the group's cross-sectional area. Beam elements 1 and 2 represented the decks. A simple frame analysis was used to approximate the bending rigidity of the decks. Concentrated masses were lumped at the upper 3 nodes to account for the total deck mass as derived from the structural

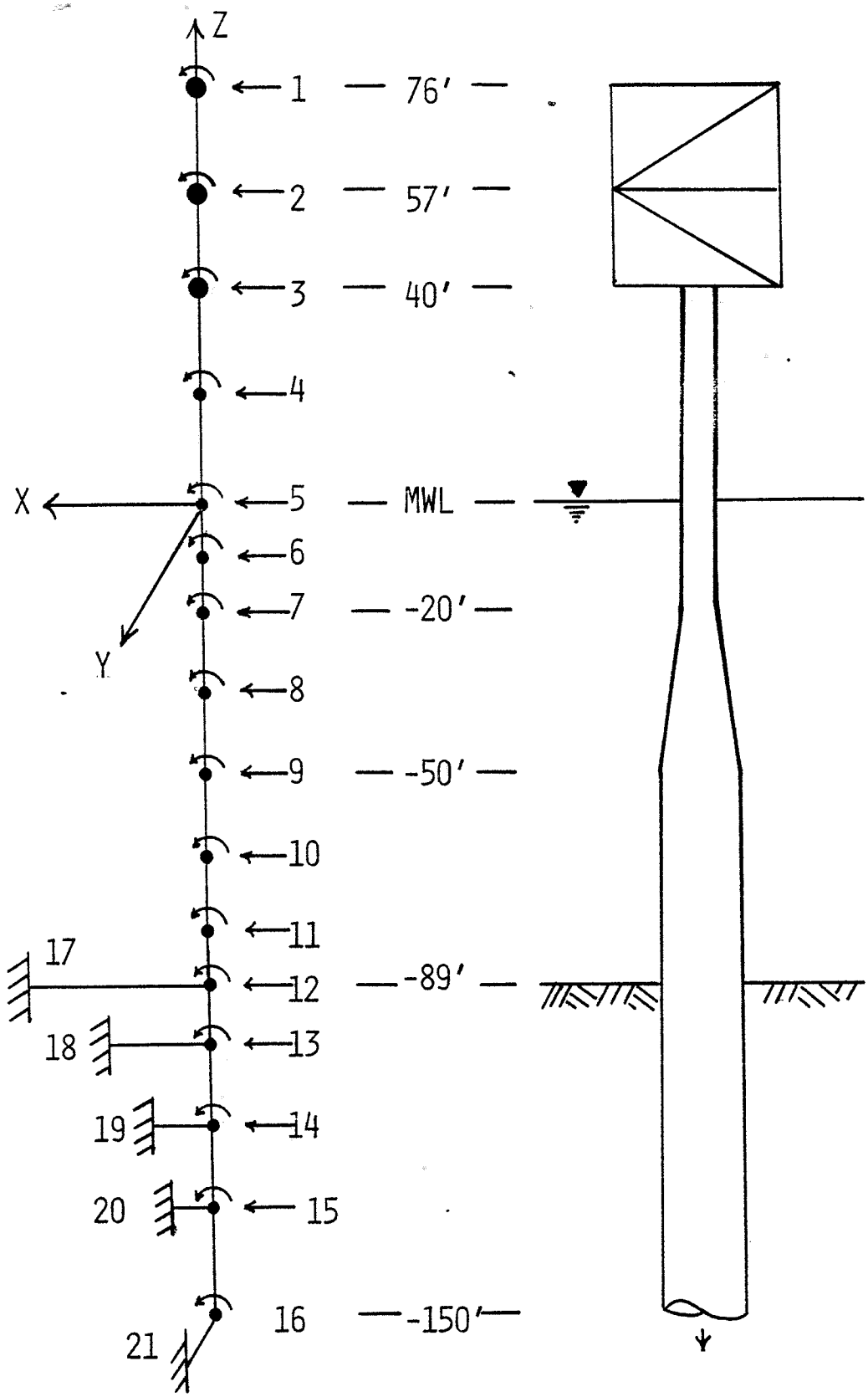

FIG. 3.1: 2-D SCHEMATIC OF 21-NODE F. E. MODEL

drawings.

Beam elements 3 through 15 represented the cumulative effects of the outer pile, the internal drill pipes, and the grout which fills the annulus between the outer pile and the 30 inch drive pile down to the mudline. Seven different beam element groups were required to adequately model the changing mass and inertia properties along the pile length. Determination of the bending rigidity, EI, of the pile was complicated by the presence of grout and was computed in the following way. An equivalent grout moment of inertia was calculated by dividing the bending rigidity of the grout by Young's modulus for steel. This equivalent moment of inertia was then added to the one calculated for the steel members. This method assumes that the bending rigidity of the grout is totally effective. In practice, the actual modulus of the grout will reduce due to crack formation under cyclic loading. Reducing the effectiveness of the grout is one of the variables in the sensitivity analysis which will be discussed later.

The diameter transition section of the pile, -20 to -50 feet, was discretized into 2 separate elements. The properties of the top element, beam element 7, were computed using the diameter at the midpoint of the element, which is 4.75 feet. For beam element 8 the average diameter of 6.25 feet was used. In a detailed finite element model, in which local stress concentrations were studied, a finer mesh is justified. Beam element 16 was employed as an equivalent rota-

tional spring and was included to represent the bending rigidity of the pile below -150 feet, since that part of the pile was not explicitly included in the model. Therefore, the terminal (lowest) node in the finite element model allows rotation but not translation.

A lumped mass matrix was used in the finite element formulations. For those elements of the pile in the water column, an added mass equal to the displaced volume of the outer pile was added to the structural mass. This is necessary in order to account for the additional inertia required to accelerate the platform in water. In the mass density calculation, a specific weight of 150 lb/ft^3 was assumed for the grout. In addition, below the mudline, it was assumed that the annulus between the outer pile and the drive pile was filled with material having a specific gravity of 2 and no virtual soil mass was added to the structural mass.

Three additional phenomena which influence the dynamic characteristics of the AMOCO caisson were not included in the finite element model. The first involves the use of a two-dimensional model with no vertical degree of freedom to simulate the response of a three-dimensional structure. A two-dimensional model simulates unidirectional loading which is often sufficient in the preliminary design phase. The vertical DOF was restrained, as vertical dynamic contributions are insignificant compared to horizontal motions. The static contribution to the stress in the pile can be easily calculated with knowledge of the structural mass. The second phen-

omenon not represented is the "p-delta" effect which arises when the pile is deflected laterally from the vertical. An additional moment is created equal to the weight of the continuum multiplied by the displacement from the centerline. This moment tends to increase the natural period of the structure. The third factor not included involves the inner drill pipes. These members are actually in tension, supported by the outer piles through the connection in the Xmas tree on the wellhead deck. This large tension force acts to shorten the natural period. In a final detailed design these phenomena should be accounted for.

3.1.2 Soil-Structure Modelling

Incorporating the effects of the soil into a dynamic finite element model of a pile-supported platform is a topic currently under active geotechnical research. For the structural dynamicist, the choice of a soil model represents the largest uncertainty in the finite element idealization. Recognizing these facts, the author chose to model the soil using a simplified p-y curve formulation based on existing design procedure and then to test this formulation in an extensive sensitivity analysis. In this way, the influence of the soil foundation on the dynamic behavior of the platform was easily obtained. Comparing these results with the response characteristics as measured in the field, provides a rough check on what the behavior of the soil at the site must have been, and also points to the importance of accurate soil-structure modelling when the possibility of significant dynamic response

exists.

The procedure followed to model the soil utilizes the p-y curve formulation presented by Matlock in 1970 and outlined in Poulos and Davis [1980] for soils under quasi-static loading. A p-y curve expresses the nonlinear relationship between lateral soil load (p) and soil deformation (y) at a location at the soil-pile interface. The method is based on results of lateral load tests done on instrumented piles. The method assumes that deflection is proportional to the cube of the ratio between the actual to ultimate loading. The scheme assumes a uniform level of soil loading p to calculate the properties of four linear soil springs which act at four locations along the pile. To account for the reduction of soil stiffness under cyclic loading, these quasi-static stiffnesses were reduced until the observed behavior was obtained.

Within the ADINA program, linear soil springs are represented using truss elements. The technique outlined below was employed to derive the soil spring stiffnesses and resulting truss element lengths. As mentioned above, the basic p-y curve equations were obtained from Poulos and Davis. It should be mentioned that several modifications of these equations have been proposed [Stevens and Audibert, 1979]. The basic procedure is as follows:

1) Calculate p_u, the ultimate soil resistance per unit length of the pile, at the four truss element locations, using the minimum at each depth of either.

$$p_u = (3 + \frac{\gamma Z_s}{C_u} + 0.5 \frac{Z_s}{d}) C_u d \quad (3.1)$$

or

$$p_u = 9 C_u d \quad (3.2)$$

where: C_u = undrained soil shear strength at depth z

γ = submerged effective unit weight of soil

d = diameter of pile (7 feet)

Z_s = vertical coordinate measured positive downward from the mudline

Values of C_u and γ were obtained from a soil boring taken at a site near the AMOCO caisson.

2) Compute y_{50}, the deflection at one-half the ultimate soil resistance, using

$$y_{50} = 2.5 \varepsilon_{50} d \quad (3.3)$$

where: ε_{50} = strain at one-half the ultimate stress as obtained from laboratory tests. A value of .015 was used.

3) Assume a value of p, a uniformly distributed lateral soil load, and compute the ratio p/p_u at each node. This ratio will decrease with depth as the soil strengths increase.

4) Calculate y, the lateral deflection of the pile, using

$$y = 8(p/p_u)^3 y_{50} \quad (3.4)$$

5) Compute ENL, the equivalent nodal point loading due to the distributed load p.

6) Calculate K_s, the linear soil spring stiffness at each node, using

$$K_s = \frac{ENL}{y} \quad (3.5)$$

7) Compute L_s, the length of the corresponding truss element, using

$$L_s = \frac{EA}{K_s} = \frac{1 \times 10^6}{K_s} \qquad (3.6)$$

where: E = Young's modulus of equivalent truss elements
= 1×10^6 lb/ft^2

A = cross-sectional area of equivalent truss element
= 1.0 ft^2.

This procedure was used with the initial 19-node model and very good results were obtained on the first attempt. However, when the more realistic 21-node model was run with the same soils, much different results were acquired. This prompted a thorough re-evaluation of the soil modelling and resulted in the sensitivity analysis discussed below.

3.2 Sensitivity Analysis

Once a finite element model has been thoroughly checked, parametric variations in key parameters are imposed in order to judge the quality of the model as an accurate representation of the real structure. For the AMOCO caisson, with knowledge of the measured natural periods and damping ratios, performance of the finite element model was judged on how well the model replicated the observed dynamics. Within the ADINA program, model performance was obtained through the solution of the eigenvalue problem for the lowest three normal modes, and then comparing these results with the measured data. The goal of the sensitivity analysis was to investigate the major uncertainties in the model, namely soil modelling and grout effectiveness, through parametric variations.

The sensitivity analysis incorporated a total of nine runs in which either soil stiffnesses or grout effectiveness factors were varied. The results of the parameteric study are shown in Table 3.1 and lead to the following conclusions. The soil modelling technique described earlier, which is based on quasi-static loading, greatly overpredicts the soil stiffnesses and is clearly inadequate under cyclic loading conditions. A more realistic soil-structure model is clearly warranted. The importance of accurate finite element modelling is clearly seen by comparing the first two runs. All things being equal, the behavior of the 19-node model was much different than that of the 21-node model. Reducing the grout effectiveness factor caused the natural periods to increase as was expected and a value of 0.5 was thought to be the most realistic. Based on these results, run #8 was selected as the most realistic model for use in the forced vibration run described in the next section. The lowest three mode shapes computed in run #8 are shown in Figure 3.2.

3.3 Performance of the Optimum Model

A forced vibration analysis, using the input parameters of run #8, was performed to establish the maximum stress/helideck displacement transfer function required for fatigue life estimation. Although any type of excitation can be used to obtain this transfer function, a sinusoidal force simulating the component of the wave spectrum at the platform's fundamental resonant frequency was employed. By using this type of excitation, first mode response of the platform is simu-

TABLE 3.1

RESULTS OF SENSITIVITY ANALYSIS

RUN #	OBSERVED	1*	2	3	4	5	6	7	8	9
G.E.		1.0	1.0	1.0	1.0	0.5	0.0	1.0	0.5	1.0
S_L@-89		10.0	10.0	18.62	18.62	18.62	18.62	18.62	18.62	18.62
S_L@-100		1.25	1.25	.71	2.50	2.50	2.50	5.0	5.0	10.0
S_L@-115		.333	.333	.093	.252	.252	.252	.504	.504	1.08
S_L@-130		.119	.119	.025	.084	.084	.084	.168	.168	.336
T_1(sec)	3.07	2.97	2.72	2.58	2.77	2.86	3.00	2.92	3.00	3.09
T_2(sec)	.83	.91	.85	.80	.86	.89	.94	.90	.94	.94
T_3(sec)	.3-.33	.30	.29	.27	.29	.31	.33	.30	.32	.32
ψ(-89)		.071	.065	.050	.068	.062	.055	.082	.075	.097

*19-node model

where GE = grout effectiveness factor

S_L = soil spring length used in ADINA (Ft)

T_i = computed natural period of ith mode

ψ(-89) = value of 1st mode shape at the mudline assuming a value 1.0 at the helideck

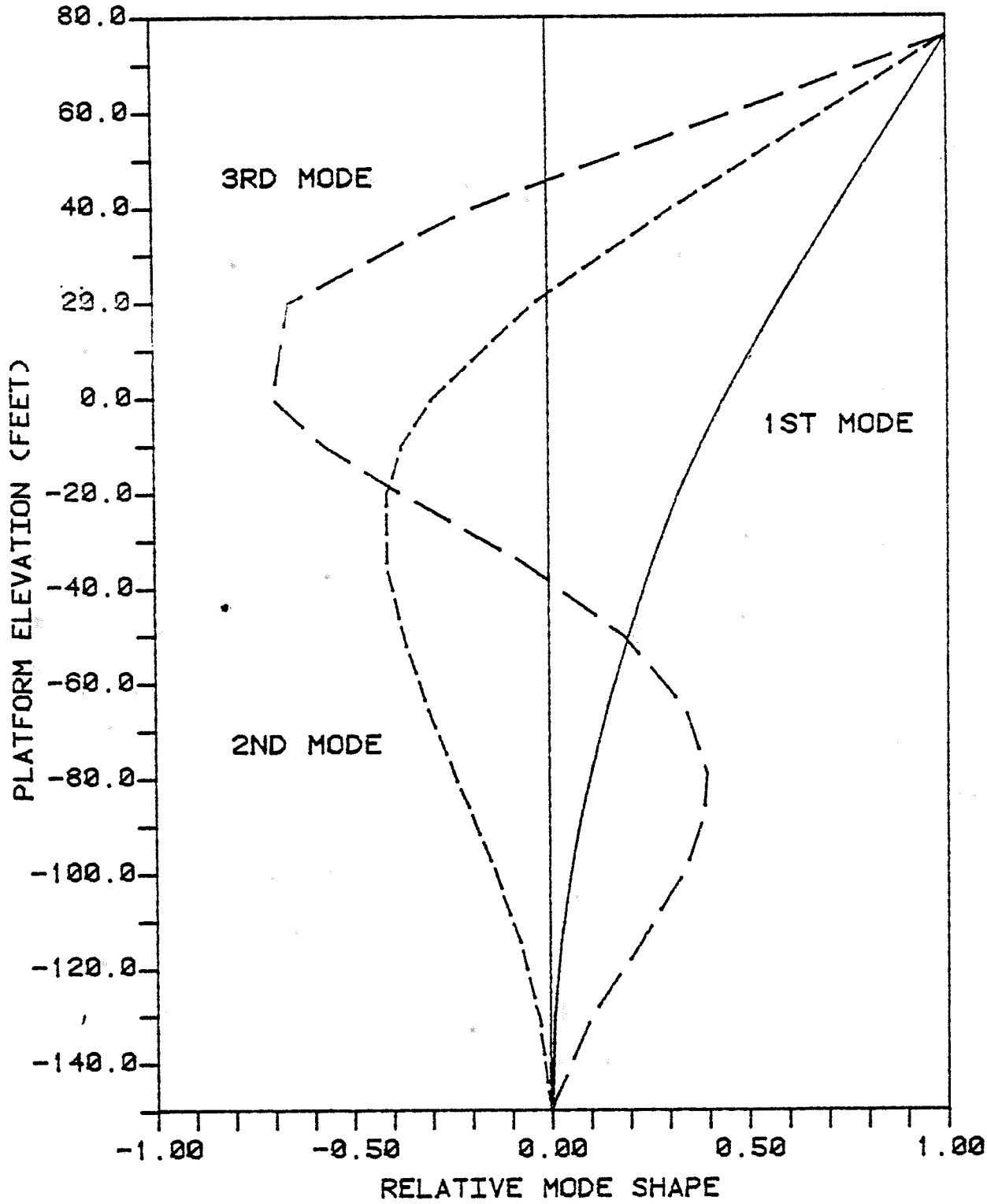

FIG 3.2: LOWEST THREE MODE SHAPES FROM FINITE ELEMENT RUN 8

lated. In addition, initial conditions were imposed to eliminate initial transients. For the AMOCO caisson, this required the input of initial velocities at all the nodes, with both initial displacements and accelerations equal to zero. With the initial velocity at node 1 specified, the remaining nodal initial velocities were calculated by multiplying the node 1 value by the first mode shape.

The technique of modal superposition [Bathe and Wilson, 1975] was used to solve the finite element equilibrium equations of the 21-node model. In this model, the 31 coupled equations of the 21-node model are transformed to an uncoupled set of equations in the normal modes. The forced vibration run was made using one mode with a damping ratio of 1.2% in the modal superposition analysis. With the goal of attaining a value of the dynamic stress to displacement transfer function due to motions in the fundamental bending mode, the use of a single mode is justified.

The Newmark method of integration, using a time step of 0.125 seconds, was utilized to integrate the dynamic equations. The Newmark method is an implicit unconditionally stable algorithm, details of which can be found in Bathe and Wilson. In the forced vibration run, forcing over one-half a response cycle was applied and the resulting output was used to calculate the maximum stress to helideck displacement transfer function. At each time step, the maximum dynamic stress (Smax) in the pile was determined from the maximum moment (Mmax) as output by ADINA using Equation 3.7.

$$Smax = \frac{Mmax\ r}{I} \qquad (3.7)$$

where: r = radius of the pile below the mudline = 3.5 feet

I = moment of inertia of the outer pile = 14.70 ft^4

The maximum dynamic stress in the pile is at a point 26 feet below the mudline, based on the finite element model results. In terms of the structure, the implication is that the top soil layers are very soft. The maximum stress to helideck displacement transfer function was next calculated at each time step by dividing Smax by the displacement at node 1. The transfer function values were essentially constant over the half cycle of loading indicating that the model behaved linearly. The average value of the transfer function to be used in the fatigue analysis is 4.952 ksi/ft.

In summary, the structural idealization of the AMOCO caisson resulted in a useful finite element model. Through the sensitivity analysis, valuable insights into the behavior of the platform under dynamic loading were obtained. The soil modelling technique proved inadequate in predicting the observed performance, thus warranting improvement in the soil-pile model. In conclusion, the two-dimensional finite element model developed here is a valuable tool in the interpretation and prediction of response for the Lollipop.

CHAPTER 4

SOURCES OF DAMPING

Accurate prediction of the dynamic response of a structure in the ocean requires knowledge of the various damping phenomena present. For this thesis it is convenient to use the technique of modal analysis to model the damping controlled response of each mode of the structure as an independent single degree of freedom (SDOF) system. This method has merit if the structure behaves linearly and the damping is small [Vandiver, 1979]. For the AMOCO caisson, which has significant damping controlled dynamic response at only one frequency, a SDOF equivalent model will yield total response estimates useful for preliminary design purposes. The sources of damping which will be included in the analysis are steel hysteretic damping, radiation (wave making) damping, viscous hydrodynamic damping, and soils damping. Each of these contributions to the total damping will be discussed in this chapter following a brief overview of the subject of damping.

In its broadest sense, damping is the removal of energy from a vibratory system either through internal dissipation or interactions with the environment [Crandall, 1970; Draper Labs, 1978, Campbell, R.B.]. Internal dissipation is the energy lost within a vibratory structural system due to inelastic behavior within the material and through the mechanical connections which bind the structure together. Steel hysteretic damping is of this type. Environmental interactions iden-

tify energy losses which arise in fluid-structure-soil interactions. The remaining three sources of damping identified in the previous paragraph fit this category. Damping is present within all structural systems and the level of damping determines the rate of decay of free vibrations and establishes an upper bound on the response of a vibratory system excited at resonance. Within the context of modal analysis, damping is specified for each normal node using an equivalent linear dashpot. For the AMOCO caisson, only the damping within the first fundamental bending mode will be estimated and then converted to the SDOF equivalent.

4.1 Steel Hysteretic Damping

Steel hysteretic damping refers to the energy lost due to internal dissipation within a steel member under cyclic loading. Several references on the characterization of material damping phenomena exist [Crandall, 1970; Lazan and Goodman, 1961; Draper Labs (Campbell), 1978] so only the major features required to obtain an estimate of the steel hysteretic damping for the AMOCO caisson will be presented here. The estimate will be obtained assuming energy dissipation is restricted to the outer pile which will yield a lower bound (conservative) estimate of the true steel hysteretic damping. The initial step requires the definition of three related material damping measures. The most fundamental measure is the unit damping energy D_u, which is the energy dissipated per cycle within a unit volume of material when that material is subjected to a sinusoidal uniaxial stress. Under these conditions, D_u equals

the area within the stress-strain hysteresis loop plotted over one cycle. A wealth of experimental evidence has indicated that for most structural materials D_u satisfies

$$D_u = JS_a^n \tag{4.1}$$

where: S_a = amplitude of sinusoidally varying uniaxial stress

J = function of temperature (for viscoelastic materials, also a function of excitation frequency)

n = constant, usually between 2 or 3.

The total damping energy D_s is the total energy dissipated in the material calculated by integrating D_u over the volume. The loss factor η_s is another damping parameter which is defined as

$$\eta_s = \frac{D_s}{2\pi U_s} = \frac{JE}{\pi} S_a^{n-2} \tag{4.2}$$

where: $D_s = \int_V D_u dV$

$U_s = \int_V \frac{S_a^2}{2E} dV$ = the peak strain energy density stored in the material during a cycle.

The final expression for the loss factor is valid for systems of a single material under uniaxial stress conditions, and it is independent of the stress level if n=2. Tabulated data [Lazan and Goodman, 1961] for SAE 1020 mild steel, which is the type of steel typically used offshore, indicates that n=2 and $J = 500 \times 10^{-12}$ (at room temperature) for cyclic stresses below 30 ksi. Substituting these values into Equation 4.2 yields

$$\eta_s = \frac{JE}{\pi} = .0047 \tag{4.3}$$

which is an estimate of the steel hysteretic damping within the outer pile of the Lollipop under cyclic loading. However, to utilize this result requires a transformation to the equivalent SDOF model which defines first mode response of the AMOCO caisson.

In the modelling of multi-degree-of-freedom systems, the classic solution has been to assign an equivalent linear dashpot to each mode of the structure by equating the dashpot loss factor, η_i, with the actual loss factor of the system when it oscillates in the i^{th} mode [Crandall, 1970]. Since the AMOCO caisson responds primarily in only its lowest fundamental modes

$$\eta_i = \eta_s = .0047 \tag{4.4}$$

A linear dashpot exerts a force $F_D = Rv$ proportional to and in phase with the relative velocity v between its terminals. The constant of proportionality, R, is termed the dashpot constant. In the SDOF equivalent system for the i^{th} mode,

$$M_i\ddot{q} + R_i\dot{q} + K_iq = F_i(t) \tag{4.5}$$

where: M_i = modal mass of i^{th} mode

R_i = total modal damping coefficient

K_i = total stiffness

q = generalized coordinate obtained by modal analysis for the particular mode

$F_i(t)$ = modal exciting force.

the loss factor, damping ratio, and natural frequency are defined as

$$\eta_i = \frac{R_i \omega_i}{K_i} \tag{4.6}$$

$$\xi_i = \frac{R_i}{2\sqrt{K_i M_i}} = \frac{R_i \omega_i}{2K_i} = \frac{R_i}{2M_i \omega_i} \tag{4.7}$$

$$\omega_i = (K_i/M_i)^{1/2} \tag{4.8}$$

where:

$2\sqrt{K_i M_i}$ = critical damping coefficient of i^{th} mode.

Substituting Equations 4.7 into 4.5 yields the familiar SDOF resonator equation for the i^{th} mode

$$\ddot{q} + 2\xi_i \omega_i \dot{q} + \omega_i{}^2 q = F_i(t)/M_i \tag{4.9}$$

Comparing Equations 4.6 and 4.7 yields the relationship between the loss factor and the damping ratio of the i^{th} mode.

$$\xi_i = \frac{1}{2} \eta_i \tag{4.10}$$

For the equivalent SDOF linear system representing the first mode of the AMOCO caisson, the damping ratio of the first mode is made up of the sum of four components.

$$\xi_1 = \xi_T = \xi_{ST} + \xi_{RAD} + \xi_{VH} + \xi_{SOIL} \tag{4.11}$$

where: ξ_{ST} = damping ratio due to steel hysteretic damping

ξ_{RAD} = damping ratio due to radiation (wave making) damping

ξ_{VH} = damping ratio due to viscous hydrodynamic damping

ξ_{SOIL} = damping ratio due to soils damping

The damping ratio due to steel hysteretic damping, ξ_{ST}, is

obtained by substituting Equation 4.4 into Equation 4.10.

$$\xi_{ST} = \frac{1}{2}\eta_i = .00235 \simeq .24\% \qquad (4.12)$$

Equation 4.12 is a lower bound estimate of the damping ratio due to steel hysteretic damping which occurs during 1st mode vibrations of the Lollipop.

4.2 Radiation (Wave Making) Damping

A platform oscillating in the ocean creates waves which radiate outward from the structure. This mechanism represents an energy loss to the system and is therefore a form of damping. The name usually associated with this phenomenon is radiation damping although the term wave making damping is also used. The linear SDOF equivalent radiation damping of the first mode of the AMOCO caisson can be estimated using either of two different methods. The first approach is to solve the linear potential flow problem for a cylinder oscillating in a calm sea. This solution is contained in a 1976 report by Petrauskas and the result will be recast here in a simpler form. The second approach utilizes the principle of reciprocity for ocean waves and it is fully described in a 1979 paper by Vandiver. The principle of reciprocity relates the radiation damping of a structure oscillating in a calm sea to the linear wave force exerted on the structure if it were held fixed in incident waves. Since viscous effects are not included in either formulation, the radiation damping as defined here is strictly a function of the inertial forces.

In the potential flow approach, the general expression for the modal radiation damping coefficient for a uniform cylinder in an irrotational inviscid fluid of depth h can be expressed as

$$R_{RAD}(\omega) = \frac{\pi d\ \rho_w\ \omega\ P_1(Kd/2)}{\sinh Kh \cosh Kh + Kh} \left[\int_{-h}^{o} \psi(Z) \cosh K(Z+h) dZ\right]^2 \quad (4.13)$$

where: d = cylinder diameter

ρ_w = density of water

ω = frequency of radiated waves

K = wave number

h = water depth

$\psi(Z)$ = mode shape

$P_1(Kd/2) = 2/(\pi K/2(J_1^1(Kd/2)^2 + Y_1^1(Kd/2)^2))$

J_1^1 and Y_1^1 are first derivatives of Bessel functions of the first and second kind, respectively.

The function $P_1(Kd/2)$ is plotted in Figure 4.1 versus Kd/2. For Kd/2 values less than 1/2 or greater than 2, $P_1(Kd/2)$ may be approximated as

$$P_1(Kd/2) = \frac{\pi}{2} \left(\frac{Kd}{2}\right)^3 \quad \text{for } \frac{Kd}{2} < \frac{1}{2} \quad (4.14)$$

or

$$P_1(Kd/2) = 1.0 \text{ for } Kd/2 > 2 \quad (4.15)$$

An expression applicable for deep water radiated waves can be obtained from Equation 4.13 using the deep water disper-

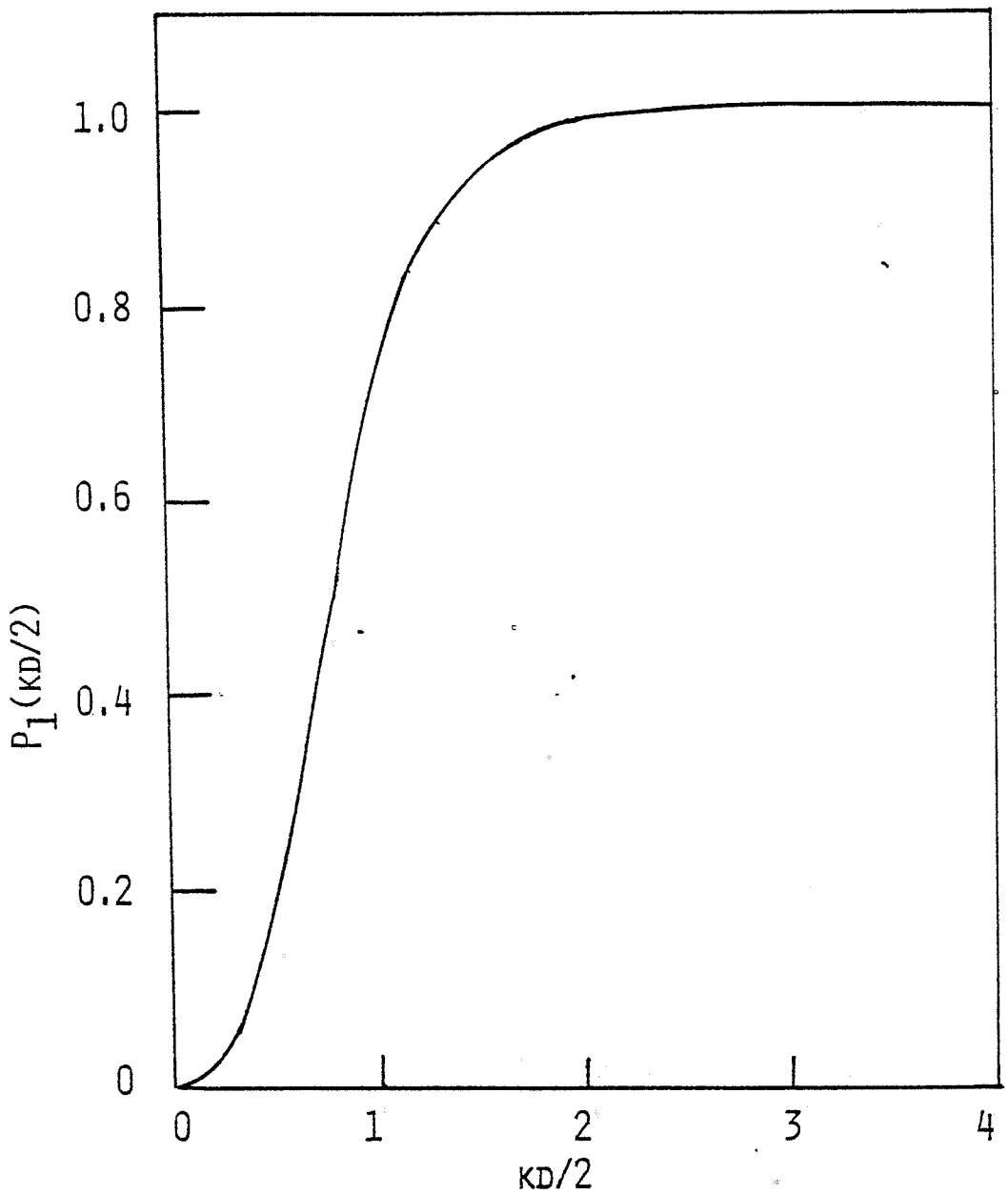

FIG. 4.1: $P_1(KD/2)$

sion relation $K = \omega^2/g$ and noting that $\sinh Kh \sim \cosh Kh \sim 1/2 e^{Kh}$.

$$R_{RAD}(\omega) = \frac{\pi d\, \rho_w\, \omega\, P_1(Kd/2)}{e^{2Kh} + 4Kh} \left[\int_{-h}^{o} \psi(Z) e^{K(Z+h)} dZ \right]^2 \qquad (4.16)$$

For "back of the envelope" estimates, Equation 4.16 can be simplified if the first mode of the cylinder is approximated with a simple analytic expression. For example, for a linearly varying mode shape, $\psi(Z) = 1+Z/h$, normalized to have a value of 1.0 at the free surface, Equation 4.16 becomes

$$R_{RAD}(\omega) = \frac{\pi d\, \rho_w\, \omega P_1(Kd/2)}{K^2} (1 - 1/Kh)^2 \qquad (4.17)$$

which holds for deep water waves. Equation 4.17 can be employed to calculate the modal radiation damping ratio using the modal mass associated with the same linear mode shape.

The AMOCO caisson oscillates at approximately 2.048 radians/second (.326 Hz, 3.07 seconds) in first mode resonant response creating deep water radiated waves in 89 feet of water. Since the major contribution to the radiation damping occurs in the near surface zone, an estimate of the modal radiation damping coefficient was initially obtained by evaluating Equation 4.16 numerically with the following inputs:

$d = 4$ feet, $\rho_w = 1.988$ lb-sec^2/Ft^4, $\omega = 2.048$ rad/sec

$K = .1303$ 1/ft, $h = 89$ feet, $P_1(Kd/2) = .0278$

$\psi(Z)$ from Run #8 of F.E. model

to yield:

$R_{RAD}(2.048) = 14.03$ lb-sec/ft

$$\xi_{RAD}(2.048) = .102\% \sim .10\%$$

For a non-uniform diameter the expression for the modal radiation damping coefficient becomes

$$R_{RAD}(\omega) = \frac{\pi\rho_w \omega}{e^{2Kh} + 4Kh} \left[\int_{-h}^{o} dP_1\left(\frac{Kd}{2}\right)\psi(Z)e^{K(Z+h)}dZ\right] \cdot \left[\int_{-h}^{o} \psi(Z)e^{K(Z+h)}dZ\right] \qquad (4.18)$$

Evaluating Equation 4.18 numerically using the same parameters as above yields

$$R_{RAD}(2.048) = 14.03 \text{ lb-sec/ft}$$

$$\xi_{RAD}(2.048) = .108\% \sim .11\%$$

which is only slightly different from the uniform diameter result. The true value of the radiation damping ratio is probably higher than these estimates due to the presence of the boat landing in the surface zone.

The alternate approach, using the principle of reciprocity to estimate the modal radiation damping, was originally developed by Haskind and cast in a usable form by Newman. As given by Vandiver [1979], the Haskind/Newman relation for the modal radiation damping coefficient is

$$R_{RAD}(\omega) = \frac{\omega^3}{4\pi\rho_w g^3} \int_o^{2\pi} \frac{|F(\omega,\theta)|^2}{|A(\omega,\theta)|^2} d\theta \qquad (4.19)$$

where $F(\omega,\theta)$ = modal exciting force exerted on a fixed body of deep water regular waves of frequency ω and amplitude $A(\omega,\theta)$ incident at an angle θ.

g = acceleration of gravity

If $F(\omega,\theta)$ is assumed to be due to inertial forces only, then the expression for the modal radiation damping becomes

$$R_{RAD}(\omega) = \frac{\pi^2 \omega^7 \rho_w C_M^2}{64\ g^3} \left[\int_{-h}^{o} \psi(Z)\ d^2\ e^{KZ} dZ \right]^2 \qquad (4.20)$$

where C_M = inertia coefficient from Morison's equation. Evaluating Equation 4.20 numerically using the same parameters as shown earlier yields

$$R_{RAD}(\omega) = 3.473\ C_M^2 \qquad (4.21)$$

If the inertia coefficient is assumed to be a constant equal to 2, the estimate for the modal radiation damping in the first mode of the AMOCO caisson becomes

$$R_{RAD}(2.048) = 13.89 \text{ lb-sec/ft}$$

$$\xi_{RAD}(2.048) = .107\% \sim .11\%$$

This result, which assumes the modal force is due strictly to inertia effects, is virtually identical with the potential flow results, so that either method could be used to estimate the modal radiation damping.

4.3 Viscous Hydrodynamic Damping

In the previous section, it was observed that the radiation damping was dependent on the inertia forces. In an analogous way, the viscous hydrodynamic damping is related to the separated-flow drag force term in Morison's equation. As stated in a report by Dunwoody and Vandiver in 1981, the separated-flow drag force influences the response of an offshore structure by producing an excitation proportional to

the incident flow field, a damping which increases with sea state, and an additional excitation term related in a complex fashion to the fluid and structural motion. An expression for the modal viscous hydrodynamic damping coefficient for first mode response of a vertical cylinder can be found in the 1980 thesis by Dunwoody to be

$$R_{VH} = \int_{-h}^{o} \frac{1}{2} \rho_w C_D d \sqrt{\frac{8}{\pi}} \sigma_r (Z) \psi^2(Z) dZ \qquad (4.22)$$

where C_D = drag coefficient

σ_r = root mean square relative velocity

Since R_{VH} is dependent on the relative velocity, an exact solution of Equation 4.22 requires iteration. To avoid this, an approximate solution can be obtained if the structural velocities are much smaller than the fluid particle velocities. When this is the case, the r.m.s. water particle velocity at depth z, $\sigma_u(Z)$, can be computed using

$$\sigma_u^2(Z) = \int_o^\infty \omega^2 G_\eta(\omega) e^{2KZ} d\omega \qquad (4.23)$$

where $G_\eta(\omega)$ = incident wave spectrum.

This expression is valid for deep water linear waves which decay exponentially. It is apparent in Equation 4.23 that the magnitude of the viscous hydrodynamic damping as defined in Equation 4.22 is proportional to the incident wave spectrum which causes the damping to increase with sea state.

To estimate the modal viscous hydrodynamic damping for the AMOCO caisson, the root mean square water particle velocity was calculated using a Bretschneider two-parameter wave

spectrum defined as

$$G_{\eta}(\omega) = \frac{1.25}{4} H_S^2 \frac{\omega_p^4}{\omega^5} \exp\left(-1.25 \frac{\omega_p^4}{\omega^4}\right) \qquad (4.24)$$

where H_S = significant wave height (feet)

ω_p = peak wave frequency (rad/sec)

Replacing the r.m.s. relative velocity by the r.m.s. water particle velocity in Equation 4.22, estimates of the modal viscous hydrodynamic damping for several unidirectional wave spectra were obtained.

The results are shown in Table 4.1 as a function of C_D for each of the four measured wave spectra discussed in Chapters 7 and 8 as well as estimates for one lower and two higher sea states. These values were computed numerically employing the same mode shape as in the previous section. The estimates of the modal viscous hydrodynamic damping ratio are probably upper bounds on the true values for a bare cylinder since a unidirectional wave spectrum was used to compute the incident water particle velocities. For the AMOCO caisson, however, these results are likely to be representative of the true values due to the presence of the boat landing in the surface zone.

TABLE 4.1

MODAL VISCOUS HYDRODYNAMIC DAMPING RATIOS

REEL NO.	H_s (ft)	T_p (sec)	C_D=.8 ξ_{VH}(%)	C_D=1.0 ξ_{VH}(%)	C_D=1.2 ξ_{VH}(%)
1*	2.5	6.0	.08	.11	.13
3	4.12	7.28	.13	.17	.20
4	3.32	6.79	.11	.14	.16
5	3.59	7.10	.12	.15	.18
6	3.80	7.10	.12	.16	.19
	10.0	8.0	.33	.41	.49
	20.0	9.0	.63	.79	.95

*H_s and T_p estimated from visual data for Reel #1.

4.4 Soils Damping

Soils damping refers to the energy dissipated within the soil mass under cyclic loading of a pile-supported offshore structure. Compared with the other components of the total damping discussed previously, the characterization and modelling of soils damping is more complex and less well established. A literature survey was conducted and it was learned that damping within the soil is usually modelled as the imaginary term of a complex stiffness [Blaney, et. al., 1976; Angelides and Roesset, 1980; Novak and Nogami, 1977, etc.]. Two possible damping sources were identified; material (internal) soil damping and geometric (radiation) damping. Material soil damping is hysteretic damping and is usually specified for a particular soil mass with a constant soils damping ratio. Geometric damping is analogous to the wave making damping discussed previously. Geometric damping is possible only if the frequency of oscillation exceeds a threshold value which depends on the soil stratum at a given location. In this section, a simple technique is developed to evaluate the energy dissipated in the soil surrounding the AMOCO pile when it oscillates in the first mode.

The modal soils damping is estimated by relating the total energy dissipated in the soil during a cycle with the soils material damping ratio. No attempt is made to explicitly model geometric damping. As mentioned above, a soils damping ratio constant with depth is typically assigned to a soil stratum. This damping ratio corresponds to an assumed equi-

valent uniformly distributed linear dashpot along the length of the pile. For a linear dashpot, the relationship between the damping ratio, in this case ξ_{smd}, and the damping capacity $\Psi(Z)$ is given by

$$\Psi(Z) = \frac{D_z(Z)}{U_z(Z)} = 4\pi\xi_{smd} \qquad (4.25)$$

where $D_z(Z)$ = energy dissipated per unit length along the pile per cycle

$U_z(Z)$ = peak strain energy stored in the soil per unit length along the pile per cycle.

If the stiffness of the soil is modelled using distributed linear soil springs, as was done in the finite element model described in Chapter 3, $U_z(Z)$ becomes

$$U_z(Z) = \frac{1}{2} k_{soil}(Z) \; X_p^2(Z) \qquad (4.26)$$

where $k_{soil}(Z)$ = soil stiffness per unit length

$X_p(Z)$ = peak lateral displacement of the pile

Substituting Equation 4.26 into Equation 4.25 and solving for $D_Z(Z)$ yields

$$D_Z(Z) = 2\pi\xi_{smd} \, k_{soil}(Z) \, X_p^2(Z) \qquad (4.27)$$

The total energy dissipated within the soil D_{TS} is then obtained by integrating Equation 4.27 over the pile length

$$D_{TS} = 2\pi\xi_{smd} \int_z k_{soil}(Z) \, X_p^2(Z) dz \qquad (4.28)$$

The modal equivalent of Equation 4.28, applicable when the AMOCO caisson vibrates in the x^{th} mode with a maximum helideck displacement of a_o is

$$D_{TS} = 2\pi\xi_{smd}\, a_o^2 \int_z k_{soil}(Z)\psi^2(Z)\, dZ \qquad (4.29)$$

Using the 4 lumped soil springs from the finite element model changes the integration in Equation 4.29 to the summation in Equation 4.30.

$$D_{TS} = 2\pi a_o^2\, \xi_{smd} \sum_{i=1}^{4} K_s(Z_i)\psi^2(Z_i) \qquad (4.30)$$

where K_s = lumped soil stiffness at $Z = Z_i$

$\psi(Z_i)$ = value of the mode shape at $Z = Z_i$

Equation 4.30 represents the energy dissipated in the soil when the Lollipop oscillates in mode X with a peak helideck displacement of a_o. The final step in this technique is to calculate the soils damping coefficient R_{SOIL} of the equivalent SDOF system by equating energy losses. The energy loss associated with R_{SOIL} in the equivalent SDOF system is

$$D_{eq} = \pi a_o^2\, \omega_x R_{SOIL} \qquad (4.31)$$

where D_{eq} = energy loss per cycle due to soils damping

ω_x = natural frequency of the x^{th} mode

Equating Equations 4.30 and 4.31 and solving for R_{SOIL} yields

$$R_{SOIL} = \frac{2\xi_{smd}}{\omega_x} \sum_{i=1}^{4} K_s(Z_i)\psi^2(Z_i) \qquad (4.32)$$

which corresponds to a SDOF equivalent damping ratio of

$$\xi_{SOIL} = \frac{\xi_{smd}}{M\,\omega_x^2} \sum_{i=1}^{4} K_s(Z_i)\psi^2(Z_i) \qquad (4.33)$$

where ξ_{SOIL} = equivalent soils damping ratio of SDOF system.

Equation 4.33 was evaluated for the fundamental mode of the AMOCO caisson using the same mode shape, modal mass and natural frequency as used in the previous sections. The corresponding values for K_s were calculated from the soil spring lengths L_s given in Table 3.1 for run #8. The estimates of modal soils damping coefficient and damping ratio are shown in Table 4.2 for a typical range of soils material damping ratios ξ_{smd}.

The estimates in Table 4.2 are indicative of the range of soils damping parameters which contribute to first mode response of the AMOCO caisson. In the next section, the results of the previous four sections are summarized to judge the relative contributions of each damping source to the total modal damping.

4.5 Damping Summary

In the previous sections of this chapter, estimates of the four primary sources of damping applicable to first mode vibrations of the AMOCO caisson have been developed. In Chapter 8, estimates of the equivalent total modal damping are derived for both orthogonal fundamental modes from the acceleration time histories of a biaxial pair of accelerometers. In this section, the primary sources of damping are combined with the total damping estimates obtained by analyzing the responses of the Lollipop on three different days. The results are shown in Table 4.3

The total modal damping ratio estimate was obtained by

TABLE 4.2

MODAL SOILS DAMPING ESTIMATES

ξ_{smd} (%)	R_{SOIL} (lb-sec/ft)	ξ_{SOIL} (%)
2	45.56	.35
3	68.33	.53
4	91.11	.70
5	113.89	.88
6	136.67	1.06
8	182.23	1.41
10	227.78	1.76

TABLE 4.3

DAMPING SUMMARY

MODAL DAMPING* RATIO ESTIMATES(%)	Reel 1		Reel 3		Reel 4	
	Mode x	Mode y	Mode x	Mode y	Mode x	Mode y
1. ξ_T - Total	1.1+/-.3	1.3+/-.3	1.0+/-.4	1.4+/-.4	.9+/-.2	1.1+/-.3
2. ξ_{ST} - Steel	0.24	0.24	0.24	0.24	0.24	0.24
3. ξ_{RAD} - Radiation	0.11	0.11	0.11	0.11	0.11	0.11
4. ξ_{VH} - Viscous	0.11	0.11	0.17	0.17	0.14	0.14
5. **$\xi_T - (\xi_{RAD}+\xi_{VH}+\xi_{ST})$	.64	.84	.48	.88	.41	.61
6. ξ_{soil} for $\xi_{smd} = 0.03$	0.53	0.53	0.53	0.53	0.53	0.53
7. ξ_{soil} for $\xi_{smd} = 0.05$	0.88	0.88	0.88	0.88	0.88	0.88

*Items 2, 3, 4, 6, and 7 were theoretically obtained. Item 1 is an experimental value.

**This is the soils damping required to make the total experiment damping value equal the total theoretical. The values shown suggest that an average value for ξ_{SOIL}=0.6%.

isolating the principal modal directions and then using MEM spectral analysis to compute the damping ratio estimate and its variance. The confidence bounds on the estimates of ξ_T are 95% confidence limits. Details of the estimation of ξ_T are presented in Chapter 8. For the component sources of damping, ξ_{ST} is a lower bound estimate since only energy dissipation within the outer pile is considered. Alternatively, ξ_{VH} is probably an upper bound on the true value since it is calculated using a unidirectional wave spectrum. However, when the drag effects of the boat landing are factored in, the estimate of ξ_{VH} becomes more representative of the true value. Two soils damping ratios are shown which correspond to different assumed values of ξ_{smd}. The experimental data suggests that ξ_{SOIL} equals 0.6% which is approximately 60% of the total modal damping.

Several conclusions are evident from the data presented in Table 4.3. First, the sum of the theoretical estimates for the four sources of damping are, for almost all the modes, contained within the 95% confidence limits of the total damping estimate. Second, the relative magnitudes of each source of damping are probably indicative of the actual behavior with the soils damping estimate the least certain. The soils account for more than 1/2 of the total. Finally, the characterization of damping as it affects the dynamic response of a structure is not an automatic exercise. A consistent model of the structure which properly incorporates the damping phenonema applicable to the problem is a necessity if reli-

able response predictions are to be obtained. In the next chapter, a method to predict the damping controlled response of an offshore structure to random wave excitation is presented.

CHAPTER 5

DAMPING CONTROLLED RESPONSE PREDICTION

In this chapter, the mean square damping controlled dynamic response of the AMOCO caisson to random wave excitation will be estimated using the method proposed by Vandiver in 1979. This technique utilizes the principle of reciprocity which was introduced in Section 4.2. The performance of the method will be evaluated by comparing the predictions to the responses measured in the field and described in Chapters 7 and 8. In addition, the influence of wave spreading on the predicted responses of the two orthogonal fundamental nodes will be delineated. A simple analysis of vortex shedding will conclude the chapter.

5.1 Reciprocity Method

The reciprocity method for predicting the damping controlled dynamic response of an offshore structure in a random sea, proposed by Vandiver in 1979, will be employed here. This technique yields a simple result for the mean square modal response and its use is valid only for lightly damped modes excited by linear wave forces. Linear wave forcing neglects drag effects, therefore the method will yield accurate results only for those modes in which inertia forces dominate. Although drag forces are neglected, modal damping due to separated flow drag is included. As given by Vandiver, the expression for the mean square dynamic response of the

x^{th} mode within two half-power bandwidths of the resonant frequency ω_x is

$$\sigma_x^2 = \frac{2.5\ C_x \rho_w\ g^3}{M_x \omega_x^5}\ G_\eta(\omega_x)\ \frac{R_{RAD}(\omega_x)}{R_T(\omega_x)} \qquad (5.1)$$

where σ_x^2 = mean square dynamic deflection in x^{th} mode

M_x = modal mass

$G_\eta(\omega_x)$ = wave elevation spectral ordinate at ω_x

$R_{RAD}(\omega_x)/R_T(\omega_x)$ = ratio of radiation to total damping of the x^{th} mode

The term C_x depends both on structural geometry and the directional wave spectrum, as well as being weakly dependent on frequency. The determination of C_x for the AMOCO caisson will be presented in the next section.

Equation 5.1 written in terms of cyclic frequency f_x is

$$\sigma_x^2 = \frac{C_x\ \rho_w\ g^3}{80\pi^5 M_x f_x^5}\ G_\eta(f_x)\ \frac{\xi_{RAD}}{\xi_T} \qquad (5.2)$$

where: $f_x = \omega_x/2\pi$

$G_\eta(f_x)$ = wave spectral ordinate in cyclic frequency domain evaluated at f_x

ξ_{RAD}/ξ_T = ratio of radiation to total damping ratio for the x^{th} mode

To aid in the comparison with the measured platform accelerations, the relationship between accelerations and displacements of a narrow band process

$$\sigma_{\ddot{x}}^2 = \omega_x^4\ \sigma_x^2 = 16\pi^4 f_x^4 \sigma^2 x \qquad (5.3)$$

where: $\sigma^2_{\ddot{x}}$ = mean square acceleration response of the x^{th} mode

was employed to yield

$$\sigma^2_{\ddot{x}} = \frac{2.5\ C_x\ \rho_w\ g^3}{M_x \omega_x} G_\eta(\omega_x)\ \frac{R_{RAD}(\omega_x)}{R_T(\omega_x)} \tag{5.4}$$

$$\sigma^2_{\ddot{x}} = \frac{C_x\ \rho_w\ g^3}{5\pi\ M_x f_x} G_\eta(f_x)\ \frac{\xi_{RAD}}{\xi_T} \tag{5.5}$$

The performance of the method was evaluated for the AMOCO caisson by comparing the predicted mean square acceleration of each of the orthogonal fundamental bending modes, termed mode x and mode y, using Equation 5.5 with the measured mean square accelerations of Reels 3 and 4. To achieve a meaningful comparison, values of C_x and C_y were computed, as described in the next section, and the spectral ordinate $G_\eta(f_x)$ was obtained from the measured wave spectra. In addition, the ratio ξ_{RAD}/ξ_T was formed using the value of ξ_{RAD}, estimated in Chapter 4, with ξ_T obtained from the data analysis. The wave forces which excite the fundamental mode of the AMOCO caisson are inertia dominated so the reciprocity method is clearly applicable. The results are shown in Table 5.1 with the predicted and measured mean square helideck accelerations in close agreement. Based on these results, the reciprocity method is a viable, easily applicable technique to predict the modal response of a structure excited by linear wave forces.

5.2 Accounting for Wave Spreading

A realistic description of the wave environment at a location in the ocean must account for randomness in both

TABLE 5.1

COMPARISON OF PREDICTED AND MEASURED HELIDECK ACCELERATION RESPONSES

	Reel #3		Reel #4	
	Mode x	Mode y	Mode x	Mode y
$G_\eta(f)$ (ft^2/Hz)	1.2	1.2	.7	.7
C_i	1.56	.44	1.37	.63
$\xi_T(\%)$	1.0+/-.4	1.4+/-.4	.9+/-.2	1.1+/-.3
ξ_{RAD}/ξ_T	.110	.079	.122	.100
$f_i(Hz)$	.323	.328	.323	.327
σ^2_{xp} (ft^2/sec^4)	.85 (.61-1.42)	.17 (.13-.24)	.48 (.36-.72)	.18 (.15-.22)
σ^2_{xm} (ft^2/sec^4)	.71	.20	.49	.23

M = 3162 lb-sec^2/ft=101,815.5 lb_m

ρ_w = 1.988 lb-sec^2/ft^4

g = 32.2 ft/sec^2

ξ_{RAD} = .11%

σ^2_{xp} = predicted mean square helideck acceleration

σ^2_{xm} = measured mean square helideck acceleration

amplitude and direction of the incoming waves. The reciprocity method described in the previous section incorporates directional effects through the constant C_x, which is a function of the directional wave spectrum $G_\eta(\omega,\theta)$, where θ is the wave incidence angle. The directional wave spectrum is related to the incident point wave spectrum $G_\eta(\omega)$ by

$$G_\eta(\omega) = \int_0^{2\pi} G_\eta(\omega,\theta)\,d\theta \tag{5.6}$$

In most applications, $G_\eta(\omega,\theta)$ is assumed to be separable into distinct functions of ω and θ.

$$G_\eta(\omega,\theta) = G_\eta(\omega)D(\theta) \tag{5.7}$$

where $D(\theta)$ = spreading function.

As given by Vandiver (1979), the expression for C_x

$$C_x = \frac{\int_0^{2\pi} G_\eta(\omega,\theta)\,|\Gamma_x(\omega,\theta)|^2 d\theta}{G_\eta(\omega)\,\frac{1}{2\pi}\int_0^{2\pi} |\Gamma_x(\omega,\theta)|^2 d\theta} \tag{5.8}$$

where: $\Gamma_x(\omega,\theta)$ = the modal wave force per unit wave amplitude for mode x, for a regular wave of frequency ω and incidence angle θ.

is dependent solely on structural geometry. For a single pile platform, $\Gamma_x(\omega,\theta)$ can be written as separable functions of ω and θ

$$|\Gamma_x(\omega,\theta)| = |\Gamma(\omega)\cos\theta| \tag{5.9}$$

where: $\Gamma(\omega)$ = the maximum modal wave force per unit wave amplitude.

Substituting Equations 5.7 and 5.9 into 5.8 simplifies the expression for C_x.

$$C_x = 2\int_0^{2\pi} D(\theta)\cos^2\theta\,d\theta \tag{5.10}$$

If mode x and mode y are used to describe the two fundamental flexural modes of the Lollipop, the expression for C_y is computed in the same fashion, utilizing

$$|\Gamma_y(\omega,\theta)| = |\Gamma(\omega)\sin\theta| \tag{5.11}$$

to yield

$$C_y = 2\int_0^{2\pi} D(\theta)\sin^2\theta d\theta \tag{5.12}$$

Values of C_x and C_y for three different spreading functions (unidirectional, omnidirectional, and cosine-squared) are shown in Table 5.2, when the x mode is lined up with the mean direction of the seas. The fourth spreading function shown below is described in a 1980 report by Vandiver.

$$D(\theta-\theta_o) = \frac{\sqrt{1-e^2}}{2\pi(1-e\cos(\theta-\theta_o))} \tag{5.13}$$

where θ_o = mean direction of the seas

e = eccentricity of an ellipse, $0 \leq e \leq 1.0$.

The spreading function described by Equation 5.13 plots a family of ellipses in a polar coordinate system. The values of e corresponding to the 3 other spreading functions are also shown in Table 5.2. The spreading function defined in Equation 5.13 is normalized to insure that the relationship between the point wave amplitude spectrum and the directional wave spectrum, as delineated in Equation 5.6, is satisfied. Table 5.3 contains values of C_x and C_y as a function of e when the x-mode is in line with the mean direction of the seas (θ_o=0). Values of C_x and C_y used in the previous section

TABLE 5.2

C_X AND C_Y FOR UNIDIRECTIONAL, OMNIDIRECTIONAL AND COSINE-SQUARED WAVE SPREADING

Type of Spreading	$D(\theta)$	C_x	C_y	e
Unidirectional	$\delta(\theta)$	2.0	0.0	1.0
Cosine-squared	$\frac{2}{\pi}\cos^2\theta$	1.5	0.5	.95
Omnidirectional	$\frac{1}{2\pi}$	1.0	1.0	0.0

TABLE 5.3

C_X AND C_Y AS A FUNCTION OF e

e	C_x	C_y
0	1.0	1.0
.5	1.07	.93
.7	1.16	.84
.8	1.24	.76
.85	1.31	.69
.87	1.34	.66
.89	1.37	.63
.90	1.39	.61
.95	1.52	.48
.96	1.56	.44
.99	1.74	.26
1.0	2.0	0

to predict response levels, were produced from an estimate of e using the technique outlined in Section 8.3.2. From the results of this section, it is clear that directionality in the seas excites both fundamental modes of the AMOCO caisson.

5.3 Influence of Vortex Shedding

Another possible source of excitation for a cylindrical structure in the ocean is vortex shedding. In this section, the vortex shedding phenomenon due to wave effects is addressed in an attempt to delineate the boundary point above which excitation, due to vortex shedding, is possible for the AMOCO caisson. In comparison with the steady flow case, the behavior of a cylinder in a wave environment is more complex.

In order for vortex shedding to occur, it is anticipated that the orbital amplitude of the water particles must be on the order of the diameter of the cylinder. This corresponds to a Keulegan-Carpenter number of 2π for regular waves. The Keulegan-Carpenter number for regular waves is given by

$$K.C. = \frac{U_m T}{d} = \frac{2\pi A}{d} \tag{5.19}$$

where U_m = maximum water particle velocity

T = wave period

d = pile diameter

A = wave amplitude

Sarpkaya, 1976, has shown that for K.C.<5 transverse forces on a smooth cylinder in a uniform oscillating flow are negligibly small.

Much less is known about the generation of transverse forces in a directionally spread random wave environment. One measure of the likelihood of significant transverse forces is given by a root mean square Keulegan-Carpenter number [Dunwoody, 1980]

$$K.C. = \frac{\sigma_u T_m}{d} \qquad 5.15)$$

where σ_u = r.m.s. water particle velocity

T_m = mean period of the wave spectrum

For the worst case sea conditions observed in these field experiments, the r.m.s. K.C. number was approximately 2. Lift forces were insignificant.

CHAPTER 6

DYNAMIC RESPONSE FATIGUE LIFE ESTIMATION

For offshore structures experiencing significant dynamic response in "everyday" sea states, the governing design criteria is often the prevention of failure caused by low-stress, high cycle fatigue. In this chapter, a method is developed to estimate the rate of accumulation of fatigue damage due to first mode dynamic response of the AMOCO caisson. The fatigue accumulation model employed assumes that the stress history is a narrow band Gaussian process with Rayleigh distributed stress peaks [Crandall and Mark, 1963]. Utilizing a stress range S-N curve,

$$SN^b = c \tag{6.1}$$

the equation for the mean rate of accumulation of fatigue damage is

$$F = \frac{\nu_o^+}{c} (2^3 \sigma_s^2)^{b/2} \Gamma(1+b/2) \tag{6.2}$$

where F = mean rate of accumulation of fatigue damage at a location in the structure which experiences a mean square stress σ_s^2

ν_o^+ = average zero upcrossing rate of the stress process

$\Gamma(\ )$ = the Gamma function

N = mean number of cycles to failure for stress range S

b, c = constants of the S-N curve utilized.

Implicit within this equation is the Palmgren-Miner rule for fatigue damage accumulation. This model is assumed to

be valid for the purposes of this thesis.

To estimate the fatigue life of the AMOCO caisson, the maximum mean square stress within the outer pile as a function of platform dynamics and wave characteristics must be known. The relationship between platform deflections and maximum stress has already been estimated with the finite element model described in Chapter 3. In particular, the transfer function between the maximum stress in the pile and helideck displacements was found to be 4.952 ksi/ft. for first mode response. Mathematically, the relationship between the maximum stress in the pile and helideck displacements can be expressed as:

$$\sigma_s^2 = B^2 \sigma_x^2 \tag{6.3}$$

where B = 4.952 ksi/ft.

σ_x^2 = mean square helideck displacement for mode x

Wave characteristics are incorporated in the fatigue accumulation model using the reciprocity method to estimate the mean square modal response given by Equation 5.2.

$$\sigma_x^2 = \frac{C_x \rho_w g^3}{80\pi^5 M_x f_x^5} G_\eta(f_x) \frac{\xi_{RAD}}{\xi_T} \tag{5.2}$$

Combining Equations 5.2 and 6.3

$$\sigma_s^2 = B^2 \frac{\rho_w g^3}{80\pi^5} \left[\frac{C_x}{M_x f_x^5} \frac{\xi_{RAD}}{\xi_T} G_\eta(f_x) \right] \tag{6.4}$$

yields an expression for σ_s^2 which depends on the directionality in the seas, the incident wave spectrum, modal mass,

modal frequency, and the ratio of radiation to total damping.

Conducting a fatigue analysis for an offshore structure requires knowledge of the wave characteristics at the site. The typical treatment uses past wave data to develop significant wave height (H_s) and peak wave period (T_p) pairs each with an assigned probability of occurrence, to represent the long term statistics of the sea. Each pair is then substituted in a theoretical wave spectrum and the cumulative rate of fatigue damage, weighted by the probability of occurrence, is summed over all pairs. In this thesis, the equation used for the fatigue life estimate (FLE) is

$$FLE = 1/\sum_{i=1}^{J} F_i P_i \tag{6.5}$$

where F_i = mean rate of accumulation of fatigue damage due to sea state i

P_i = annual probability of occurrence of sea state i expressed as a fraction of 1 year

J = total number of sea states.

Utilizing a Bretschneider two-parameter wave spectrum

$$G_\eta(f) = \frac{1.25}{4} H_s^2 \frac{f_p^4}{f^5} e^{-1.25(f_p/f)^4} \tag{6.6}$$

where f_p = peak wave frequency = $1/T_p$

the expression for the maximum mean square stress becomes

$$\sigma_s^2 = \frac{1.25B^2\rho_w g^3}{320\pi^5} \left[\frac{C_x H_s^2}{M_x} \frac{f_p^4}{f_x^{10}} \frac{\xi_{RAD}}{\xi_T}\right] e^{-1.25(\frac{f_p}{f_x})^4} \tag{6.7}$$

Substituting Equation 6.7 into the fatigue accumulation

model as defined in Equation 6.2 yields a general expression for the mean rate of accumulation of dynamic response fatigue damage in mode x caused by sea state i.

$$F_i = \frac{f_x}{c}\left[\frac{B^2\rho_w g^3}{32\pi^5}\ \frac{C_x H_s^{\,2}}{M_x}\ \frac{f_p^{\,4}}{f_x^{\,10}}\ \frac{\xi_{RAD}}{\xi_T}\ e^{-1.25\left(\frac{f_p}{f_x}\right)^4}\right]^{b/2}\Gamma(1+b/2) \tag{6.8}$$

where $\nu_o^+ = f_x$.

In this equation, all the parameters which affect the fatigue life estimate are present, except for the probability of occurrence of the sea state. Careful selection of the input parameters of Equation 6.8 is required because fatigue life estimates are extremely sensitive to small variations in the inputs.

The fatigue life was estimated for the AMOCO caisson using one set of parameters with the twelve Gulf of Mexico sea states given in a 1979 report by Kinra and Marshall. For this estimate, the modal mass and modal frequency were assumed constant over the lifetime of the structure. The ratio ξ_{RAD}/ξ_T was fixed at .2 for all the sea states. The selection of a value for C_x was not straightforward since modal directions change with time, since the AMOCO caisson exhibits no preferred modal orientation. In addition, given the truly two-dimensional response of the Lollipop, all locations on the circumference of the pile should have similar stress histories. For the initial fatigue life estimate, C_x was set equal to 1.0 which corresponds to omnidirectional seas. The

AWS-X modified S-N curve applicable for steel members was used to obtain b and c.

The results are outlined in Table 6.1. The fatigue life of 161.1 years should be treated as a baseline estimate. For instance, with C_x equal to 2.0, which corresponds to unidirectional seas, the fatigue life decreases to 35.3 years. With C_x=1.0 and ξ_{RAD}/ξ_T= 0..5, the fatigue life is 21.7 years. Using sea states other than those given in Table 6.1 will also influence the fatigue life estimate.

Incorporating the reciprocity method into the fatigue accumulation model given by Equation 6.2 yields a simple expression which includes all the important features contributing to the fatigue of a dynamically-responding structure. One factor excluded in this analysis is the contribution of large long period storm waves to fatigue. Such waves are responsible for the quasi-static response of the platform which was not included in the dynamic response analysis given above. Although the number of such waves expected in the life of the structure is small, the damage per cycle may be quite large. In a detailed fatigue analysis, both quasi-static and dynamic contributions to the accumulation of fatigue damage should be included.

TABLE 6.1

DYNAMIC RESPONSE FATIGUE LIFE ESTIMATE USING THE RECIPROCITY METHOD

SEASTATE	H_s (ft)	T_p (sec)	P_i	σ_x^2 (ft^2)	$\sigma_s^2 (ksi)^2$	F_i	$F_i P_i$
1	40	16.92	.000001	.0771	1.890	.0358	3.58×10^{-8}
2	29	14.10	.000114	.0839	2.057	.0431	4.92×10^{-6}
3	26	14.10	.000387	.0674	1.653	.0267	1.03×10^{-5}
4	21	12.69	.000546	.0669	1.641	.0263	1.44×10^{-5}
5	16	11.28	.00387	.0621	1.522	.0223	8.63×10^{-5}
6	11	9.87	.0273	.0498	1.222	.0138	3.76×10^{-4}
7	7	9.87	.0464	.0202	.495	.0019	8.83×10^{-5}
8	7	7.05	.0464	.0750	1.838	.0337	1.56×10^{-3}
9	4	8.46	.1752	.0121	.296	.0006	1.09×10^{-4}
10	4	5.64	.1752	.0560	1.374	.0178	3.12×10^{-3}
11	2	7.05	.1752	.0061	.150	.0001	2.45×10^{-5}
12	2	4.94	.3493	.0220	.541	.0023	8.07×10^{-4}
							$\Sigma = 6.21 \times 10^{-3}$

$$FL = \frac{1}{\sum_{i=1} F_i P_i} = \frac{1}{6.21 \times 10^{-3}} = 161.1 \text{ years}$$

$c = 2.639 \times 10^{11}$

$b = 4.38$

CHAPTER 7

DESCRIPTION OF THE FIELD TEST PROGRAM

In March of 1980, Professor Vandiver and the author spent one week recording both environmental and response data on the AMOCO caisson which stands in South Marsh Island (SMI) Block 33 in the Gulf of Mexico. Prior to commenting on the details of the trip, it is a necessity to acknowledge the AMOCO personnel who made the trip a reality. Al Knapp and Ken Blenkarn were supportive of the proposed research and obtained approval for the experiment. Don Green, an engineer in AMOCO's New Orleans office, took charge of all logistical matters and accompanied the team to the field. His aid was invaluable and the week of work went smoothly because of his effort. In addition, the AMOCO field personnel headquartered on SMI 50B also contributed greatly to the success of the test program by providing food, overnight lodging, and logistical support.

The goal of the test program was to simultaneously measure platform accelerations, wave elevations, wind speeds, and currents in a variety of different combinations in order to learn as much as possible about the response characteristics of a single pile platform in a random sea. Specifically, answers were sought to the following questions. Is the platform's total response the sum of two unique orthogonal bending modes and if so can they be isolated? What are the natural frequencies and damping ratios of these as well as higher

modes? How important is wave spreading to the response of the Lollipop and can it be measured? Prior to the trip, some response data from the Lollipop had already been published [Hong, Brooks, 1976] and this information has served as a useful comparison to results presented here. In the next chapter, these and other questions are addressed.

7.1 Instrumentation

The instrumentation used in the field consisted of four accelerometers, a wave staff, an anemometer, an acoustic current meter and a 4-channel FM tape recorder. The accelerometers, ENDEVCO model QA116-16, are force-balance accelerometers with a dynamic range between +/- 1 g, resolution to 10^{-6}g and a sensitivity, including external amplification, of 100 volts per g. Each is housed with a separate preamplifier in a water-resistant case about the size of a large hand-held calculator and measures accelerations along one axis. Typically, two accelerometers were set up as a biaxial pair taped to the deck in the center of the platform with one accelerometer pointing platform east and the other, platform north.

The wave staff used is of the capacitance type which converts sea level fluctuations into voltages. The staff consists of two sections. The detection circuitry is located in a cylindrical case from which the wave probe extends down into the water. At the heart of the detection circuitry are two Colpitts oscillators, one acting as a reference signal to the other, the latter having a frequency dependent on the variable capacitance of the wave probe. The wave probe is

simply an insulated wire in which the wire and the water act as the two plates of the capacitor and the insulation is the dielectric. The wave staff was lowered over the edge of the wellhead deck until the probe was approximately at its zero calibration point. The staff was then tied off to the railing on the wellhead deck. A heavy weight was attached to the lower end of the wave staff to minimize lateral motions of the probe. The wave staff calibration was 0.89 volts per foot of wave elevation.

An anemometer was used to determine the wind speed at a point on the structure. A simple four cup rotary anemometer was used which produces an ac signal whose amplitude is a function of the wind velocity. The anemometer was calibrated in the MIT Acoustics and Vibrations Lab wind tunnel by Peter Stein, a graduate student. The wind speed to frequency calibration is $u = 1.41f + 1$ for u in knots and f in cycles per second. In the field, the anemometer was placed six feet above the wellhead deck on the north side of the structure for the first two measurements and then moved to a location 10 feet above the wellhead deck, three feet inside the east edge. Neither location was free from turbulence caused by wind interacting with the structure.

A Neil Brown two-axis acoustic current meter was also brought along in an effort to measure the water particle velocity field around the platform. However, after some brief success on the second day, the current meter connector was damaged preventing use of the unit for the remainder of

the trip. The initial results indicated that no mean current was present and that the water particle velocities were wave induced.

Data was recorded with a 4-channel Tandberg Model 100 FM tape recorder. The recorder uses standard 1/4 inch tape and has six input voltage settings for each channel ranging from +/-0.5 volts to +/-20 volts. The output range for any input range is +/-5 volts. A small screen on the front of the tape recorder shows the input level of each channel thus simplifying the choice of input voltage range and allowing the user to preview the recorded signal. Channel four of the recorder was also used to record voice commentary. The frequency reproduction of the recorder is very good with errors less than .1% between recorded and playback signal. All of the data was recorded at 1 7/8 ips.

7.2 Test Summary

A brief descriptive summary of the itinerary during the 1980 test program is outlined below:

March 23 - Professor Vandiver and the author travelled from Boston to New Orleans to Lafayette, Louisiana.

March 24 - Travelled by helicopter from Intracoastal City to the AMOCO caisson. Recorded the first reel of data.

March 25 - Two more reels of data recorded. Current meter was tested and briefly deployed.

March 26 - Adverse weather conditions prevented travel to the Lollipop.

March 27 - Adverse weather conditions prevented travel to the Lollipop.

March 28 - Returned to the AMOCO caisson to find the current meter cable damaged. Recorded the final three reels of data.

March 29 - Poor weather conditions complicated off-loading of equipment from the Lollipop. The MIT team was split up; the author and half of the equipment reached shore, Prof. Vandiver was forced to remain offshore as the weather deteriorated.

March 30 - Prof. Vandiver and the author regroup in New Orleans and return to Boston in the afternoon.

The specifics of each recorded reel of data and the environmental conditions at that time are schematically represented in Figures 7.1 - 7.3.

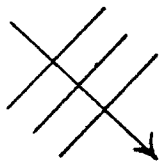

REEL 1

3-24-80: 1510-1645

1-3 FEET

20 KNOTS

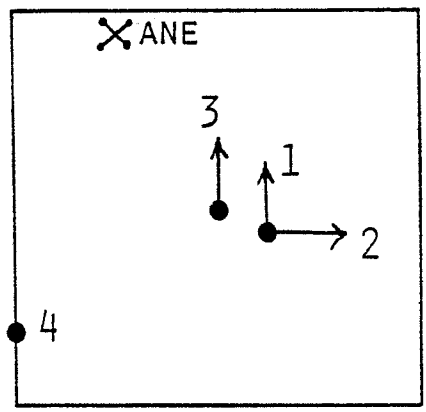

1 - NAP
2 - EAP
3 - NAW
4 - WSE

KEY

1,2,3,4	- CHANNEL NO.	ANE	- ANEMOMETER
NA, EA	- NORTH, EAST ACCELEROMETER	WSE	- WAVE STAFF
H , P	- ON HELIDECK, PROD. DECK	T	- TORSION
W , B	- ON WELLDECK, BOAT LANDING		

REEL 2

3-25-80: 0900-1118

1 - NAH
2 - NAP
3 - NAW
4 - NAB

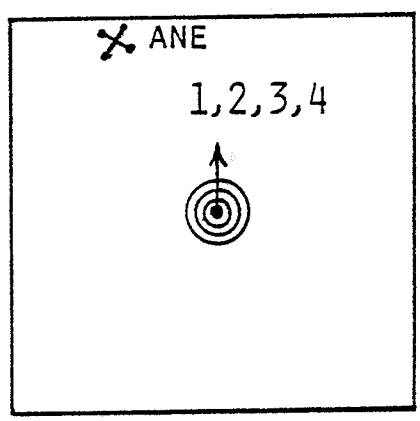

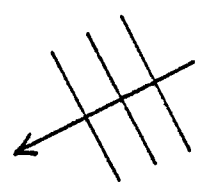

5-8 FEET

20 KNOTS

FIG. 7.1: SUMMARY OF FIELD TESTS 1 & 2

REEL 3

3-25-80: 1130-1400

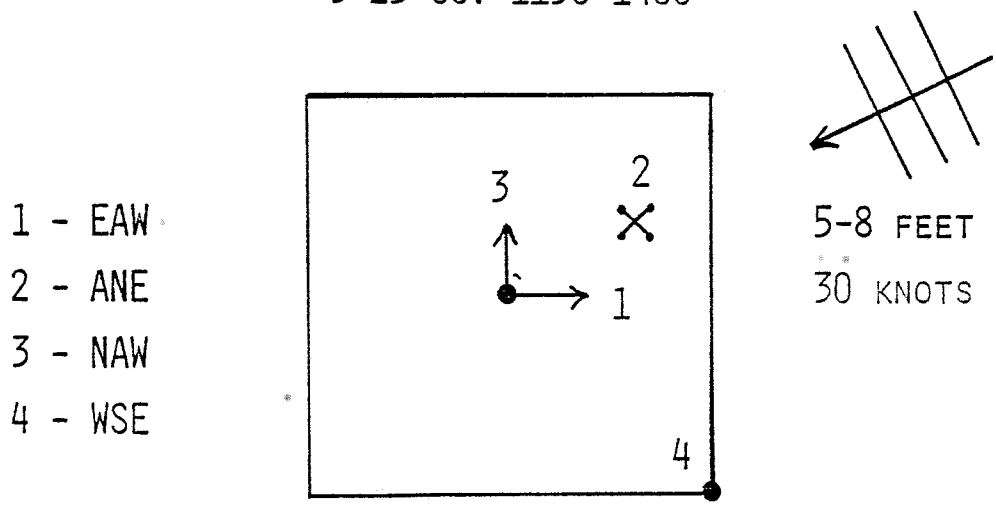

REEL 4

3-28-80: 1050-1210

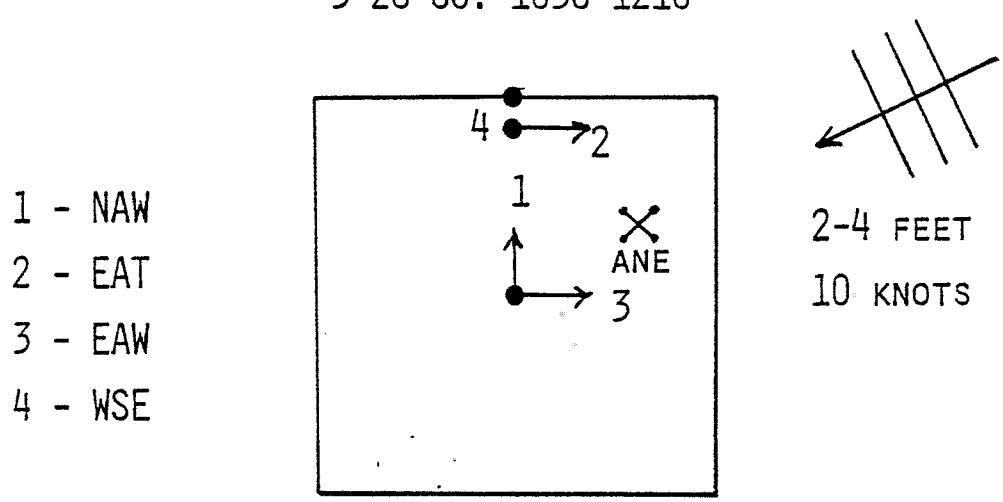

FIG. 7.2: SUMMARY OF FIELD TESTS 3 & 4

REEL 5

3-28-80: 1450-1615

1 - NAW
2 - EAW
3 - ANE
4 - WSE

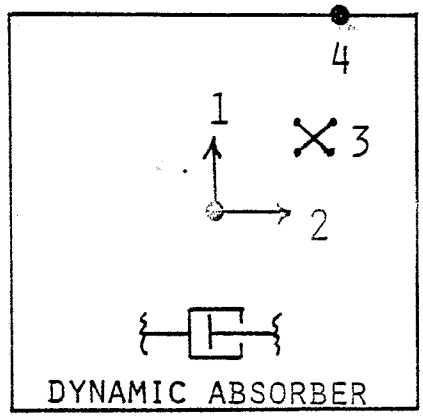

20 KNOTS
3-5 FEET

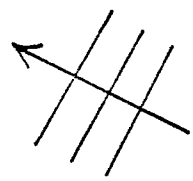

REEL 6

3-28-80: 1630-1715

1 - NAW
2 - EAW
3 - ANE
4 - WSE

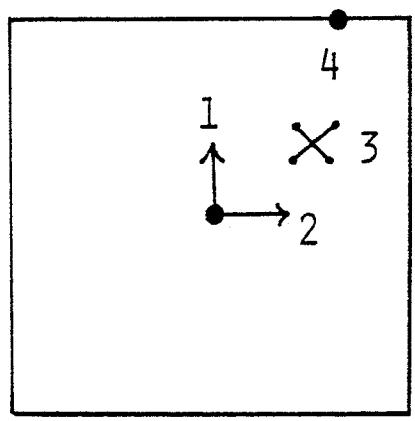

20 KNOTS
3-5 FEET

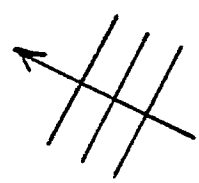

FIG. 7.3: SUMMARY OF FIELD TESTS 5 & 6

CHAPTER 8

RANDOM DATA ANALYSIS

In this chapter, the analysis performed on the data recorded in March, 1980, is described. The primary goals of the data analysis were: (1) to extract estimates of natural frequencies, damping ratios, and mean square responses of the platform response acceleration time histories; (2) to compute wave spectra, and to derive significant wave heights and peak wave periods from the recorded sea surface fluctuations; and (3) to investigate the relationships between pairs of accelerometers to identify spatial platform response characteristics.

8.1 Preliminary Data Processing

All of the data processing was done using a Gen-Rad marketed Time/Data system which combines a 4-channel 10-bit A/D converter with a Digital PDP-11/34 minicomputer. The Gen-Rad supplied software uses TSL (Time Series Language) to perform a variety of time series analysis related tasks. The only TSL program used in this analysis is a program called SCRIBE which handles the A/D conversion. As described in Chapter 7, six reels of data, each containing four channels, were recorded in March, 1980. All the accelerometer and wave data was digitized using SCRIBE with a sampling frequency of 6.4 Hz.. Each tape was previewed prior to the conversion to determine the maximum usable length of data. Also, during the conversion sequence, the output levels of each channel were moni-

tored to insure that no spurious data or voice transmission would be converted. The data was stored in blocks of 512 points and dc-coupling was used to avoid attenuation of low-frequency components. The output of the SCRIBE program is a TSL data file which contains the digitized output voltages of each channel. A summary of the A/D conversion of each reel is shown in Table 8.1.

Following the A/D conversion, an unformatted direct access FORTRAN file is produced for each channel using the program TRANSL. Next, each file is converted to zero-mean, using the program BZERO, to remove any input offsets which may have been present during the original recording. The data is then scaled to convert the tape recorder voltage outputs back into the proper engineering units. The scale factors applicable to each channel are shown in Table 8.2. The preliminary data processing is finished once all the channels have been properly scaled. Simultaneous wave elevation and EAW and NAW accelerometer time histories from reel 3 are shown in Figures 8.1 - 8.3. The wave elevation record has the distinct characterisitcs of a Gaussian wide band process while the response time histories are representative of narrow band processes.

8.2 Single-Channel Spectral Analysis

The method of spectral analysis used in this thesis is the Maximum Entropy Method (MEM). This method was introduced by Burg in 1967 and it is a nonlinear, data adaptive

TABLE 8.1

SUMMARY OF A/D CONVERSION

REEL NO.	CHANNELS DIGITIZED	TOTAL RECORD LENGTH (min)	TOTAL NUMBER OF POINTS PER CHANNEL	NUMBER OF 512 PT. BLOCKS PER CHANNEL
1	NAP*, EAP	88.0	33,792	66
2	NAH, NAP, NAW, NAB	81.33	31,232	61
3	EAW, NAW, WSE	106.67	40,960	80
4	NAW, EAT, EAW, WSE	81.33	31,232	61
5	NAW, EAW, WSE	65.33	25,088	49
6	NAW, EAW, WSE	44.0	16,896	33

* Defined in Figure 7.1

TABLE 8.2

SCALE FACTORS

REEL NO.	INPUT VOLTAGE	CHANNELS SCALED	SCALE FACTOR
1	+/-5	EAW,NAW	A
2	+/-10	NAH,NAP NAW,NAB	B
3	+/-10 +/-5	EAW,NAW WSE	B C
4	+/-10 +/-5	EAW,NAW,EAT WSE	B C
5	+/-10 +/-5	EAW,NAW WSE	B C
6	+/-10 +/-5	EAW,NAW WSE	B C

A = 0.332 ft/sec^2/volt

B = 0.644 ft/sec^2/volt

C = 1.124 ft/volt

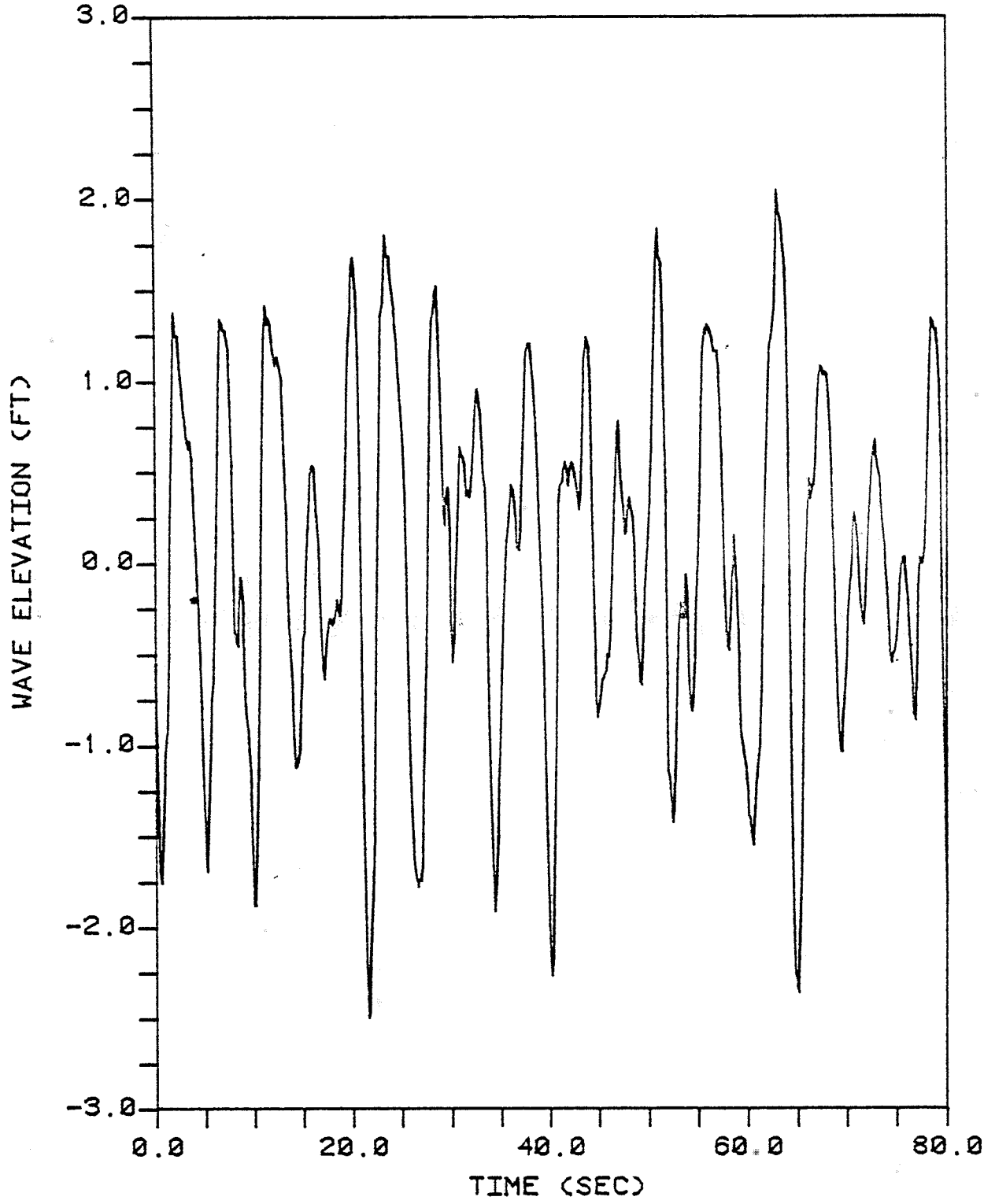

FIG 8.1: REEL 3 WAVE ELEVATION TIME HISTORY

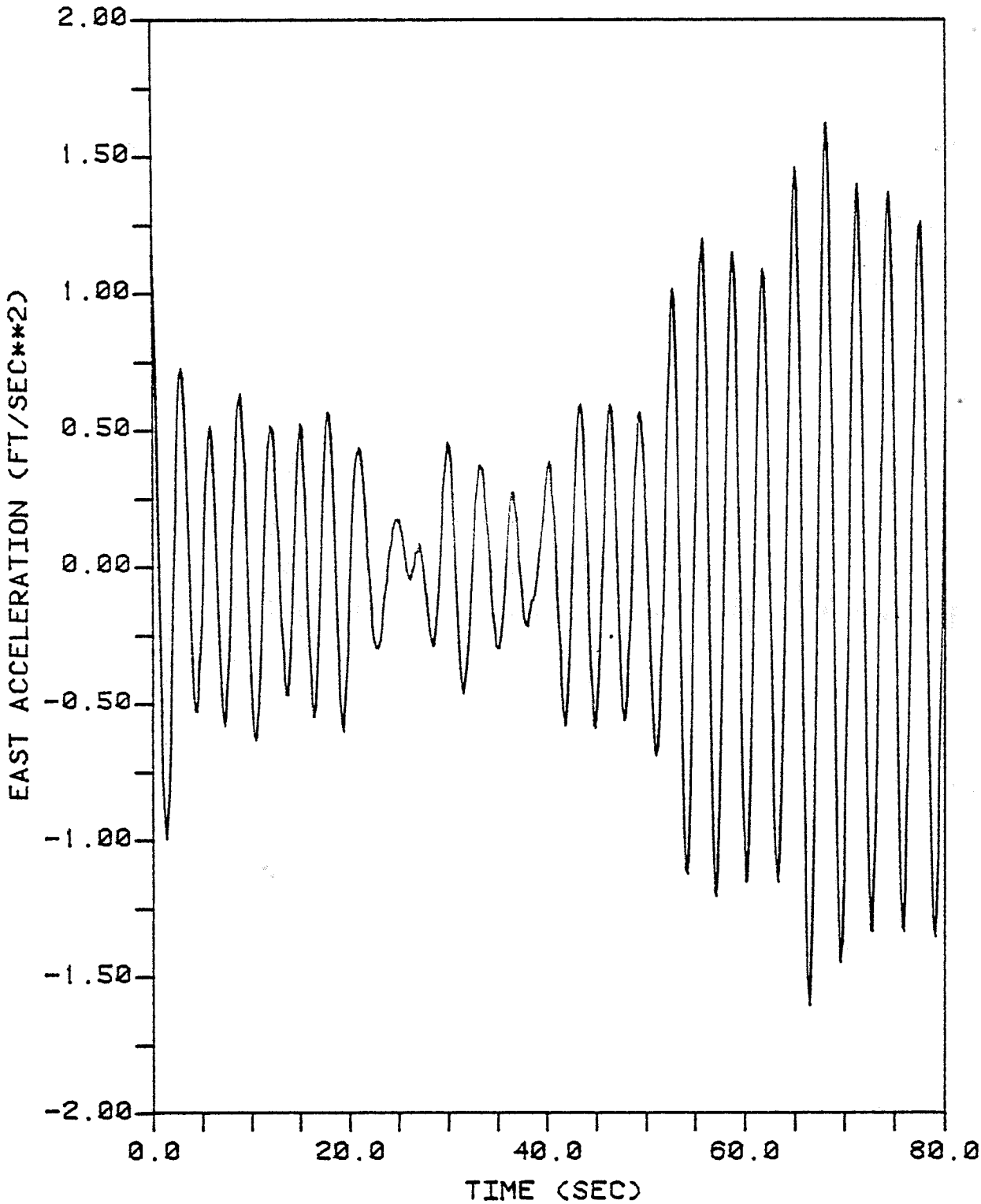

FIG 8.2: REEL 3 EAW ACCELEROMETER TIME HISTORY

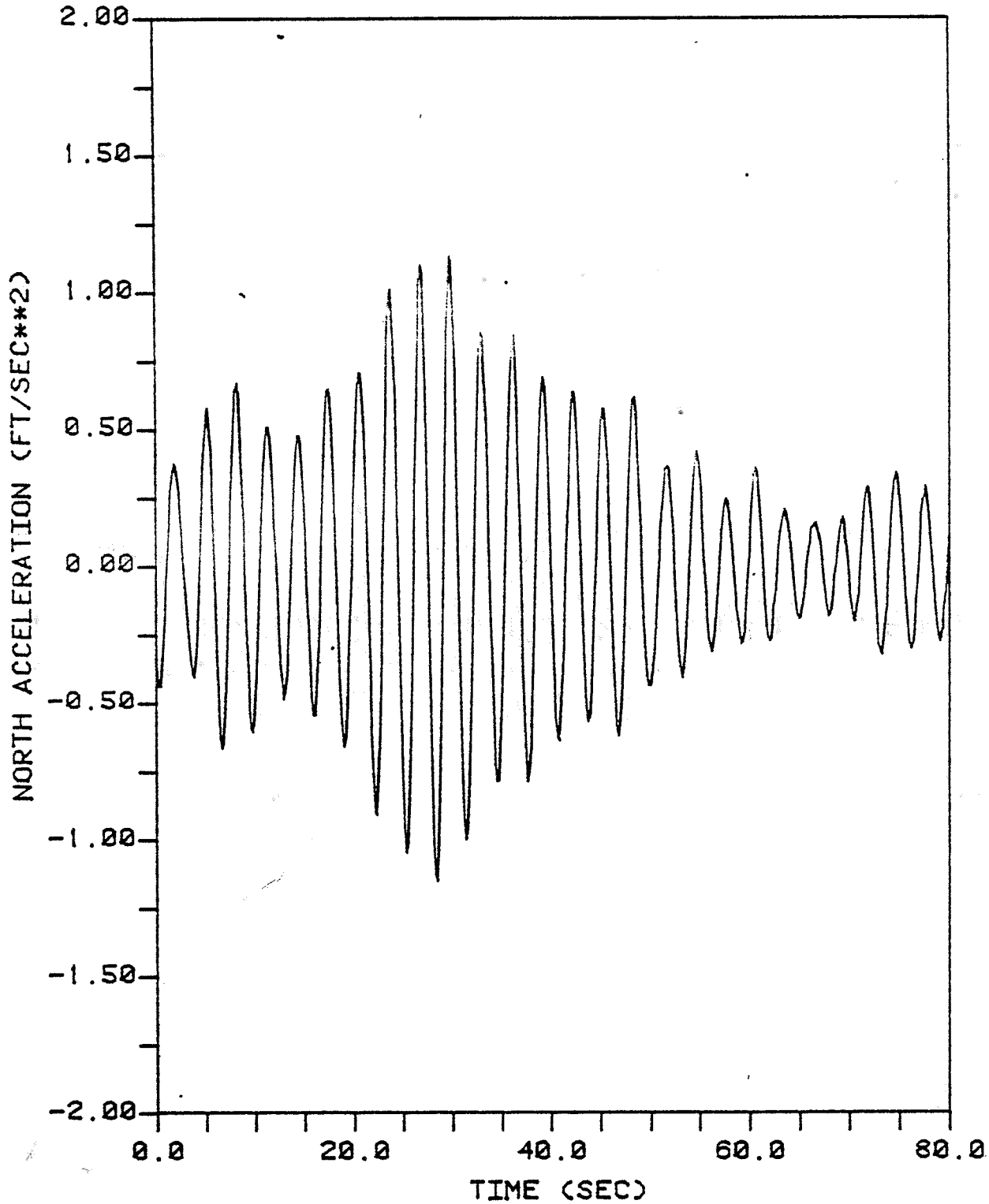

FIG 8.3: REEL 3 NAW ACCELEROMETER TIME HISTORY

method capable of achieving higher resolution spectral estimates with less data than conventional methods [Briggs, 1981]. The application of MEM to the analysis of offshore platforms was initiated by Campbell [1980] for single-channel analysis and extended to two-channels by Briggs [1981]. The MEM programs used in this thesis were written by Brad Campbell, during his tenure as an MIT graduate student.

The first step in single-channel analysis is to compute an estimate of the autocorrelation function $R_{xx}(n)$ from the digitized time series. The program ACORP, which employs an overlap and save FFT algorithm [Oppenheim and Schaffer, 1975], was used to compute a biased zero-mean autocorrelation function. An autocorrelation is a measure of the linear dependence between two points, in the same time history, a time difference n apart. The value of the autocorrelation at zero lag (n=0) is the mean square strength of the signal. In this analysis, a maximum lag of 80 seconds (512 points) was selected which corresponds to a frequency resolution of .0125 Hz. The variance associated with this resolution bandwidth depends on the number of data segments used in the estimate of the autocorrelation function. Specifically, the variance decreases with the inverse of the number of segments averaged. Achieving an acceptable variance for a desired resolution often requires long data lengths. Fortunately, in this analysis the data records are long enough to achieve an acceptable variance.

A summary of the parameters used in ACORP are shown in

Table 8.3. Figures 8.4-8.6 contain sample sea surface and acceleration response autocorrelations from reel 3. The acceleration autocorrelations are representative of a narrow band Gaussian sine wave process, which is characteristic of a lightly damped single degree of freedom system.

The next step in the analysis is the computation of MEM spectral estimates using the autocorrelations as input. To use MEM effectively requires practice because the shape of the computed spectral estimate depends on the number of lags selected. Specifically, the selection of too few lags may yield an estimate with less detail than optimum, while too many lags may introduce artificial features, such as spurious peaks, into the spectrum. For the analyst, there are four different criteria available within the MEM computer programs which aid in the selection of the number of lags to use. Of the four criteria, Akaike's FPE criteria [Akaike, 1970] is used most frequently as a general guide to the optimum number of lags.

8.2.1 Response Spectral Estimates

A response spectrum of a dynamically responding structure contains spectral peaks associated with each excited vibration mode. In this thesis, MEM single-channel spectral analysis was used to compute response spectral estimates for the AMOCO caisson. Then, the natural frequencies and damping ratios associated with the fundamental bending modes were estimated.

Within the MEM programs, natural frequencies are estimated using a maximum response estimator, while damping ratio

TABLE 8.3

AUTOCORRELATION PARAMETERS FOR EACH REEL

REEL NO.	NO. OF 512 PT. SEGMENTS	TOTAL NO. OF POINTS	TOTAL RECORD LENGTH (min)
1	60	30,720	80.0
2	58	29,696	77.33
3	58	29,696	77.33
4	58	29,696	77.33
5	49	25,088	65.33
6	33	16,896	44.0

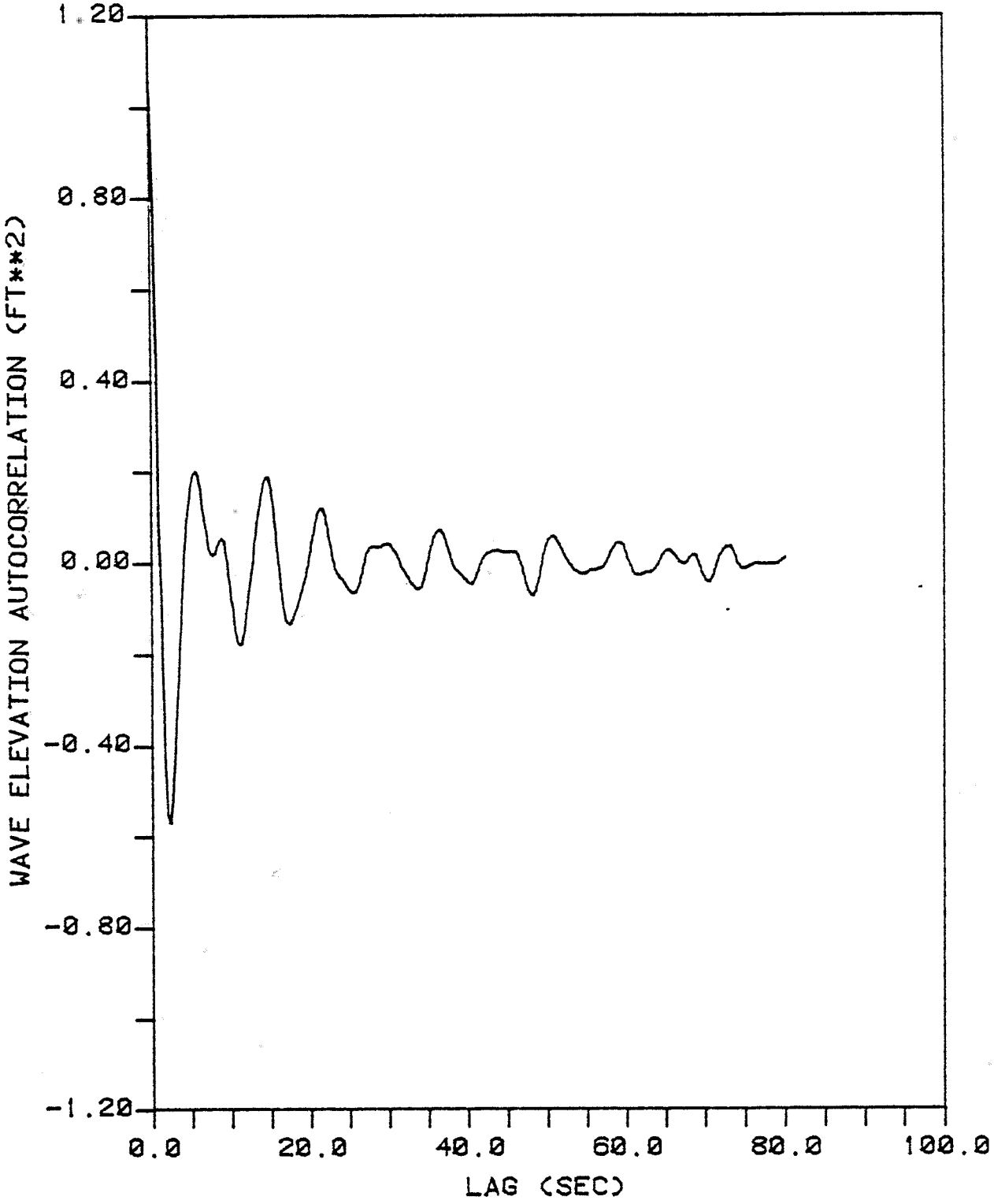

FIG 8.4: REEL 3 WAVE ELEVATION AUTOCORRELATION

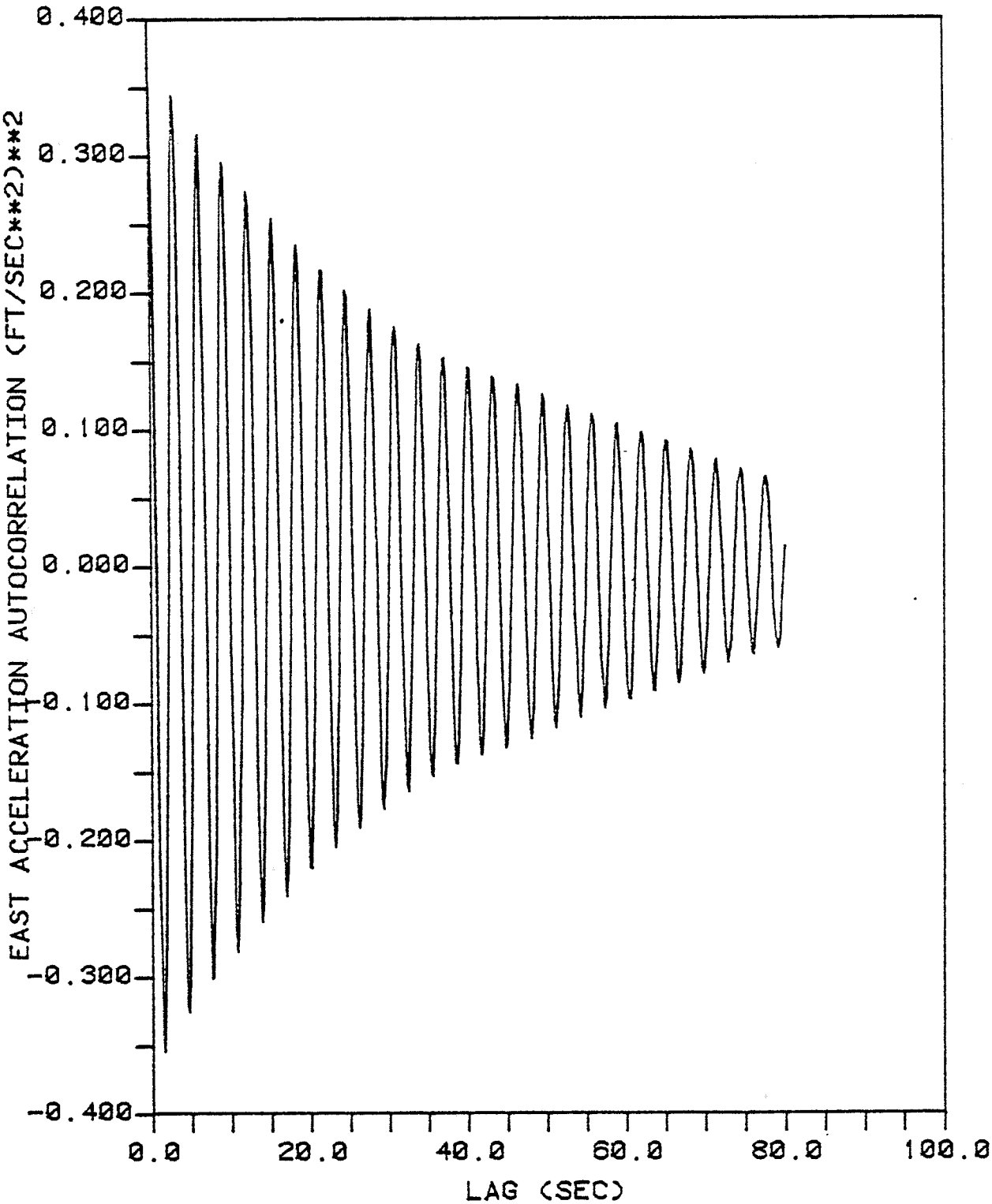

FIG 8.5: REEL 3 EAW ACCELEROMETER AUTOCORRELATION

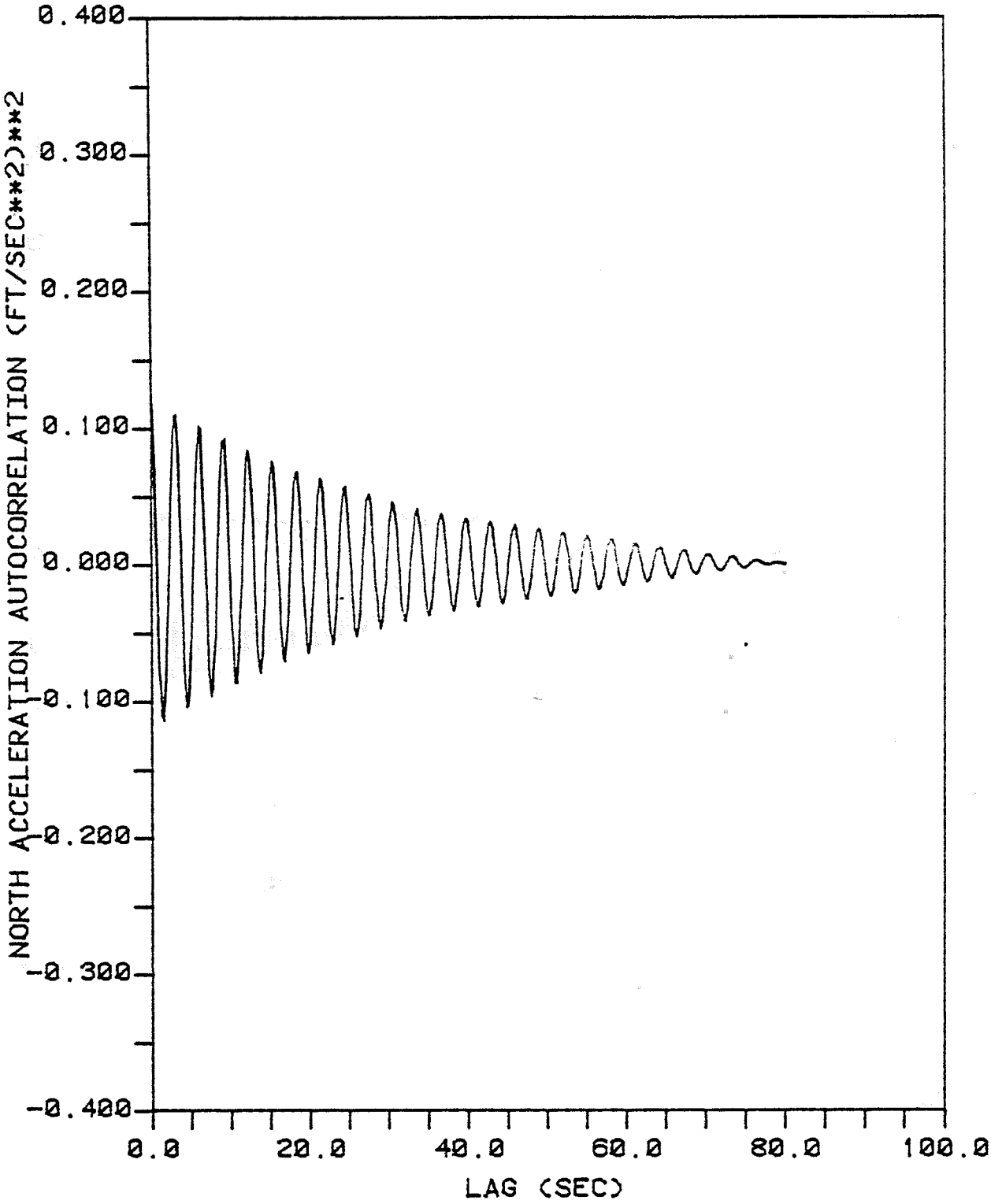

FIG 8.6: REEL 3 NAW ACCELEROMETER AUTOCORRELATION

estimates are half-power bandwidth estimates [Campbell, 1980]. The variances of these estimates are also computed, enabling the analyst to specify confidence limits for an estimate. Since both estimates and variances change with lag number, modal response characteristics cannot be conclusively inferred from a single response spectrum. Adequate identification requires knowledge of the variation of these estimates as a function of lag number. The computer program MEMAM was written for this purpose, as it computes estimates and variances of both natural frequency (f_n) and damping ratio (ξ_n) up to 100 lags. Above 100 lags, the program MEMNV (NV = No Variance calculation is performed) can be used to compute estimates of f_n and ξ_n. Plots of f_n and ξ_n versus lag number are then produced from which accurate estimates of f_n and ξ_n can be made. This procedure will be demonstrated for reel 3 data in Section 8.3.1.

Natural frequency and damping ratio estimates associated with a specific lag number are shown in Table 8.4. Also included in this table are the optimum number of lags, based on the Akaike's FPE criteria. MEM spectral estimates, using 101 lags, associated with the EAW and NAW accelerometers, as recorded on reel 3 are shown in Figures 8.7 and 8.8. From these plots it is obvious that the AMOCO caisson responds significantly in only its fundamental bending modes and that the natural frequencies of these modes are almost identical. In Section 8.3.1, a method is presented to isolate the orientation of these modes.

TABLE 8.4

NATURAL FREQUENCY AND DAMPING RATIO ESTIMATES ALONG EAST AND NORTH AXES

CHANNEL	OPTIMUM LAG	LAG USED	f_1 (Hz)	ξ_1 (%)
1 - EAP	255	255	.325	1.05
1 - NAP	256	256	.328	1.03
2 - NAH	276	101	.326	1.60
2 - NAP	249	101	.326	1.61
2 - NAW	298	101	.326	1.54
2 - NAB	251	101	.326	1.64
3 - EAW	300	101	.324	1.35
3 - NAW	265	101	.327	1.82
4 - EAW	229	101	.323	1.01
4 - NAW	260	101	.325	.83
4 - EAT	244	101	.323	.99
5 - EAW	295	295	.323	1.50
5 - NAW	278	278	.327	1.87
6 - EAW	300	101	.324	1.11
6 - NAW	241	101	.326	1.58

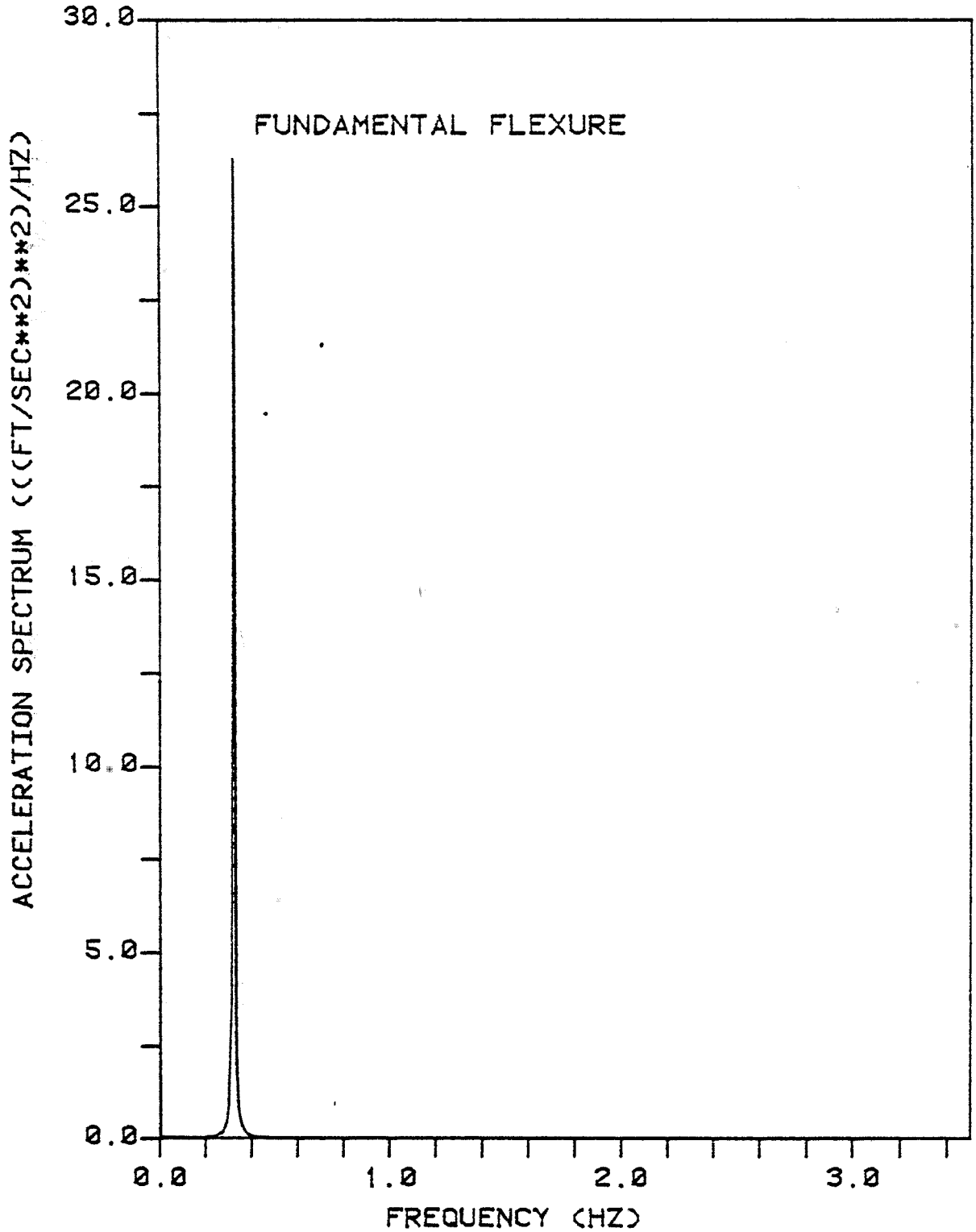

FIG 8.7: REEL 3 EAW ACCELEROMETER MEM SPECTRUM, 101 LAGS

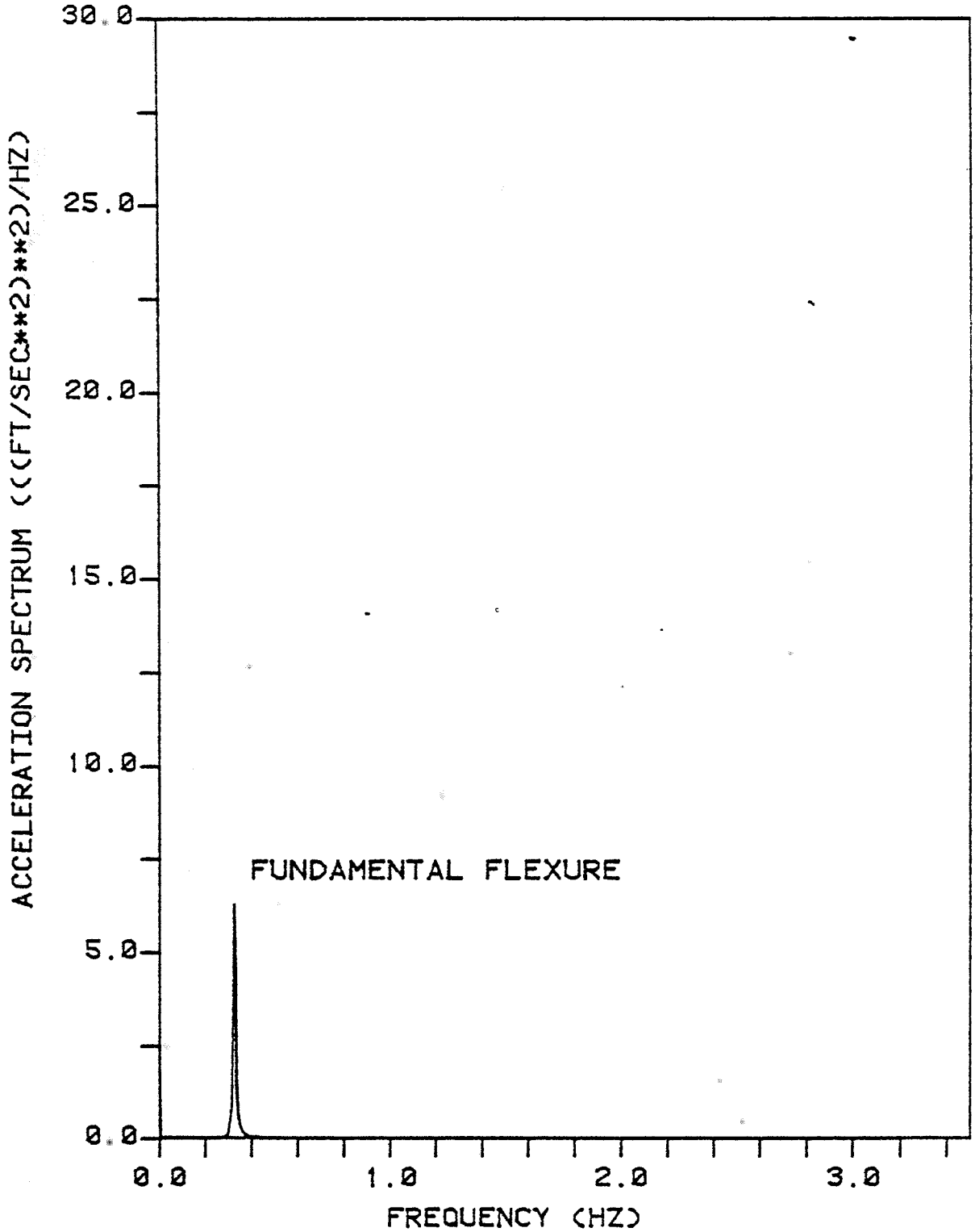

FIG 8.8: REEL 3 NAW ACCELEROMETER MEM SPECTRUM, 101 LAGS

8.2.2 Wave Spectral Estimates

Wave spectra were also obtained using the MEM programs. Useful wave data was recorded on four of the six reels and the resulting spectra are interesting. In general, wave spectra are only stationary over a time period in which the sea conditions stay relatively constant. On the days the wave data was recorded the weather was variable and the spectra are different. The reel 3 wave spectrum (Figure 8.9) has two dominant peaks indicating a swell component overlying wind-driven seas. The small peak at .32 Hz is the result of anchoring the staff to a moving platform. Both platform motions introduced at the anchor point on the wellhead deck and radiated waves produced due to the platform's vibration contribute to this peak. The reel 4 wave spectrum, shown in Figure 8.10, is typical of theoretical single-peaked spectra. Later in the day, however, the wind increased in strength and shifted directions, creating a significant number of high frequency waves as can be seen in Figures 8.11 and 8.12. An approximate value of significant wave height (H_s) was derived from the mean square of the wave record $R_{\eta\eta}(0)$ using the relation, $H_s=4(R_{\eta\eta}(0))^{1/2}$, which assumes the wave spectrum is a narrow band process [Conner and Sunder, 1980]. The peak periods and significant wave heights derived from these spectra are contained in Table 8.6.

8.2.3 Wind Spectral Estimates

Anemometer voltage outputs were recorded on reels 3, 5, and 6. Wind speed estimates were derived from this informa-

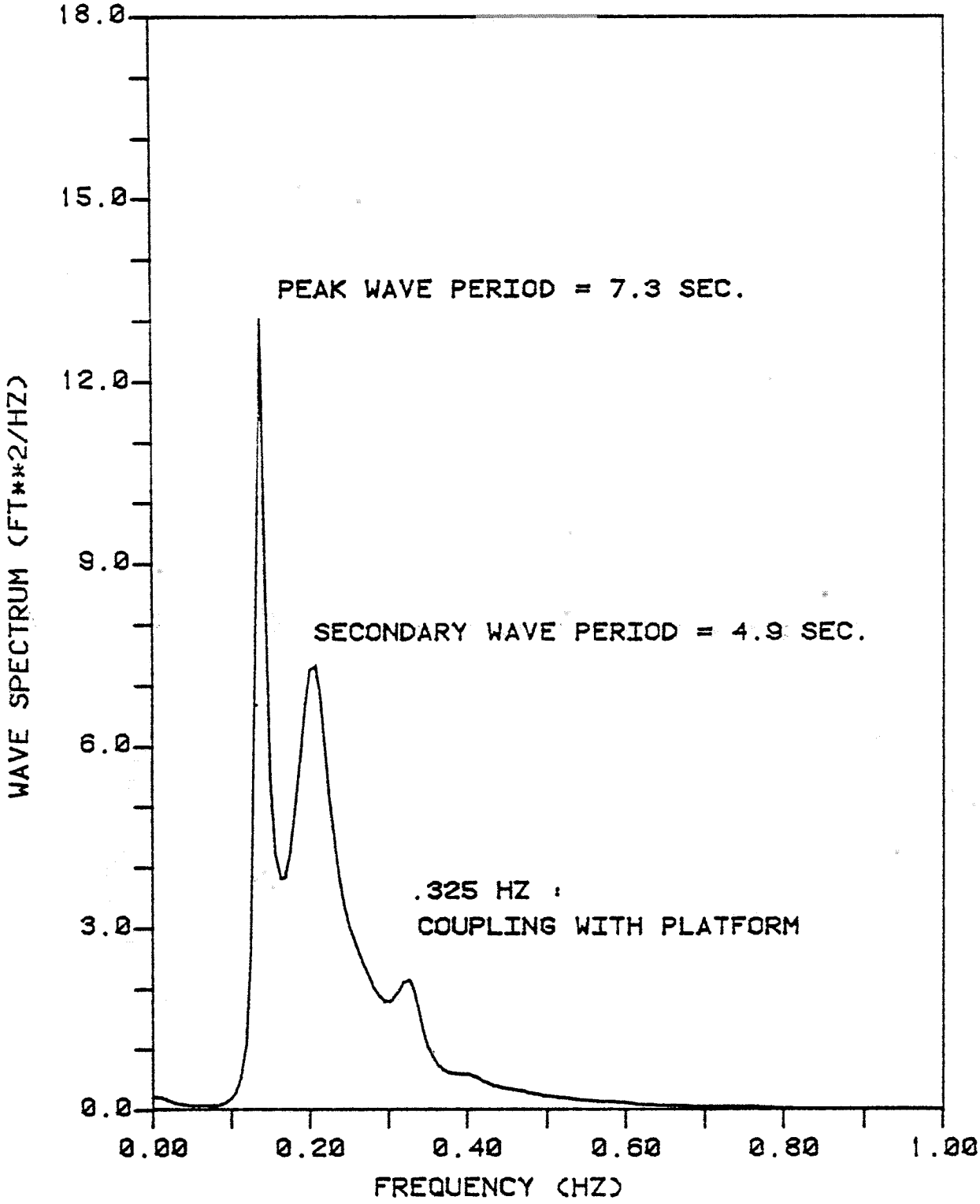

FIG 8.9: REEL 3 MEM WAVE SPECTRUM
101 LAG, 3-25-80: 1130-1315

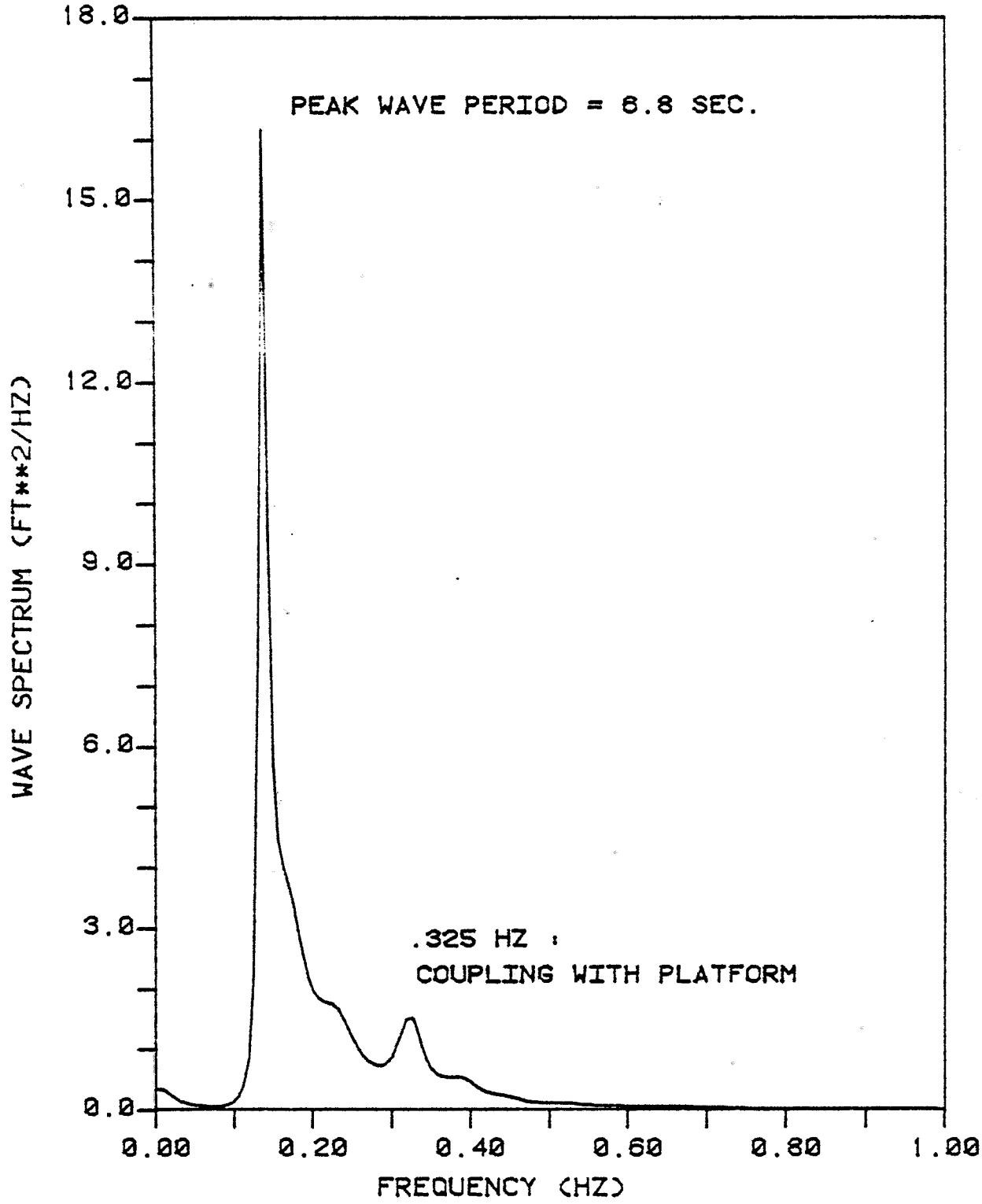

FIG 8.10: REEL 4 MEM WAVE SPECTRUM
101 LAG 3-28-80: 1050-1210

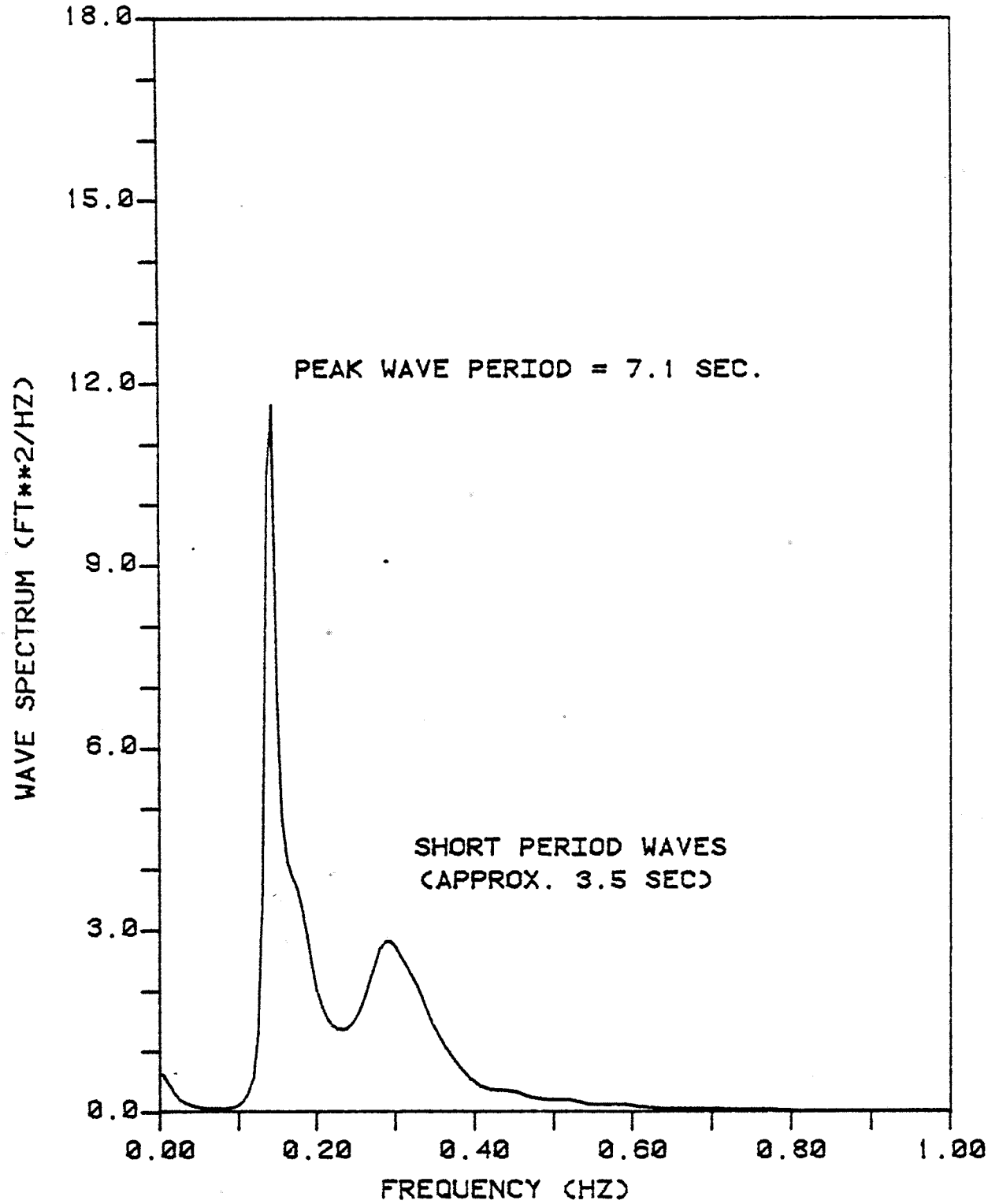

FIG 8.11: REEL 5 MEM WAVE SPECTRUM
101 LAG 3-28-80: 1450-1615

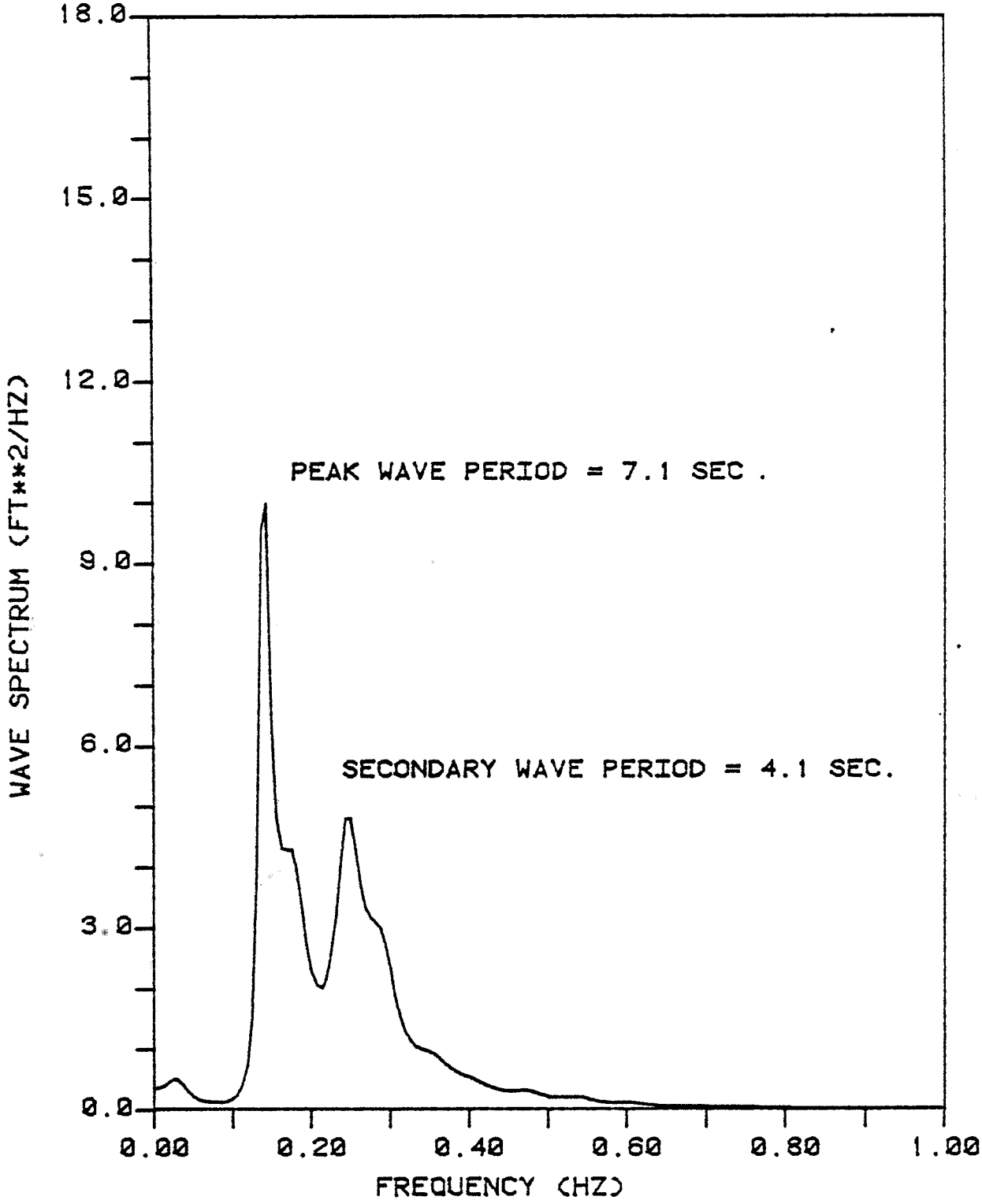

FIG 8.12: REEL 6 MEM WAVE SPECTRUM
101 LAG 3-28-80: 1630-1715

tion using the anemometer frequency to wind speed calibration factor, u=1.41f + 1, for u in knots and f in Hz. The frequency content of the anemometer voltage signal was obtained using the Gen-Rad supplied conventional real-time spectral analysis program TSLAP. The frequency axis of the spectral estimate was then scaled to correspond to wind speed in knots. The result is a wind speed intensity "spectrum" as shown in Figure 8.13 for 20 minutes of reel 3 data. A similar analysis was performed on the other two reels and the approximate mean wind speeds are shown in Table 8.6.

8.3 Two-Channel Analysis - Biaxial Pair of Accelerometers

In this thesis, a primary goal of the two-channel analysis was to isolate the two fundamental bending modes of the AMOCO caisson from the response time histories of a biaxial pair of accelerometers. As observed in Section 8.2.1, the analysis of a single channel of response yields no information about the modal orientation since both modes have virtually the same natural frequency and a single accelerometer measures components of both modes along its sensitive axis. However, joint analysis of the time histories of a biaxial pair of accelerometers can yield valuable insight into the response characteristics of the single pile platform. If the modes can be isolated, single-channel techniques can be used to estimate modal natural frequencies, damping ratios, and mean square response magnitudes.

8.3.1 Modal Orientation Identification

The AMOCO caisson responds predominantly in its two

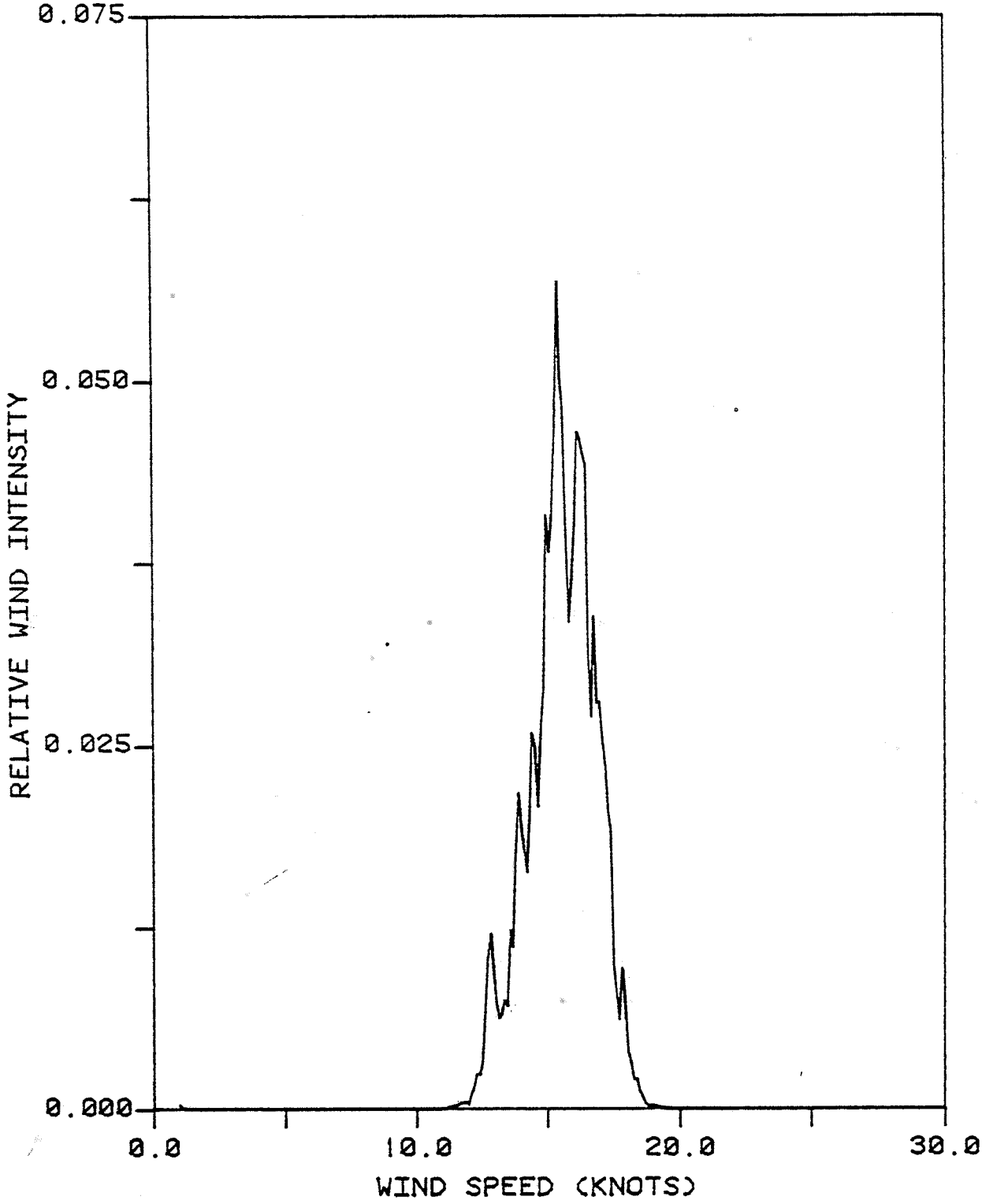

FIG 8.13: REEL 3 WIND SPEED INTENSITY "SPECTRUM"

fundamental bending modes. These modes are orthogonal to one another and have almost identical natural frequencies. The frequencies differ because of platform asymmetries and day-to-day changes in the soil behavior at the site. Since the frequencies are different, the modal orientation, measured relative to a fixed coordinate system, at any particular time is uniquely defined. In addition, through modal analysis, these two modes are independent of one another and depend strictly on the mass and stiffness properties of the system. Therefore, directionality in the seas influences the modal orientation only indirectly, through changes in the soil properties which occur under cyclic loading. In this section, the modal directions are isolated by analyzing the response time histories of a biaxial pair of accelerometers.

Accelerometers in a biaxial pair measure platform responses along two axes. For the Lollipop, the placement of the accelerometers was chosen strictly for day-to-day reproducibility, by lining one up with platform east, the other with platform north. Therefore, unless the modes are along the East-North (E-N) axes, the E-N accelerometers record components of both modes. This introduces coupling between the E-N accelerometers. The auto- and cross-correlation functions of the E-N biaxial pair contain these response characteristics.

The detection scheme developed to isolate the modal orientation uses the correlation functions in the same manner as knowledge of the normal and shear stresses on a 2-D beam section is used to isolate the principal stress axes. In the

beam, the principal axes define the surface on which only normal stress acts (shear stress equals zero). The angle at which this occurs is obtained using a Mohr's circle analysis. Using the same algorithm, the characteristics of response versus orientation in the horizontal plane can be investigated by rotating the E-N correlation functions. Specifically, for the AMOCO caisson, a new set of correlation functions, corresponding to an imaginary biaxial accelerometer pair at angle α (see Figure 8.14), was obtained using

$$\begin{bmatrix} R_{11}(n;\alpha) & R_{12}(n;\alpha) \\ R_{21}(n;\alpha) & R_{22}(n;\alpha) \end{bmatrix} = \begin{bmatrix} \cos\alpha & \sin\alpha \\ -\sin\alpha & \cos\alpha \end{bmatrix} \begin{bmatrix} R_{ee}(n) & R_{en}(n) \\ R_{ne}(n) & R_{nn}(n) \end{bmatrix} \begin{bmatrix} \cos\alpha & -\sin\alpha \\ \sin\alpha & \cos\alpha \end{bmatrix} \tag{8.1}$$

Equation 8.1 was simplified, recognizing $R_{en}(n)=R_{ne}(-n)$, to yield the four equations necessary to compute a rotated set of correlation functions.

$$R_{11}(n;\alpha) = R_{ee}(n)\cos^2\alpha+R_{nn}(n)\sin^2\alpha+(R_{en}(n)+R_{en}(-n))\cos\alpha\sin\alpha \tag{8.2}$$

$$R_{22}(n;\alpha) = R_{ee}(n)\sin^2\alpha+R_{nn}(n)\cos^2\alpha+(R_{en}(n)+R_{en}(-n))\cos\alpha\sin\alpha \tag{8.3}$$

$$R_{12}(n;\alpha) = R_{en}(n)\cos^2\alpha-R_{en}(-n)\sin^2\alpha+(R_{nn}(n)-R_{ee}(n))\cos\alpha\sin\alpha \tag{8.4}$$

$$R_{12}(-n;\alpha) = R_{en}(-n)\sin^2\alpha-R_{en}(n)\sin^2\alpha+(R_{nn}(n)-R_{ee}(n))\cos\alpha\sin\alpha \tag{8.5}$$

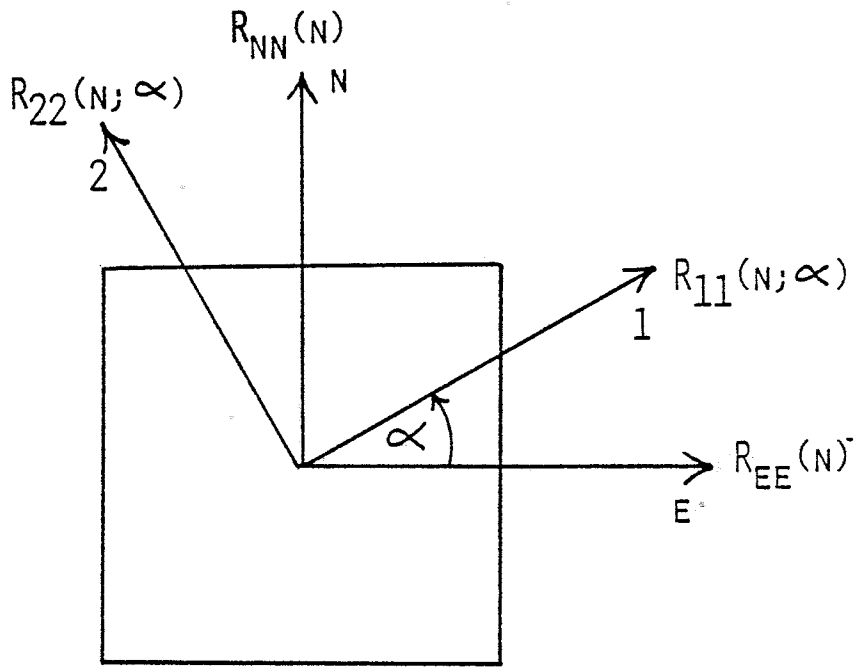

FIG. 8.14: DEFINITION SKETCH FOR ROTATED CORRELATION FUNCTIONS

where: $R_{11}(n;\alpha)$ = autocorrelation along 1-axis for angle α

$R_{22}(n;\alpha)$ = autocorrelation along 2-axis for angle α

$R_{12}(n;\alpha)$ = cross-correlation between the 1-2 axes for angle α

A modal orientation identification analysis was performed to isolate the modal directions associated with each reel of Lollipop data containing biaxial accelerometer time histories. The analysis scheme developed to make a positive identification of the unique modal orientation uses five sources of information in two phases. In the first phase, plots of natural frequency, damping ratio and mean square response estimates along the 1-2 axes as a function of α for $-45° < \alpha < 45°$, are produced. Since the modes have distinct natural frequencies, the angle associated with the maximum separation in natural frequencies should define the modal directions. Similarly in the true modal coordinates the damping values should be minimums. At other angles the reponse peaks will be broader due to the presence of two components. The natural frequency estimate associated with each autorcorrelation file was computed by counting autocorrelation cycles and dividing by the time. The damping ratio estimate was obtained using log decrements. For all but one case, these estimates were inconclusive and often contradictory. The best results, obtained from reel 3, are shown in Figures 8.15 and 8.16. In both figures, the solid line represents the orientation of the 1-axis, while the 2-axis is the dashed line, plotted versus α. At 0 degrees, the ordinates represent the

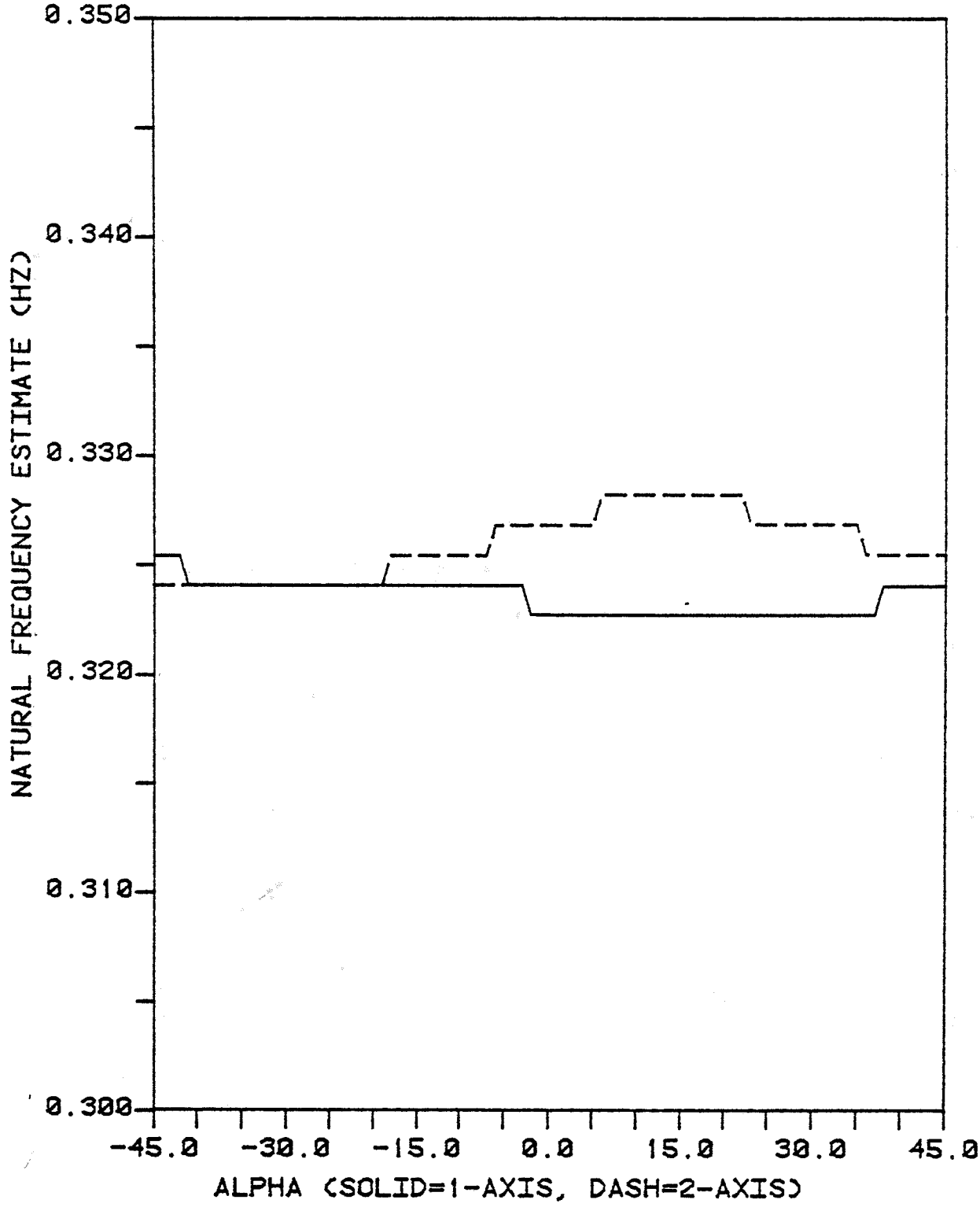

FIG 8.15: REEL 3 NATURAL FREQUENCY ESTIMATE VS. ORIENTATION

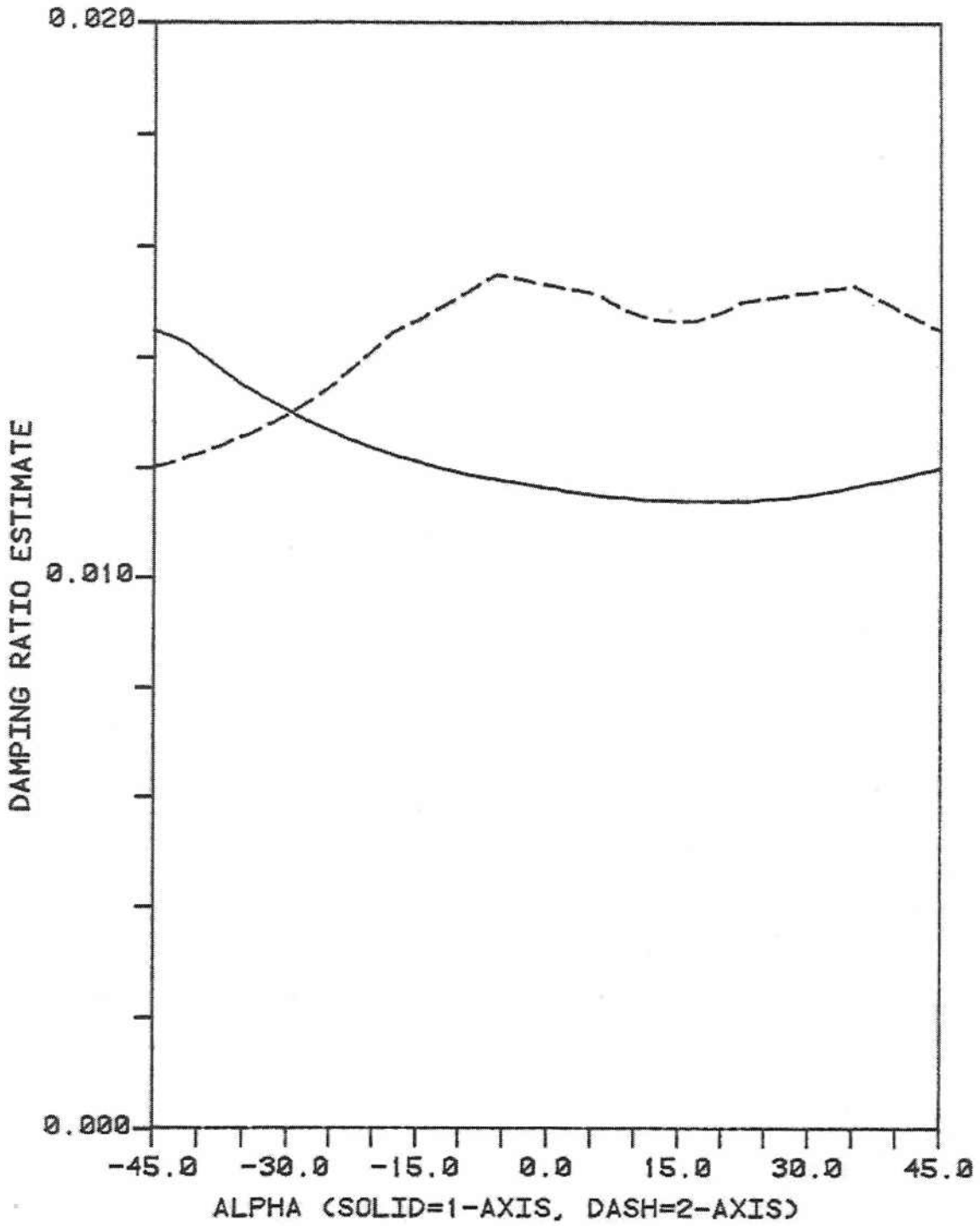

FIG 8.16: REEL 3 DAMPING RATIO ESTIMATE VERSUS ORIENTATION

estimates in the E-N axes.

A plot of mean square Lollipop response along the 1-2 axes as a function of α indicates directionality in the seas. The directionality of the forcing only influences the modal orientation through modification of the soil properties under cyclic pile loading. It is hypothesized, however, that if the seas remain constant in direction over a sufficient period of time, the soil properties will adjust to the motion and the principal modal direction will tend to line up with the dominant forcing direction. The plot of mean square response versus angle is shown in Figure 8.17 for reel 3. The dominant forcing direction is 13 degrees North of East which agrees with the observed sea conditions. In addition, it is anticipated that the orientation of the dominant mode will correspond closely with this direction, if sufficient time has passed for the soils to adjust. To test this hypothesis, a second phase of analysis was performed.

In the second phase, the correlation between rotated biaxial pairs was computed as a function of α to find the angle at which the correlation is a minimum. This angle should correspond to the modal axes since, in theory, modes are independent and responses in one modal direction do not affect motions in the other. The single pile platform is an ideal structure to test this hypothesis because of its simple geometry and near equality of modal natural frequencies. In the offshore community, the correlation between modes is an important issue in fatigue analysis. If the modes are independent,

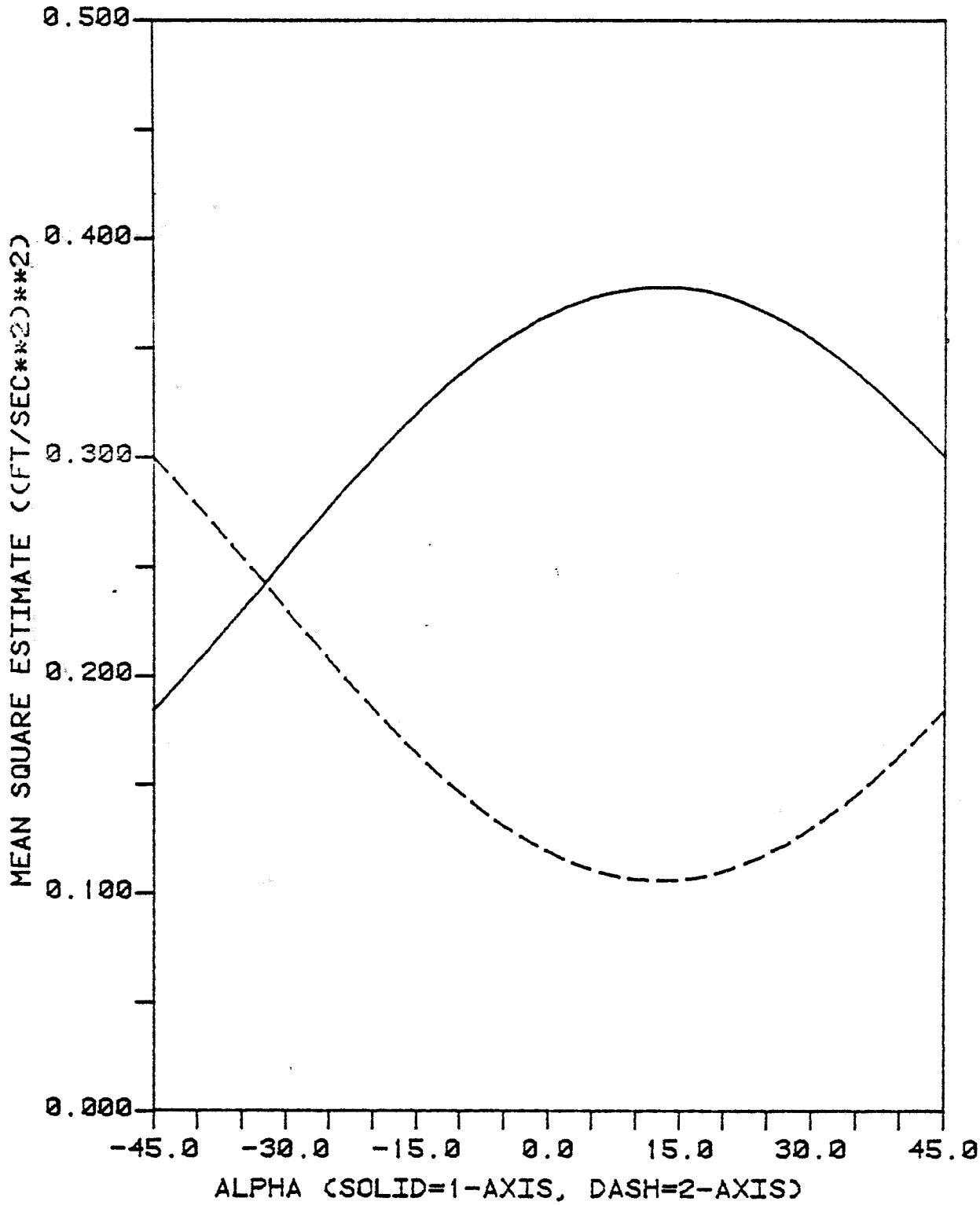

FIG 8.17: REEL 3 M. S. ACCELERATION ESTIMATE VS. ORIENTATION

the stress contributions caused by motions in both modes can be simply summed together.

The correlation between biaxial accelerometers was investigated in both frequency and time domains. In the frequency domain, the measure of correlation is the coherence function (sometimes called the coherency squared; Bendat and Preisol, 1980) which is defined as

$$\gamma_{xy}^2(f) = \frac{|G_{xy}(f)|^2}{G_{xx}(f)G_{yy}(f)}, \quad 0 \leq \gamma_{xy}^2(f) \leq 1 \tag{8.6}$$

where $\gamma_{xy}^2(f)$ = coherence function between time histories x and y at frequency f.

$G_{xy}(f)$ = cross-spectrum between x and y processes

$G_{xx}(f)$ = autospectrum of x process

$G_{yy}(f)$ = autospectrum of y process.

A coherence of 1 at a frequency indicates perfect correlation while a value of 0 implies the time histories are uncorrelated (incoherent) at that frequency. The computer program BTSPEC, a two-channel Blackman-Tukey spectral analysis program, was used to compute the coherence between biaxial accelerometer pairs. By plotting the coherence at the frequency of the fundamental modes, f=.325 Hz, as a function of α, the angle associated with the minimum coherence is easily obtained. The plot for reel 3 is shown in Figure 8.18. The minimum coherence is .008 at an angle of 13 degrees. This implies that at this angle, the accelerometer responses in the fundamental modes are essentially uncorrelated so this must be the modal

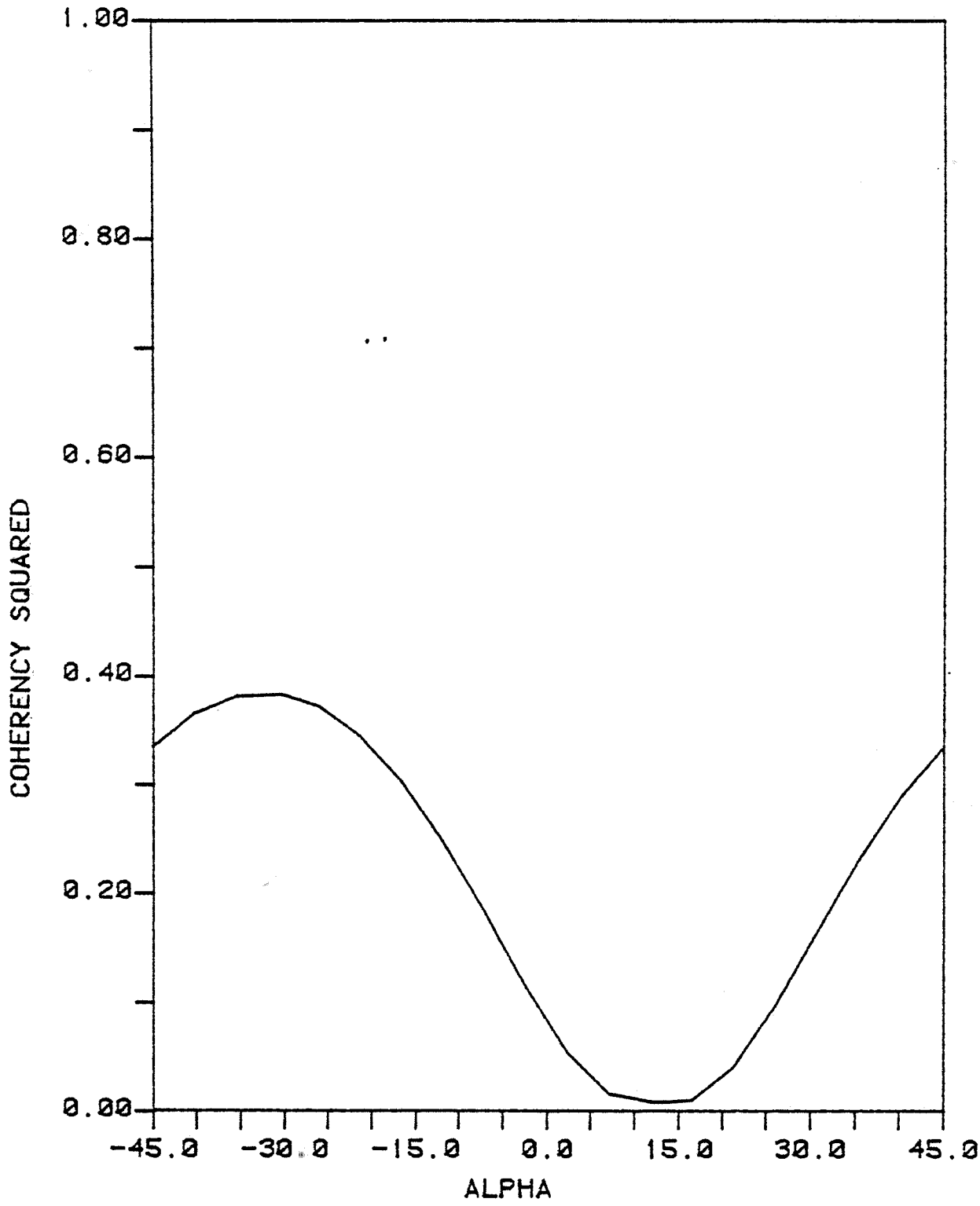

FIG 8.18: REEL 3 COHERENCE ESTIMATE AT 0.325 HZ VS. ALPHA

orientation. At angles other than 13 degrees, coupling exists between the biaxial accelerometers. The maximum coherence is .384 at -32 degrees.

To verify this result in the time domain, plots of the correlation coefficient $\rho_{12}(n;\alpha)$

$$\rho_{12}(n;\alpha) = \frac{R_{12}(n;\alpha)}{(R_{11}(n;\alpha) + R_{22}(n;\alpha))^{1/2}} \quad , 0 \leq \rho_{12}(n;\alpha) \leq 1 \tag{8.7}$$

were produced at the angles of α associated with the maximum and minimum coherences, and at $\alpha=0$. The results for reel 3 are shown in Figures 8.19-8.21. The magnitude of the correlation coefficient is substantially reduced along the modal axes defined by $\alpha=13$ degrees. For reel 3, the modal orientation lines up exactly with the dominant forcing and the correlation along the modal axes is essentially zero.

The same analysis was performed for the other four reels which contain biaxial accelerometer time histories. The results are shown in Table 8.5. In all cases, the estimated principal modal axis is within 8 degrees of the estimated dominant forcing direction. In addition, the levels of coherence associated with the modal orientations are small (less than 5%), as they should be, for reels 1, 3, and 4. However, for reels 5 and 6, the coherence of the modal oreintations are 18% and 38%, respectively, of the maximum coherence.

A hypothesis has been developed to explain this high level of coherence for reels 5 and 6. Reels 4, 5, and 6 were recorded on the same day; reel 4 in the morning, 5 and 6 in

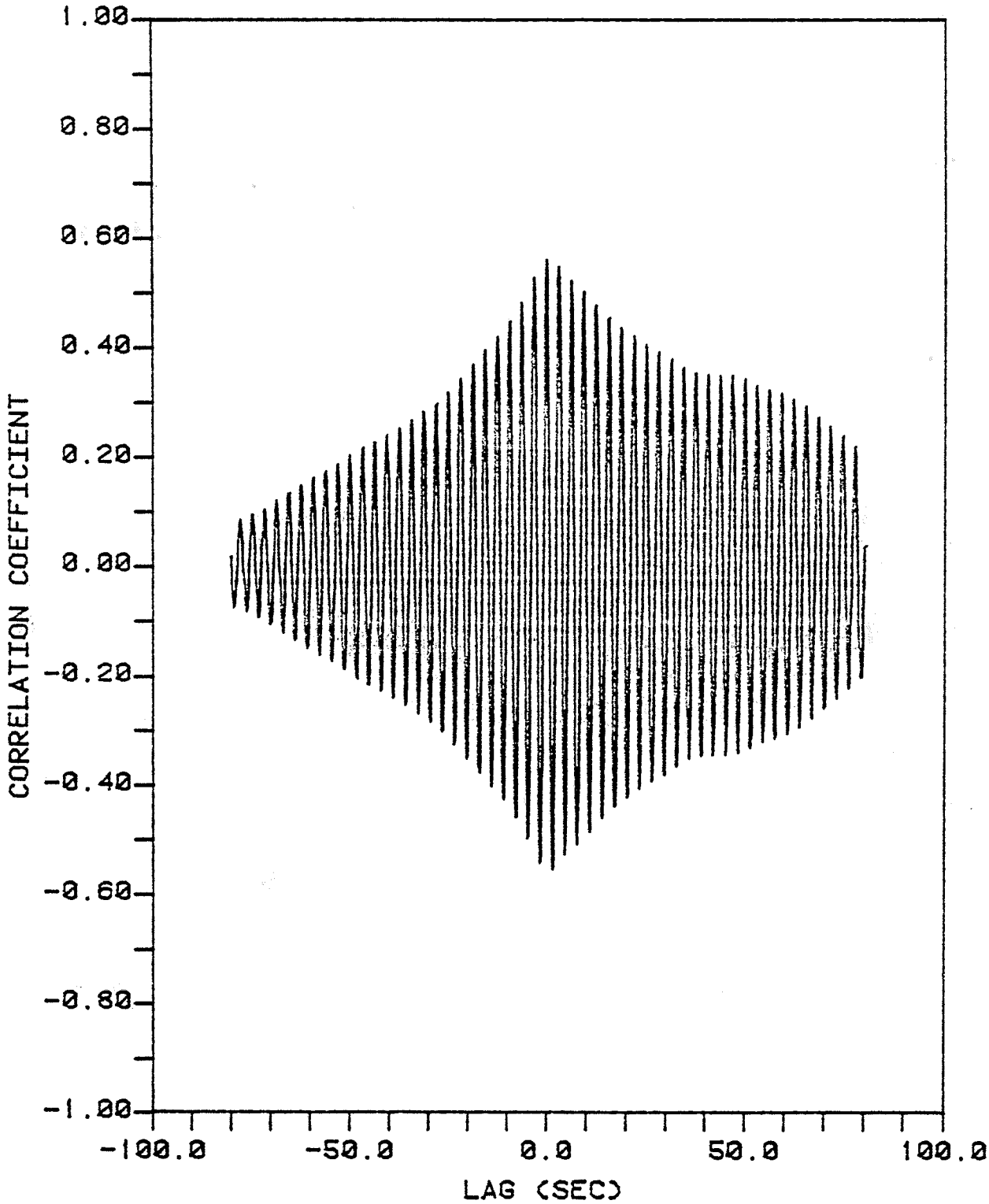

FIG 8.19: REEL 3 MAXIMUM CORRELATION COEFF.: ALPHA = -32 DEG.

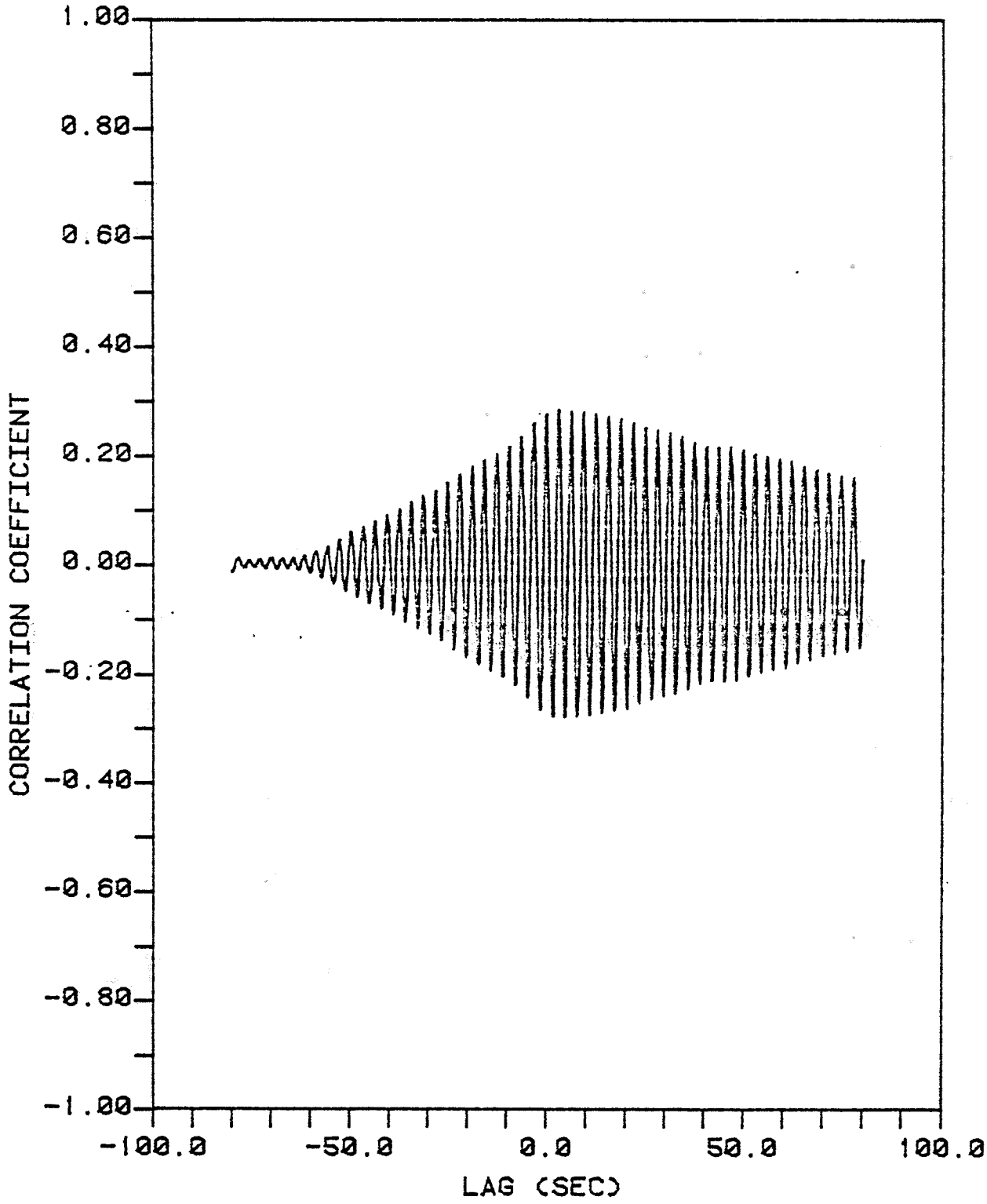

FIG 8.20: REEL 3 CORRELATION COEFF.
E-N AXES: ALPHA = 0 DEG.

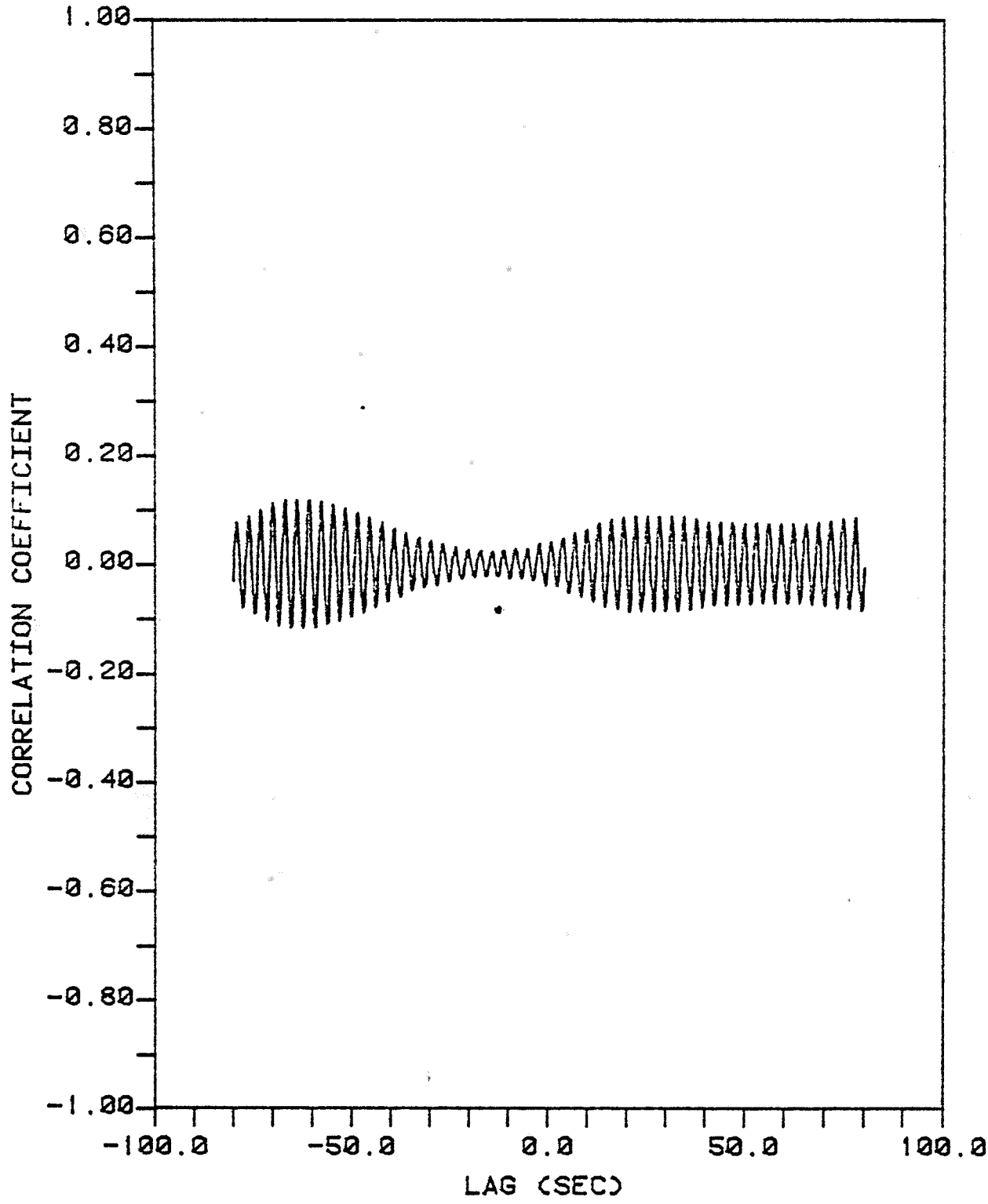

FIG 8.21: REEL 3 CORRELATION COEFF.
MODAL AXES: ALPHA= +32 DEG

TABLE 8.5

MODAL ORIENTATION RESULTS

REEL NO.	α_F (Degrees)	α_{mode} (Degrees)	COHERENCY SQUARED @ α_{mode}	α_{max} (Degrees)	COHERENCY SQUARED @ α_{max}
1	-32°	-25°	.0006	+20°	.125
3	+13°	+13°	.008	-32°	.384
4	+32°	+35°	.009	-10°	.194
5	-13°	- 7°	.030	+38°	.165
6	-18°	-15°	.076	+30°	.202

α_F - Angle associated with dominant forcing direction.

α_{mode} - Angle associated with the modal directions, (minimum coherence)

α_{max} - Angle associated with the maximum coherence

the afternoon. The weather on this day was in a state of transition and the seas changed from East-North-East (ENE) in the morning to East-South-East (ESE) in the afternoon. From Table 8.5, the estimated dominant forcing direction changes from 32 degrees North of East in reel 4 to 18 degrees South of East in reel 6. At the same time, the modal orientation changes from 35 degrees to -15 degrees. Based on this information, it seems the change in modal orientation lags the dominant forcing direction by at most a few hours. This behavior would explain the high coherence between the modal axes in reels 5 and 6 as due to a nonstationary process. If the modal orientation changed during the recording of a reel, the coherence would not disappear between the modal directions. In any case, these results indicate that changes in the directionality of the wave forcing may indeed alter the modal orientation. However, more research is necessary to conclusively verify this result.

Once the modal orientation was isolated, single-channel MEM spectral analysis was used to estimate the natural frequency and damping ratios associated with the fundamental bending modes of the AMOCO caisson. To estimate reasonable values of damping ratio and natural frequency of a mode using MEM, knowledge of the sensitivity of these estimates as a function of lag is required. As discussed in Section 8.2.1., the programs MEMAM and MEMNV are used for this purpose. Here, plots of natural frequency and damping ratio estimates versus lag number are shown in Figures 8.22-8.25 for the modal axes of reel 3.

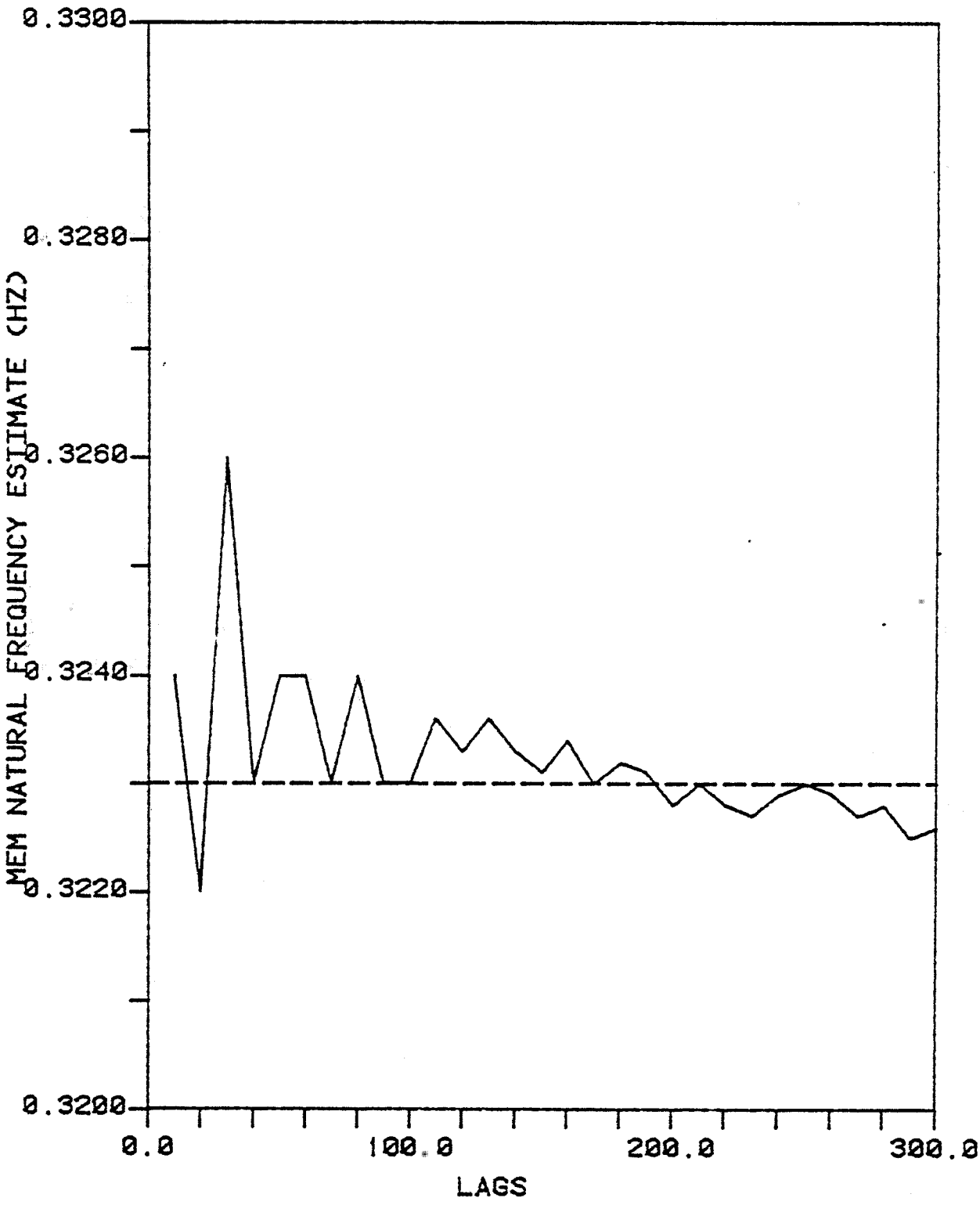

FIG 8.22: REEL 3 NATURAL FREQ. EST. FOR MODE 13 DEG. N. OF E.

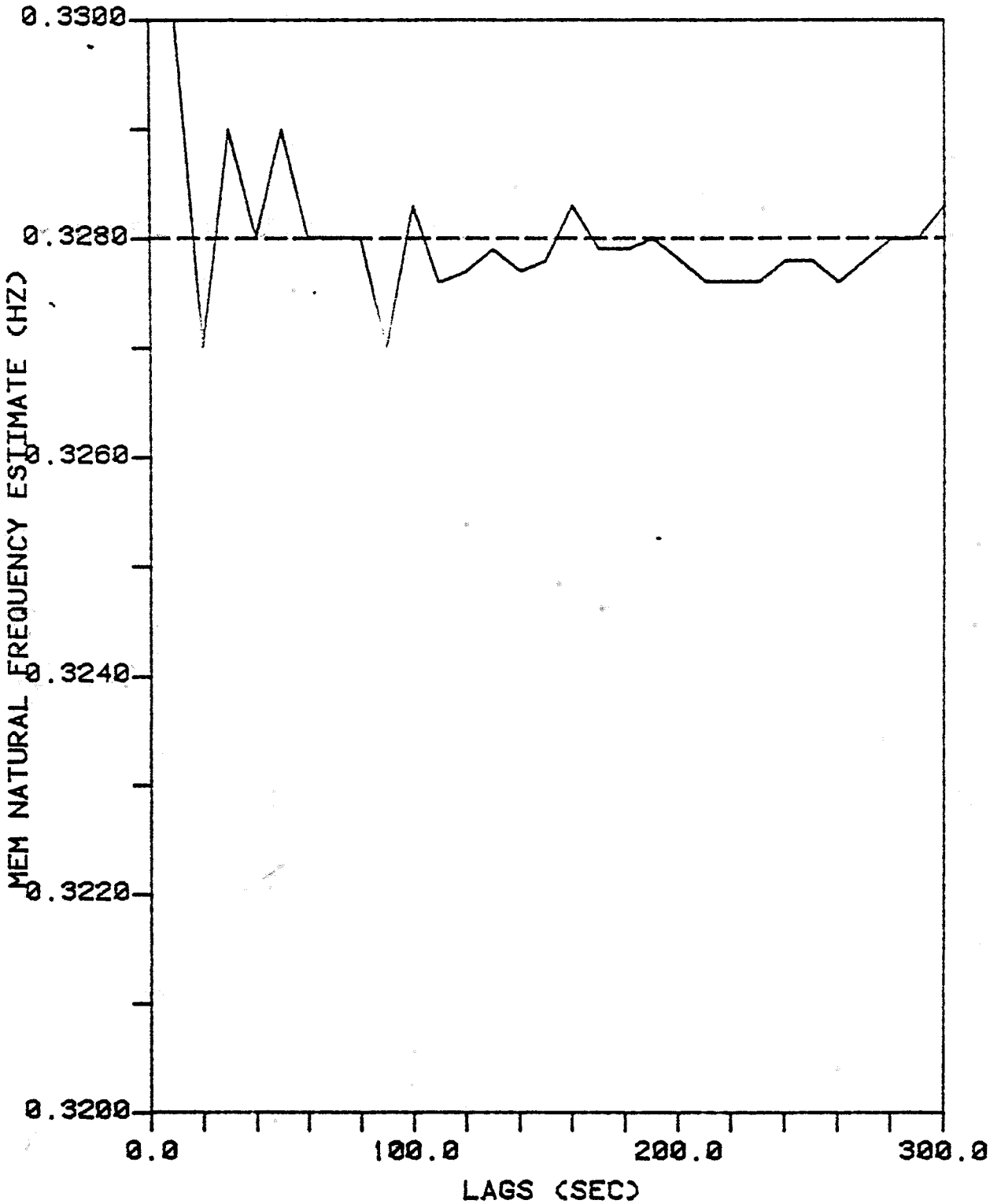

FIG 8.23: REEL 3 NATURAL FREQ. EST.
FOR MODE 32 DEG. S. OF E.

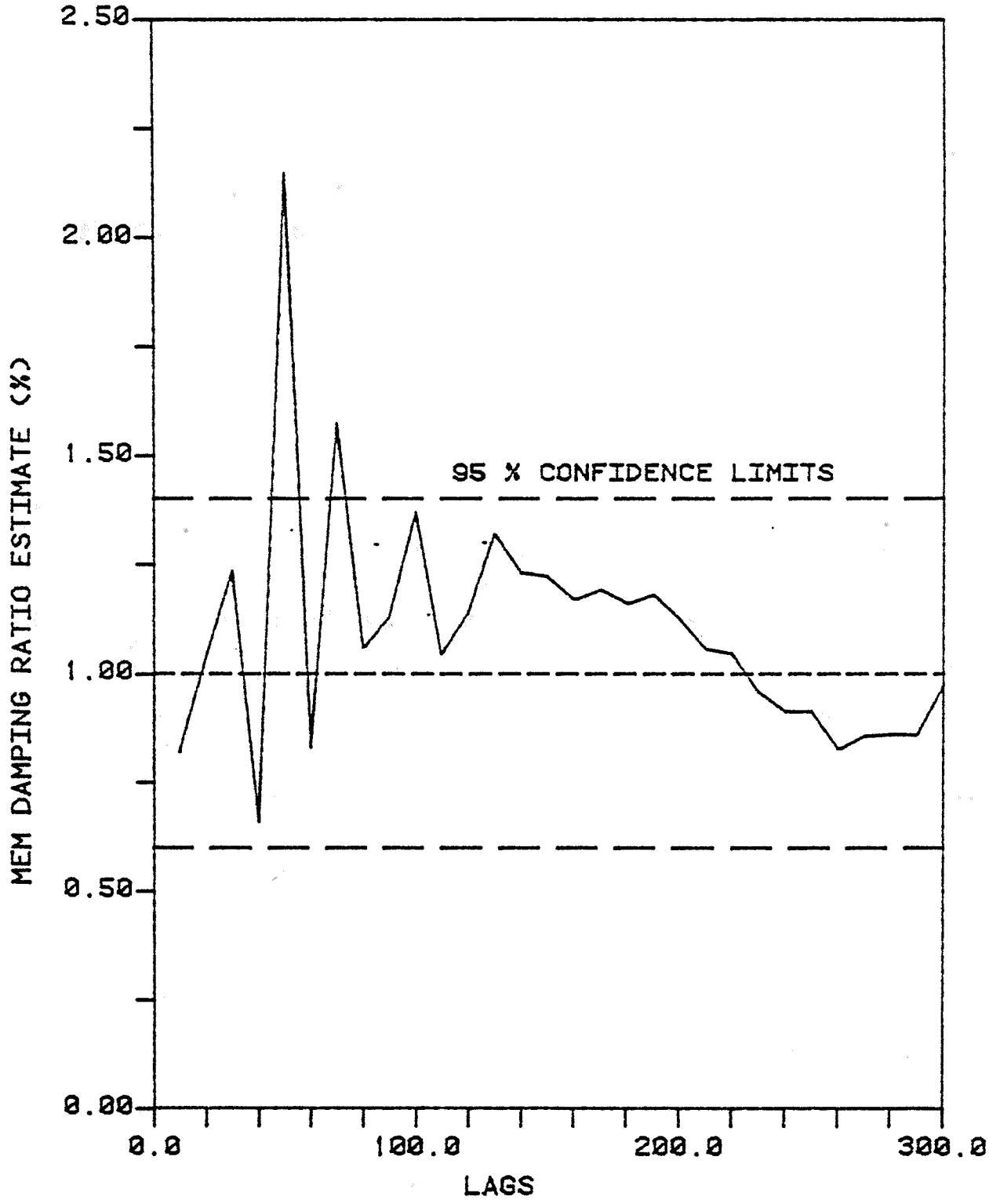

FIG 8.24: REEL 3 DAMPING RATIO EST. FOR MODE 13 DEG. N. OF E.

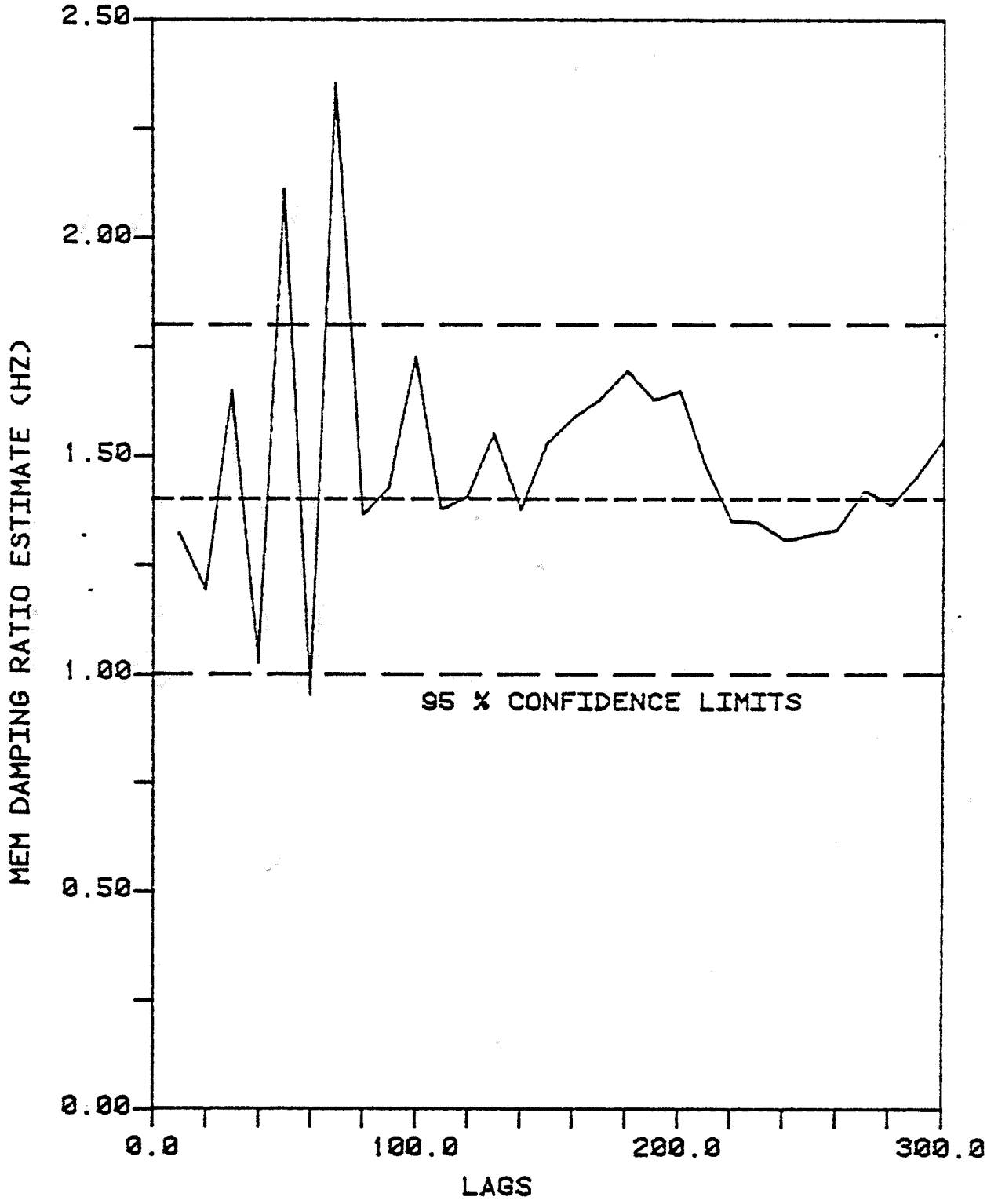

FIG 8.25: REEL 3 DAMPING RATIO EST. FOR MODE 32 DEG. S. OF E.

Superimposed on these plots are the approximate mean value and the associated 95% confidence bounds. Natural frequency estimates have small variance and are therefore fairly easy to estimate. The damping ratio estimate, however, is difficult to select and is based on the behavior of the estimator and the optimum number of lags. In general, the MEM estimates will oscillate with large amplitude initially and then settle down as the number of lags is increased. The values of damping ratio selected in Figures 8.24 and 8.25 were selected based on an approximate mean value for lags above 200. It is obvious from this procedure that the damping ratio estimates should have large confidence limits.

Similar analysis was performed for the other reels of data. The resulting estimates of modal natural frequency and damping ratio are contained in Table 8.6, which is in the next section. In this table, the damping ratio estimates associated with reel 5 are significantly larger than the other reels. The higher damping ratio estimates are due to a dynamic absorber, which was operating on the platform when reel 5 was recorded. The absorber consisted of a 600 pound bag of water, hung as a pendulum from the production deck, and tuned to oscillate at the frequency of the fundamental modes. The absorber was restrained to oscillate along the East-West axis. A detailed description of the estimation of the damping associated with the dynamic absorber is contained in a report by Lu and Vandiver to be presented at the 1982 Offshore Technology Conference.

8.3.2 Identification of Wave Spreading

A single pile platform, which responds significantly at only the frequency associated with the fundamental bending modes, acts as a transducer of the wave forcing. Specifically, in a directionally spread sea, the maximum mean square response should correspond in direction to the principal direction of the seas, if only wave forcing is present. In this section, the mean square response information associated with a biaxial pair of accelerometers is used to estimate the spreading in the seas.

As described in Section 5.2, wave spreading can be characterized in several ways. Here, the spreading function associated with the eccentricity of an ellipse as defined in Equation 5.13 will be used. To calculate an estimate of the eccentricity from a biaxial pair of accelerometer records measured on the AMOCO caisson requires the following steps:

1) Isolate the dominant forcing direction α_F as outlined in the previous section (see Figure 8.17 and Table 8.5) and record the values of mean square response along both axes.

2) Equate the maximum mean square value $R_{max}(0;\alpha_F)$ with the major axis of an ellipse and the minimum value $R_{min}(0;\alpha_F)$ with the minor axis.

3) Compute the eccentricity which is defined as

$$e = \frac{(a^2-b^2)^{1/2}}{a^2} = \frac{(R_{max}^2(0;\alpha_F) - R_{min}^2(0;\alpha_F))^{1/2}}{R_{max}(0;\alpha_F)} \qquad (8.8)$$

where a = major axis of an ellipse

b = minor axis of an ellipse

Estimates of the eccentricity were calculated for all biaxial accelerometer pairs and these results are shown in Table 8.6. In all cases, except for reel 3, the spreading in the seas is greater than cosine-squared spreading. A summary of the important observed and derived data obtained for the reels containing biaxial accelerometer time histories is contained in Table 8.6.

8.3.3 Platform Displacements

Real-time displacements of the AMOCO caisson can be obtained by judiciously double-integrating both acceleration time histories of a biaxial pair of accelerometers and plotting the resulting displacement records as ordered pairs. Knowledge of the displacement time history of a structure enables the analyst to directly calculate the dynamic component of stress within the pile as a function of time. The total displacement response of the Lollipop is much simpler than multi-pile structures since only two modes contribute significantly to the total response. However, even with only two modes, the displacement of the caisson is random and very different from the displacements calculated assuming unidirectional seas.

The computer program used in this thesis to successfully double integrate a time series, DUBINT, was written by Jen-y Jong, an MIT graduate student. The program uses the following sequence of operations on an input zero-mean digitized acceleration time history to obtain the displacement trace.

TABLE 8.6

SUMMARY OF WAVE, WIND AND RESPONSE DATA

	REEL #1	REEL #3	REEL #4	REEL #5	REEL #6
Date	3-24-80	3-25-80	3-28-80.	3-28-80	3-28-80
Time	1510-1630	1215-1335	1050-1210	1510-1615	1630-1715
Observed Wave Height (ft)	NW 1-3	ENE 5-8	ENE 2-4	ESE 3-5	ESE 3-5
Observed Wind Speed (knots)	NW @ 20	ENE @ 30	ENE @ 10	ESE @ 20	ESE @ 20
Derived Wind Speed (knots)	-	16	-	18	16
Peak Wave Period (sec)	-	7.28	6.79	7.10	7.10
Secondary Wave Period (sec)	-	4.91	-	3.45	4.05
Significant Wave Height (ft)	-	4.12	3.32	3.59	3.80
Dominant Forcing Direction	32°S of E	13°N of E	32°N of E	13°S of E	18°S of E
Maximum m.s. Helideck Acc. $(ft/sec^2)^2$	.22	.71	.49	.53	.50
Minimum m.s. Helideck Acc. $(ft/sec^2)^2$	.11	.20	.23	.24	.25
Eccentricity, e	.85	.96	.89	.89	.87
Principal Modal Direction	25°S of E	13°N of E	35°N of E	7°S of E	15°S of E
Principal Natural Frequency Est. (Hz)	.325	.323	.323	.323	.324
Principal Damping Ratio Est. (%)	1.1+/-.3	1.0+/-.4	.9+/-.2	1.9+/-.6	.9+/-.4
Orthogonal Modal Direction	20°N of E	32°S of E	10°S of E	38°N of E	30°N of E
Orthogonal Natural Frequency Est. (Hz)	.327	.328	.327	.327	.323
Orthogonal Damping Ratio Estimate (%)	1.3+/-.3	1.4+/-.4	1.1+/-.3	1.9+/-.7	1.5+/-.5

1) Least squares fit (Removes linear trend)

2) Integrate (uses digital integration technique developed by Schuessler and Ibler, 1974).

3) High pass filter (Removes low frequency components)

4) Least Squares fit

5) Integrate

6) High pass filter

7) Least squares fit

The results of the double integration are shown in Figures 8.26 and 8.27 for 200 seconds of the reel 3 EAW accelerometer time history. Similar results were obtained for the NAW accelerometer. The initial 50 seconds of the displacement record are not usable. This is because the double integration routine requires some initial time to reach steady-state behavior.

The EAW and NAW displacement time histories are then plotted as ordered pairs in the horizontal plane using the program VECTOR. Figures 8.28-8.30 are plots of the displacement trace of the Lollipop measured by the EAW and NAW accelerometers on reel 3. In Figure 8.28, the motion starts in a predominantly Northeast to Southwest pattern, shifts to a circular counter-clockwise motion and ends, in Figure 8.30, in an almost north-south movement. The motion is clearly random as is the corresponding dynamic stress field within the pile.

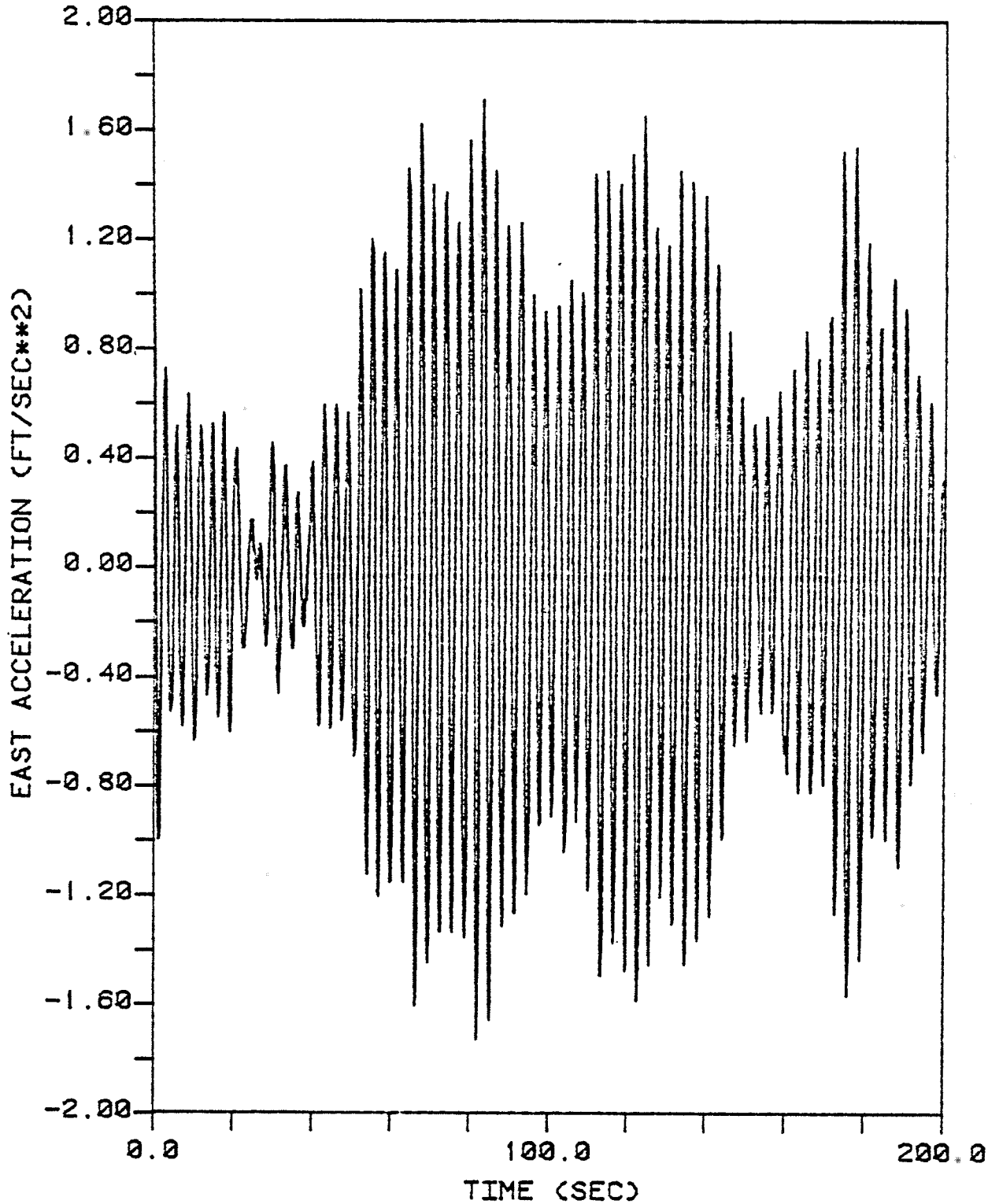

FIG 8.26: REEL 3 EAW ACCELEROMETER TIME HISTORY

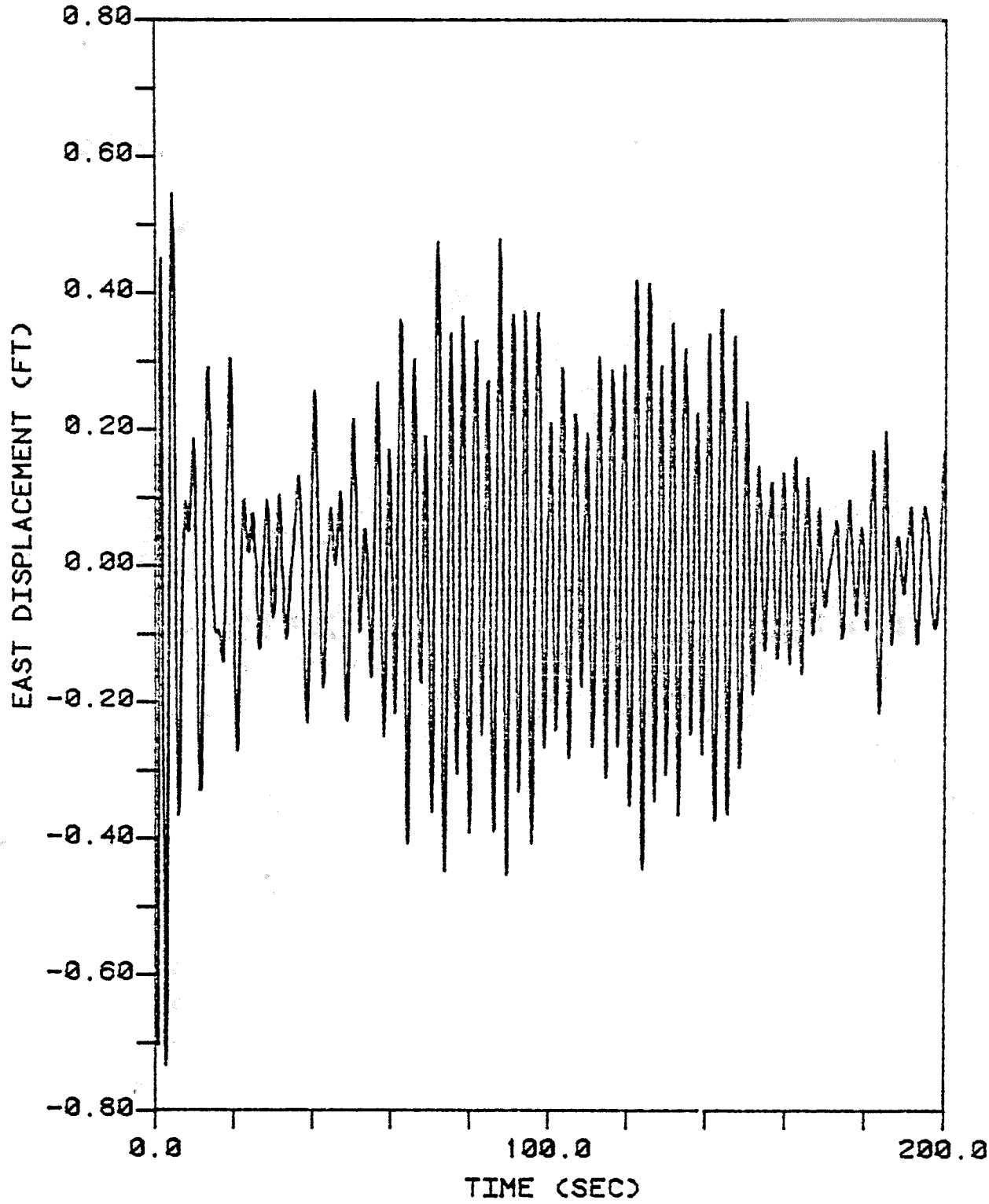

FIG 8.27: REEL 3 EAW DISPLACEMENTS AFTER DOUBLE INTEGRATION

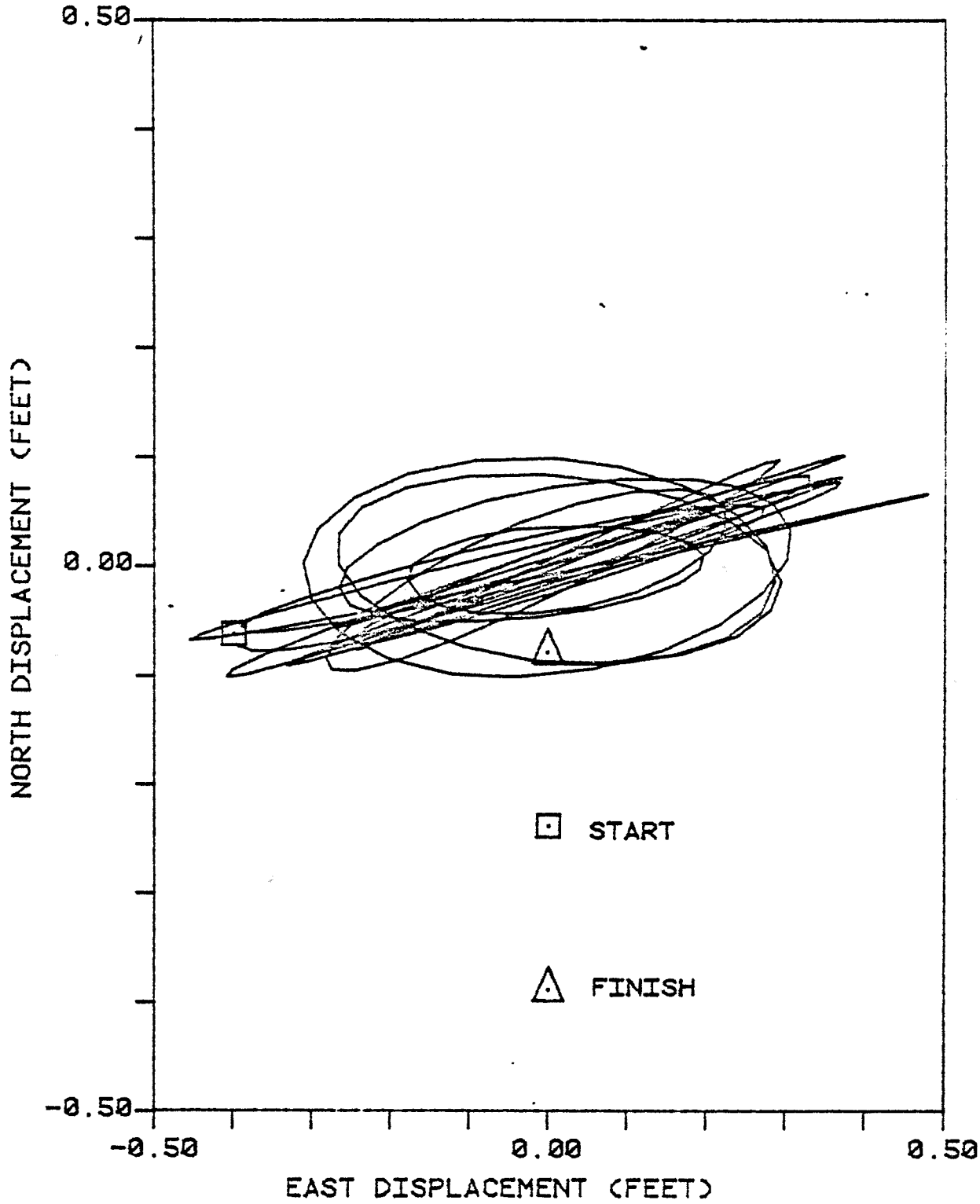

FIG 8.28: REEL 3 LOLLIPOP DISPLACEMENTS 80-120 SECONDS

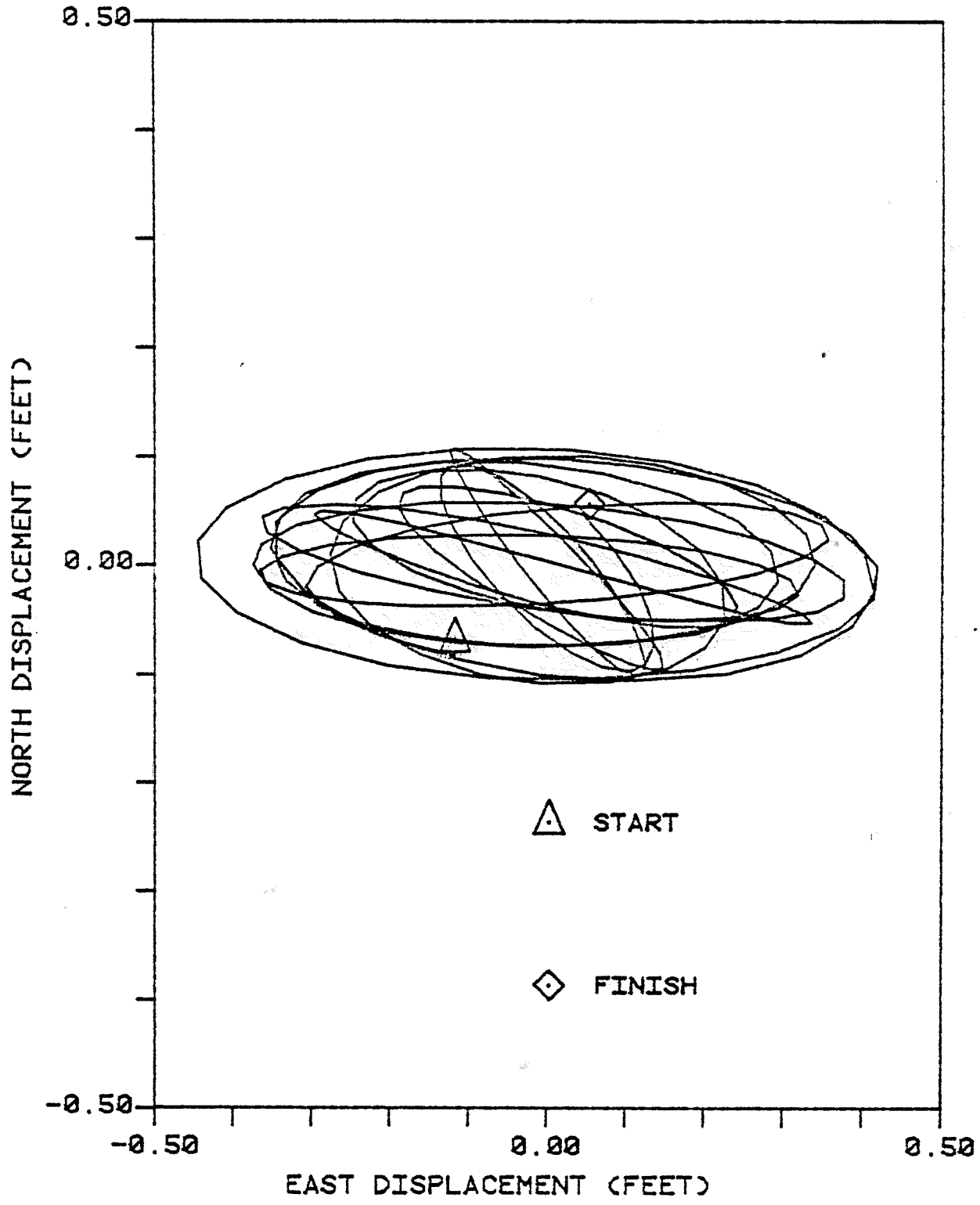

FIG 8.29: REEL 3 LOLLIPOP DISPLACEMENTS 120-160 SECONDS

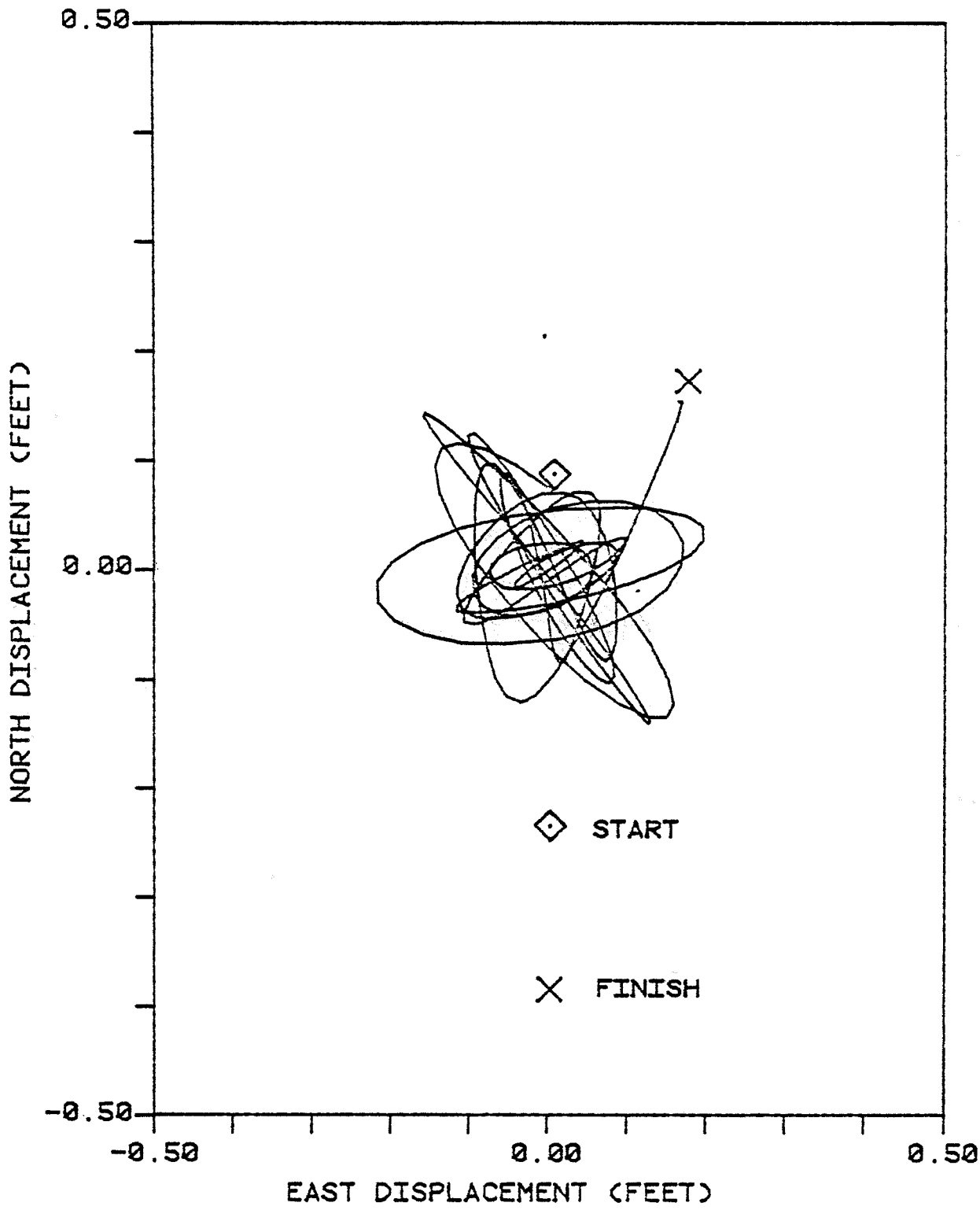

FIG 8.30: REEL 3 LOLLIPOP DISPLACEMENTS 160-200 SECONDS

8.4 Two-Channel Analysis - Mode Shape Identification

In addition to the identification of the spatial orientation of the fundamental bending modes of the AMOCO caisson, two-channel spectral analysis can be used to isolate higher vibration modes, identify mode shapes, and compute transfer functions between two locations on the structure or between an input and an output. Each of these topics is thoroughly addressed in the thesis by Briggs, 1981, in which he applied multichannel MEM spectral analysis techniques to the Lollipop data. Some of his results are included here in order to document all pertinent data analysis of the AMOCO caisson in a single source. In particular, his analysis of reel 2 (Load Case 2 in his thesis) is summarized here.

The primary reason for recording a set of four accelerometers in reel 2 was to identify the response mode shapes of the Lollipop. Mode shape identification is accomplished using the values of the transfer functions between accelerometers at each of the platform's responding natural modes. Cross-spectral magnitudes, phase and coherence estimates are required to isolate these modes. As an illustration, the cross-spectral results between north pointing accelerometers on the helideck (NAH) and the wellhead deck (NAW) are shown in Figures 8.31-8.34. The magnitude of the cross-spectral estimate is plotted on log scale to show detail at all sampled frequencies. The significant spectral peaks are associated with a mode from the phase and coherence estimates. For instance, for the fundamental flexure peak, the accelerometers are in

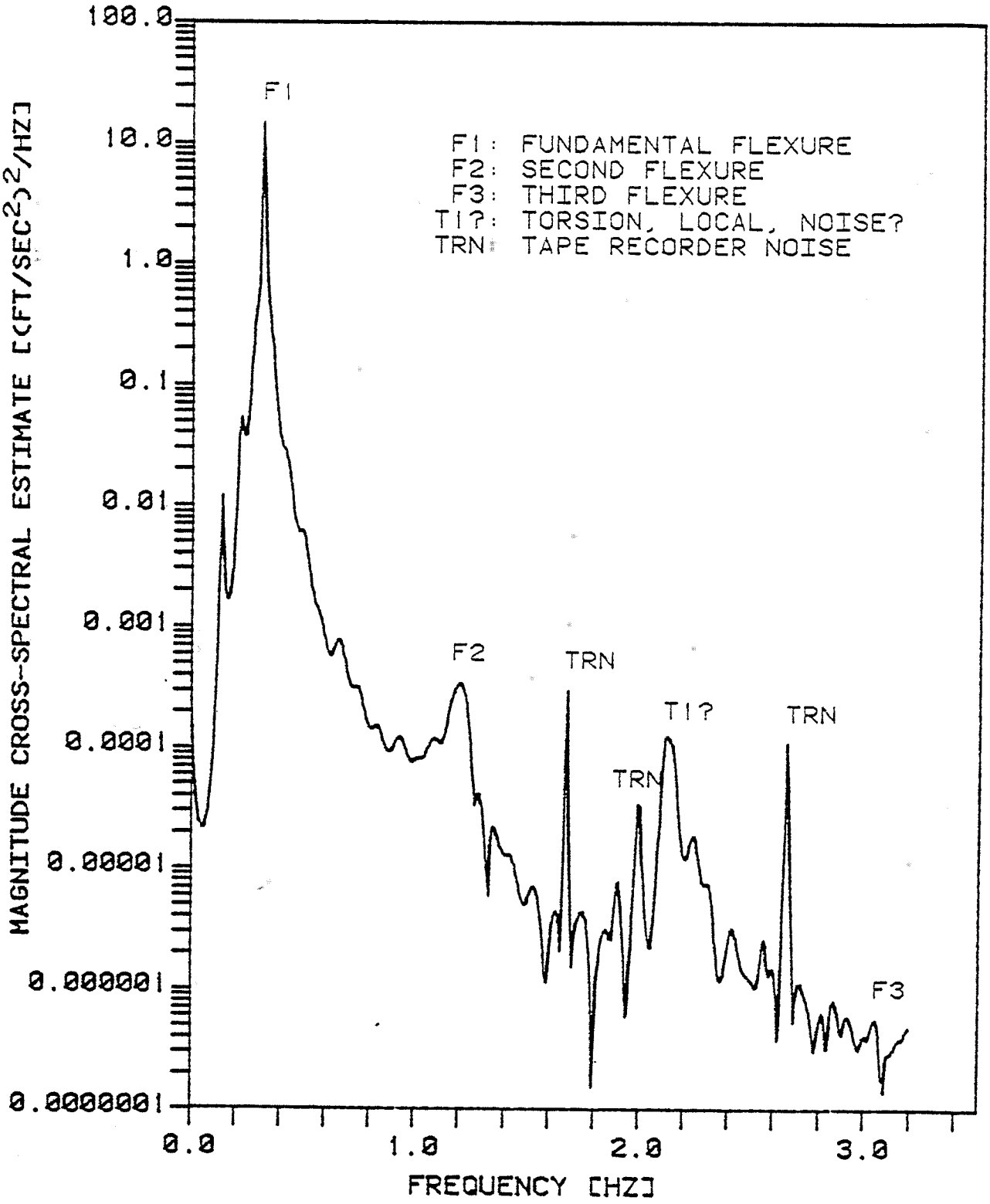

FIG 8.31: REEL 2 NAH & NAW MAGNITUDE CROSS-SPECTRUM, 80 LAGS

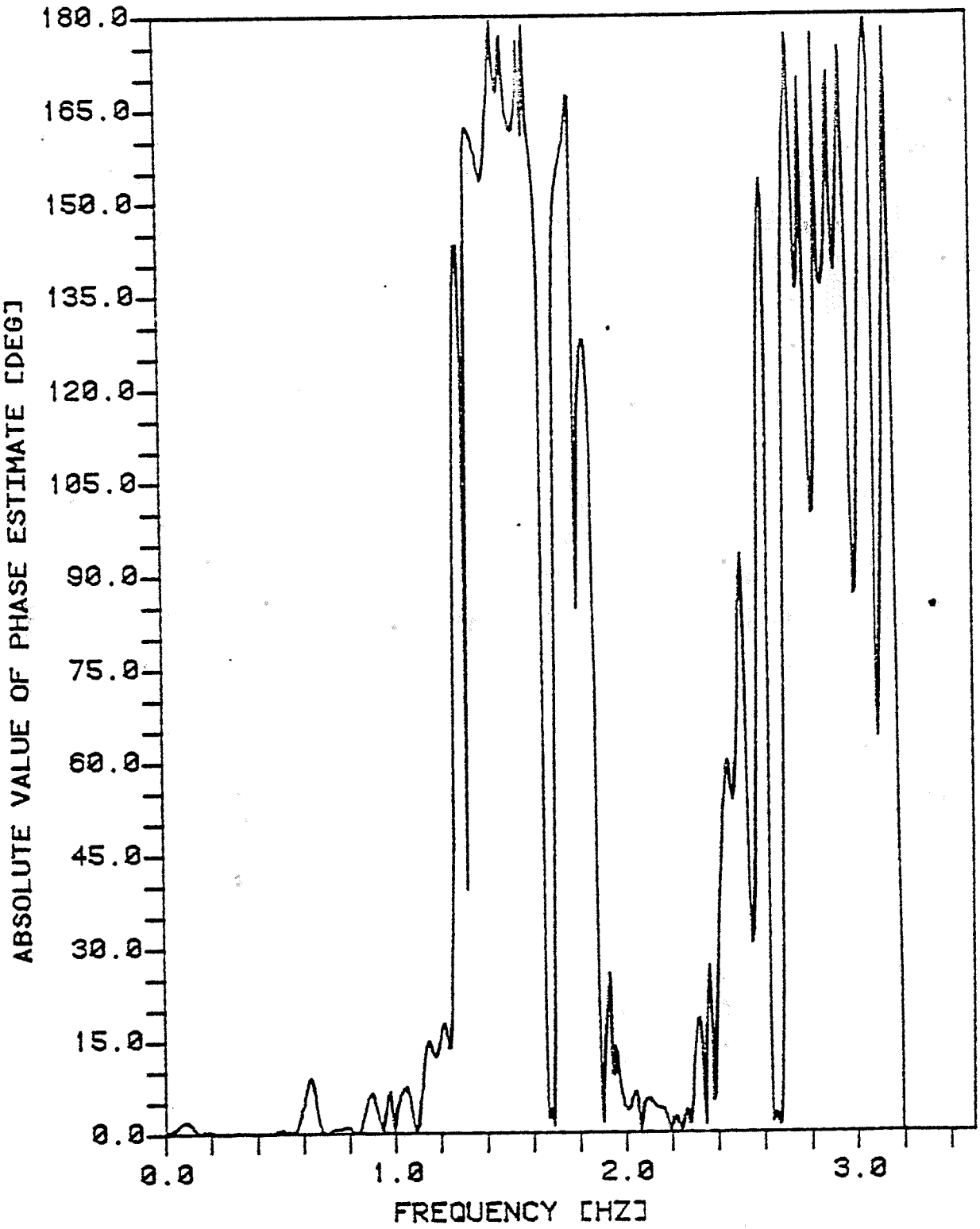

FIG 8.32: REEL 2 NAH & NAW PHASE ESTIMATES, 80 LAGS

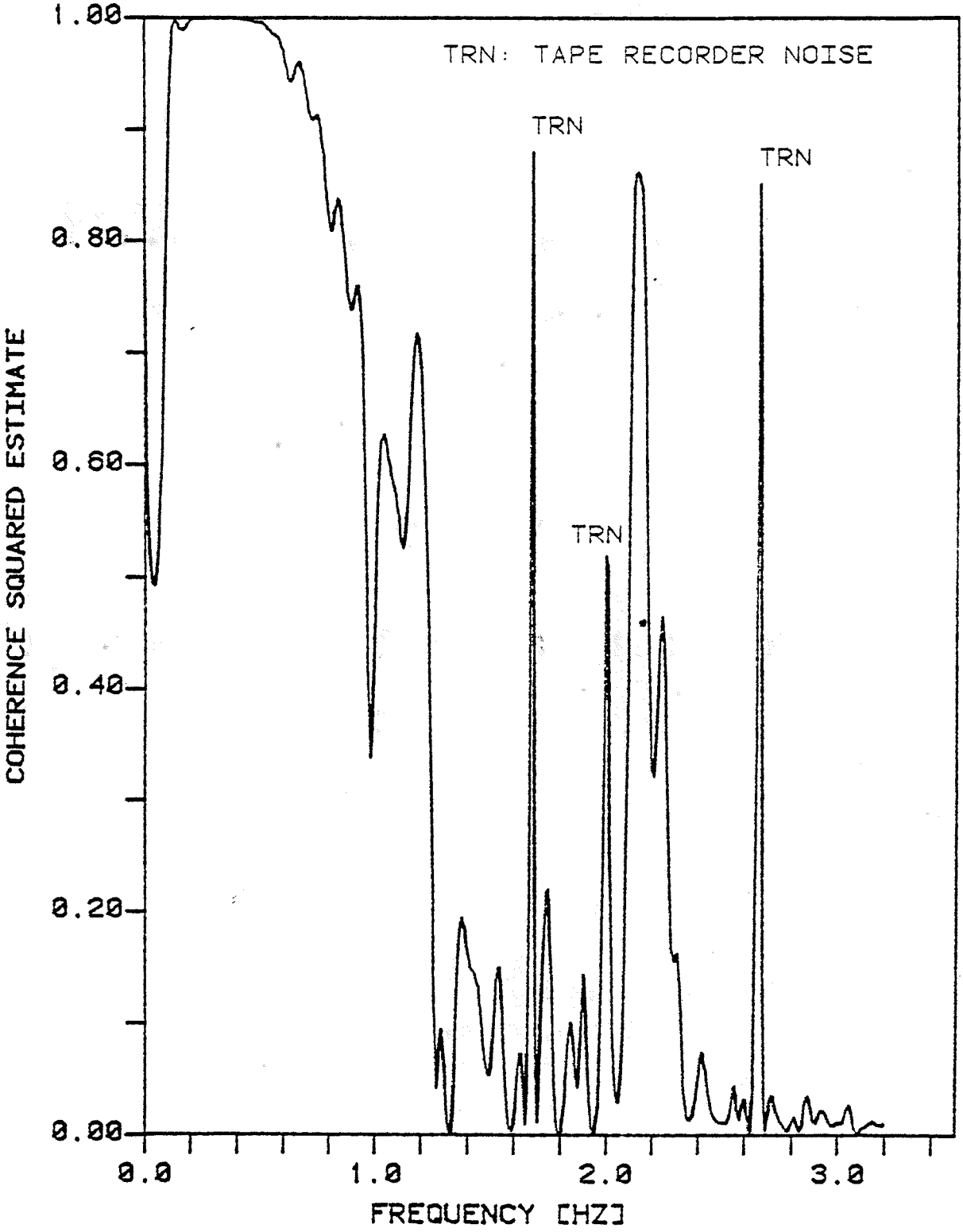

FIG 8.33: REEL 2 NAH & NAW COHERENCE ESTIMATES, 80 LAGS

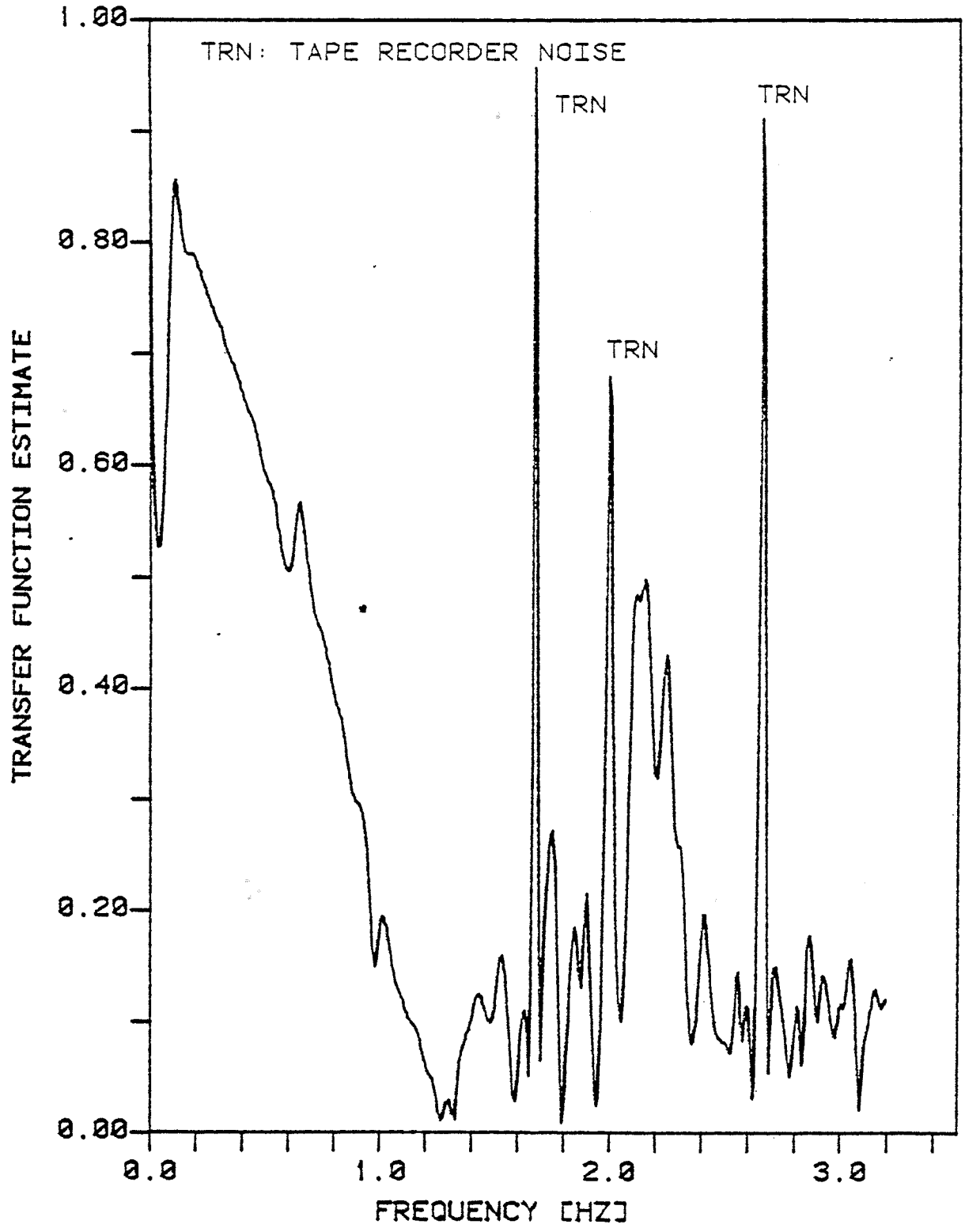

FIG 8.34: REEL 2 NAH & NAW TRANSFER FUNCTION ESTIMATE, 80 LAGS

phase with one another with unity coherence indicating first mode response. The tape recorder noise peaks will be discussed in the next paragraph. Once the modal response frequencies are known, the values of the transfer function between one pair of accelerometers at these frequencies are tabulated. After analysis of each pair of accelerometers, an estimate of the mode shape can be made. Results of this procedure are shown in Table 8.7. The estimated mode shape of the first two fundamental modes is plotted in Figure 8.35 against the mode shape from the finite element model discussed in Chapter 3.

The tape recorder noise (TRN) peaks identified in Figure 8.31 were isolated by recording a tape with grounded inputs and then computing the noise spectrum. Figure 8.36 shows the noise spectrum normalized to the same units and plotted on the same scale as the cross-spectral magnitude. The presence of noise in the measurements introduces significant errors into the spectral estimates unless the signal to noise ratio (SNR) is large. For the Lollipop, which responds predominantly in only its lowest bending modes, the second and third modal responses have relatively small SNR and the spectral estimates at these frequencies are less reliable.

TABLE 8.7
SUMMARY OF CROSS-SPECTRAL ESTIMATES
FIRST THREE FLEXURAL MODES [BRIGGS, 1981]

Accelerometers	Phase [Deg]	Coherence Sq.	Transfer Function
	Fundamental Flexure = 0.32 Hz		
NAH and NAP	0	1.00	0.85
NAH and NAW	0	1.00	0.70
NAH and NAB	0	1.00	0.40
	Second Flexure = 1.20 Hz		
NAH and NAP	0	1.00	0.57
NAH and NAW	12	0.70	0.07
NAH and NAB	180	0.95	0.65
	Third Flexure = 3.06 Hz		
NAH and NAP	15	0.00	0.15
NAH and NAW	180	0.05	0.15
NAH and NAB	180	0.00	0.10

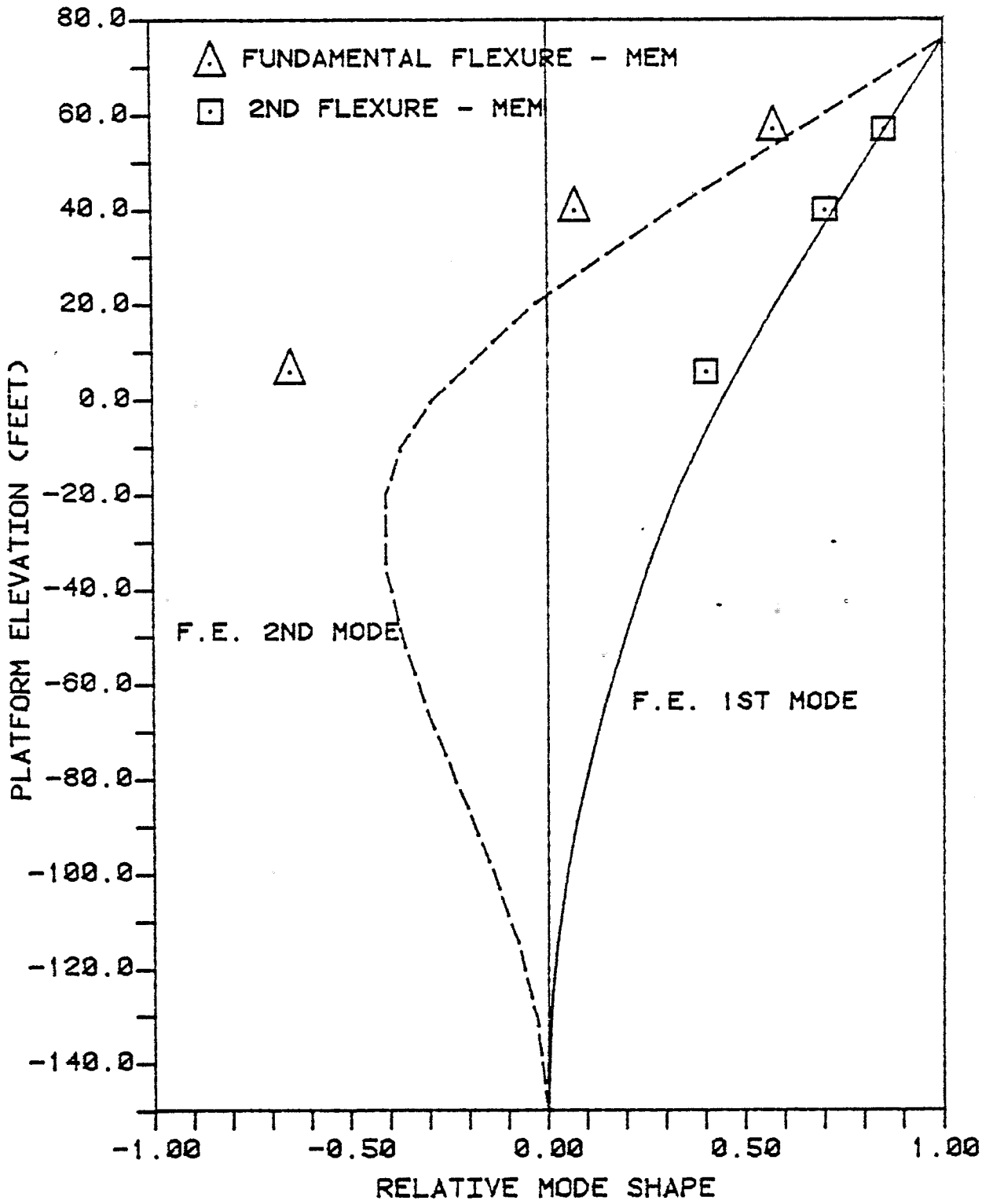

FIG 8.35: MODE SHAPE COMPARISON: MEM ANALYSIS VERSUS F.E. MODEL

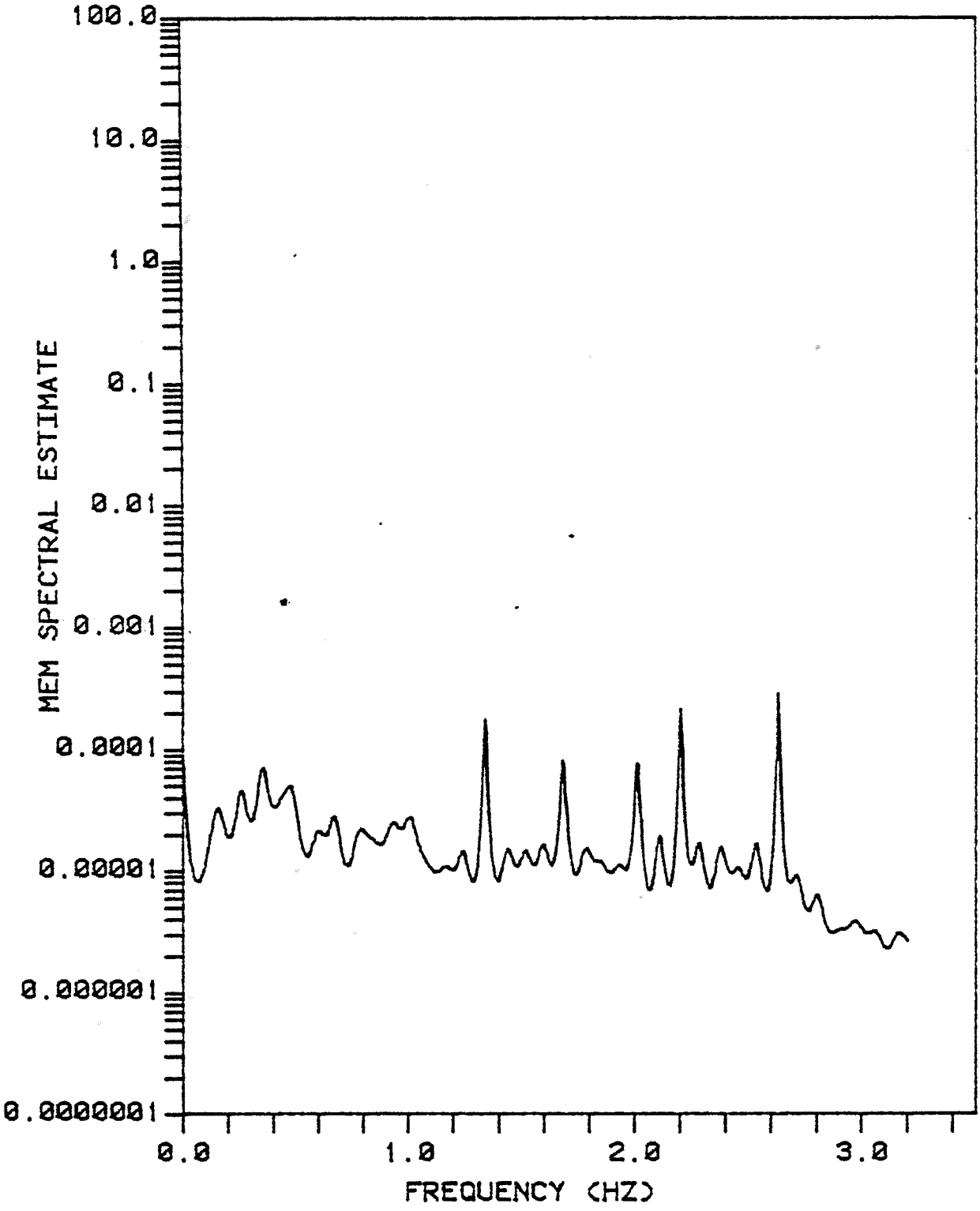

FIG 8.36: TAPE RECORDER NOISE MEM SPECTRUM, 80 LAGS

CHAPTER 9

SUMMARY AND CONCLUSIONS

The dynamic response characteristics of an operational single pile platform, the AMOCO caisson, have been investigated along two different paths. The first approach combined a dynamic finite element model, a theoretical assessment of damping and an effective technique of predicting platform response levels to yield estimates of the dynamic response fatigue life of the structure. The analysis of wind, wave and response time histories provided the other source of information about response characteristics.

Fatigue life estimation for a dynamically responding offshore platform is full of uncertainty. For the designer, uncertainty begins in the formulation of a structural model. Dynamic finite element models are particularly sensitive to changes in the foundation and extreme care must be taken if accurate structural natural frequencies are to be obtained. Accurate characterization of the damping phenomena is also a requirement. Separately estimating the contributions to the total damping, as outlined here, is a first step toward insuring the structural model accurately represents the physical system. More research is needed to establish the modal soils damping associated with a dynamically responding platform. Also, the relationship between damping and exciting forces should not be ignored. Radiation (wave making) and viscous hydrodynamic damping are proportional to the inertial and

drag forces, respectively.

Recognition of the relationship between radiation damping and linear wave forces, using the principle of reciprocity of ocean waves, leads to an expression to predict response levels of a structure subjected to random directionally spread seas. For the AMOCO caisson, predicted responses agreed closely with measured response levels.

Incorporating results from the finite element model with the reciprocity method, a versatile equation for the mean rate of accumulation of fatigue damage was produced. With this expression, the sensitivity of the fatigue accumulation model to small variations in input parameters is quickly established. The model explicitly includes wave spreading. More research is needed to quantify the statistics of the stress field within a structural member under resonant response conditions when several modes are excited.

The other major portion of the research leading to this thesis was the analysis of wind, wave and response time histories recorded on the AMOCO single pile platform in March, 1980. The major thrust of the analysis was an attempt to isolate the orientation of the fundamental flexural bending modes from the time histories of a biaxial pair of accelerometers. Using a correlation function rotation scheme based on a Mohr's circle algorithm, the response characteristics of the platform as a function of rotation angle were investigated. Both the modal orientation, defined as the angle where the coherence, evaluated at the natural frequency of the first mode, between

accelerometers was a minimum, and the dominant forcing direction, the angle associated with the maximum mean square response, were isolated for each biaxial pair.

Results indicate that the modal orientation and the dominant forcing were less than 10 degrees apart in all cases. Also, orthogonal fundamental mode responses were observed to be incoherent for three reels which indicates modal responses may be independent in certain cases. In addition, when the forcing changed direction, the modal orientation, as defined above, shifted direction as well. This would imply that directionality in the forcing alters the modal orientation and the most probable mechanism is through modifications of the soils properties under cyclic loading. The dominant response direction was also used to estimate spreading in the incident wave field and the results seem plausible. However, at the present stage of research, with data from only one structure, the conclusions drawn here are speculative. Further experiments are necessary.

A single pile platform is a relatively simple structure which exhibits most of the dynamic response characteristics associated with larger flexible structures. In this research, the factors which influence a fatigue analysis of one such structure have been identified. In addition, analysis of field data has identified several characteristics of response which need verification. The installation of a carefully designed fully instrumented single pile structure would supply the offshore community with the data necessary to clearly id-

entify the behavior of a dynamically responding platform in a random sea.

REFERENCES

Akaike, H., "Power Spectrum Estimation Through Autoregressive Model Fitting", Ann. Institute of Statistical Mathematics, Vol. 23, pp. 407-419, 1970.

Angelides, D.C., Roesset, J.M., "Nonlinear Dynamic Stiffness of Piles", Research Report R80-13, Dept. of Civil Engr., MIT, April, 1980.

Bathe, K.J., Wilson, E.L., Numerical Methods in Finite Element Analysis, Prentice-Hall, Inc., Englewood Cliffs, New Jersey, 1976.

Bathe, K.J., "ADINA: A Finite Element Program for Automatic Dynamic Incremental Nonlinear Analysis", Report 82448-1, Acoustics and Vibration Laboratory, Mechanical Engineering Dept., MIT, 1978.

Berge, B., Penzien, J., "Three-Dimensional Stochastic Response of Offshore Towers to Wave Forces", OTC 2050, Houston, May, 1974.

Bendat, J.S., Piersol, A.G., Random Data: Analysis and Measurement Procedure, Wiley-Interscience, New York, 1971.

Bendat, J.S., Piersol, A.G., Engineering Applications of Correlation and Spectral Analysis, Wiley-Interscience, New York, 1980.

Biggs, J.M., Introduction to Structural Dynamics, McGraw-Hill, New York, 1964.

Blaney, G.W., Kausel, E., Roesset, J.M., "Dynamic Stiffness of Piles", Second International Conference on Numerical Methods in Geomechanics, Blacksburg, VA, 1976, pp. 1001-1012.

Briggs, M.J., "Multichannel Maximum Entropy Method of Spectral Analysis Applied to Offshore Structures", Dissertation, Massachusetts Institute of Technology and Woods Hole Oceanographic Institution, WHOI-81-69, August, 1981.

Burg, J.P., "Maximum Entropy Spectral Analysis", 37th Society of Exploration Geologists Winter Meeting, Oklahoma City, Oklahoma, 1967.

Campbell, R.B., "The Estimation of Natural Frequencies and Damping Ratios of Offshore Structures", Doctoral Dissertation, Massachusetts Institute of Technology, January, 1980.

Connor, J.J., Sunder, S.S., "Wave Theories, Wave Statistics and Hydrodynamic Loads", Dept. of Civil Engr., MIT, 1980.

Cook, M.F., Davidson, M., Lin, W.M., "Dynamic Analysis of Offshore Single-Pile Platform by Finite Element Method", MIT, 2.093 Term Project, May, 1981.

Crandall, S.H., Mark, W.D., Random Vibration in Mechanical Systems, Academic Press, New York, 1963.

Crandall, S.H., "The Role of Damping in Vibration Theory", Journal of Sound and Vibration, Vol. 11(1), 1970, pp. 3-18.

Draper Labs (Campbell, R.B., et. al.,), "Passive and Active Suppression of Vibration Response in Precision Structures, State-of-the-Art Assessment", Technical Report R-1138, Vol. 2, Technical Analysis, Charles Stark Draper Laboratory, Inc., February, 1978.

Dunwoody, A.B., "The Role of Separated Flow in the Prediction of the Dynamic Response of Offshore Structures to Random Waves", Ph.D. Thesis, MIT, May, 1980.

Dunwoody, A.B., Vandiver, J.K., "The Influence of Separated Flow Drag on the Dynamic Response of Offshore Structures to Random Waves", Proceedings, Hydrodynamics in Ocean Engineering, Trondheim, August, 1981.

Haskind, M.D., "The Exciting Forces and Wetting of Ships in Waves", (in Russian) Izrestia Akademii Nauk S.S.S.R., Otdelenie Tekhnicheskikh Nauk (1957) No. 7, pp. 65-79. (English Translation available as David Taylor Model Basin Translation No. 307, March, 1962.)

Hong, S.T., Brooks, J.C., "Dynamic Behavior and Design of Offshore Caissons", OTC 2555, May, 1976.

Kinra, R.K., Marshall, P.W., "Fatigue Analysis of the Cognac Platform", OTC 3378, Houston, May, 1979.

Lazan, B.J., Goodman, L.E., "Material and Interface Damping", Vol. 2, Chapter 36, Shock and Vibration Handbook, ed. by Harris, C.M., Crede, C.E., McGraw-Hill, New York, 1961.

Lu, X., Vandiver, J.K., "Least P^{th} Optimization of Parameter Estimation in Structural Response Spectrum", OTC 4283, May, 1982.

Marshall, P.W., "Dynamic and Fatigue Analysis Using Directional Spectra", OTC 2537, Houston, May, 1976.

Meirovitch, L., Elements of Vibration Analysis, McGraw-Hill, New York, 1975.

Newman, J.N., "The Exciting Forces on Fixed Bodies in Waves", Journal of Ship Research, SNAME, Vol. 6, No.3, December, 1962.

Novak, M., Nogami, T., "Soil-Pile Interaction in Horizontal Vibration", Earthquake Engineering and Structural Dynamics, Vol. 5, 1977, pp. 263-281.

Oppenheim, A.V., Schaffer, R.W., Digital Time Series Analysis, John Wiley & Sons, New York, 1975.

Petrauskas, C., "Hydrodynamic Damping and 'Added Mass' for Flexible Offshore Platforms", U.S. Army Coastal Engineering Research Center, Report CERC-TP-76-18, October, 1976.

Poulos, H.G., Davis, E.H., Pile Foundation Analysis and Design, John Wiley & Sons, New York, 1980.

Sarpkaya, T., "Vortex Shedding and Resistance in Harmonic Flow About Smooth and Rough Cylinders", Proceedings, International Conference on the Behavior of Offshore Structures, Trondheim, 1976.

Schuessler, H.W., Ibler, W., "Digital Filters for Integration", European Conference on Circuit Theory and Design, Institute of Electrical Engineers, Conference Publication No. 116, 1974.

Stevens, J.B., Audibert, J.M.E., "Re-examination of P-Y Curve Formulations", OTC 3402, Houston, May, 1979.

Vandiver, J.K., "Prediction of the Damping Controlled Response of Offshore Structures to Random Excitation", OTC 3515, Houston, May, 1979.

Vandiver, J.K., "The Significance of Dynamic Response in the Estimation of Fatigue Life", Submitted to the Norges Tekniske Hogskole at Trondheim, following completion of a visiting professorship during the summer of 1980, October 1980.

Vughts, J.H., Kinra, R.K., "Probabilistic Fatigue Analysis of Fixed Offshore Structures", OTC 2608, Houston, May, 1976.